NOVEL INSIGHTS INTO MASS AND ENERGY TRANSFER AT MID-OCEAN RIDGES FROM SEISMIC IMAGING OF THE EAST PACIFIC RISE AND JUAN DE FUCA RIDGE

by

GILLEAN MEKAISTO ARNOUX

A DISSERTATION

Presented to the Department of Earth Sciences
and the Graduate School of the University of Oregon
in partial fulfillment of the requirements
for the degree of
Doctor of Philosophy

December 2018

DISSERTATION APPROVAL PAGE

Student: Gillean Mekaisto Arnoux

Title: Novel Insights into Mass and Energy Transfer and Mid-Ocean Ridges from Seismic Imaging of the East Pacific Rise and Juan de Fuca Ridge

This dissertation has been accepted and approved in partial fulfillment of the requirements for the Doctor of Philosophy degree in the Department of Earth Sciences by:

Prof. Douglas R. Toomey	Chairperson/Advisor
Prof. Emilie E. E. Hooft	Core Member
Prof. Paul J. Wallace	Core Member
Prof. Eugene D. Humphreys	Core Member
Prof. John S. Conery	Institutional Representative

and

Janet Woodruff-Borden	Vice Provost and Dean of the Graduate School

Original approval signatures are on file with the University of Oregon Graduate School.

Degree awarded December 2018

DISSERTATION ABSTRACT

Gillean Mekaisto Arnoux

Doctor of Philosophy

Department of Earth Sciences

December 2018

Title: Novel Insights into Mass and Energy Transfer and Mid-Ocean Ridges from Seismic Imaging of the East Pacific Rise and Juan de Fuca Ridge

In this dissertation, I use seismic imaging and waveform modeling methods to investigate melt migration processes and the structure of the magma plumbing system beneath the East Pacific Rise (EPR) and Endeavour segment of the Juan de Fuca Ridge, respectively. This work begins by studying shallow mantle reflections beneath the EPR. I find the amplitude versus offset and waveform characteristics of the reflections to be consistent with a sub-horizontal dunite channels located up to 20 km off-axis. The depth of the dunite channels correlate with patterns of mantle melt delivery and the predicted base of the thermal lithosphere, suggesting the channels are thermally controlled and may have formed *in situ* via dissolution by focused flow at the base of the lithosphere. This interpretation is consistent with field observations in ophiolites and numerical modeling of melt-focusing channels. The three-dimensional velocity structure of the Endeavour segment is then investigated to identify how patterns of mantle melt delivery influence the segment-scale distribution of crustal melt and crustal accretion. The results from this study indicate that the mantle magmatic system is skewed relative to the ridge-tracking crustal magmatic system and that this skew exerts primary control on magmatic, tectonic, and hydrothermal activity at the Endeavour segment. In regions where mantle melt delivery is axis-centered, mantle-derived melts are efficiently transported from the mantle to the crust,

resulting in frequent crustal melt replenishment, associated seismogenic cracking, and enhanced crustal melt content that drives vigorous hydrothermal activity. Conversely, sites of off-axis melt delivery are characterized by less efficient vertical melt transport, resulting in infrequent crustal melt injection and hence, reduced crustal melt content and hydrothermal activity. Next, I focus on how along-axis variations in magma replenishment modulate crustal permeability and the intensity of hydrothermal circulation. Using full-waveform inversion, I show that sites of localized magma replenishment to the axial magma lens, along with induced seismogenic cracking, coincide with enhanced permeability. I conclude that the frequency of magma injection governs hydrothermal circulation patterns and heat flux at mid-ocean ridges.

This dissertation includes previously published and unpublished coauthored material.

CURRICULUM VITAE

NAME OF AUTHOR: Gillean Mekaisto Arnoux

GRADUATE AND UNDERGRADUATE SCHOOLS ATTENDED:

University of Oregon, Eugene, Oregon, USA
Montana State University, Bozeman, Montana, USA
University of Montana, Missoula, Montana, USA

DEGREES AWARDED:

Doctor of Philosophy, Geological Sciences, 2018, University of Oregon
Bachelor of Science, Earth Sciences, 2011, Montana State University

AREAS OF SPECIAL INTEREST:

Seismic Imaging
Mid-Ocean Ridge Magmatic and Tectonic Processes
Tectonic-Magmatic-Hydrothermal Interactions

PROFESSIONAL EXPERIENCE:

Graduate Teaching Fellow, University of Oregon, 2012-2018

Undergraduate Research Assistant, Montana State University, 2010-2011

Lab Assistant, Montana State University, 2010

GRANTS, AWARDS, AND HONORS:

Weiser Scholarship, University of Oregon, 2018

Outstanding Student Paper Award, American Geophysical Union, 2017

Graduate Research Grant, Geological Society of America, 2016

Earth Sciences Research Recognition Award, University of Oregon, 2016 and 2018

Johnston Scholarship, University of Oregon, 2013, 2014, 2015, 2016, and 2017

PUBLICATIONS:

Hooft, E. E., Nomikou, P., Toomey, D. R., Lampridou, D., Getz, C., Christopoulou, M. E., O'Hara, D., **Arnoux, G. M.**, Bodmer, M., Gray, M., Heath, B. A., and VanderBeek, B. P. (2017). Backarc tectonism, volcanism, and mass wasting shape seafloor morphology in the Santorini-Christiana-Amorgos region of the Hellenic Volcanic Arc. *Tectonophysics*, 712, 396-414.

Arnoux, G. M., Toomey, D. R., Hooft, E. E., Wilcock, W. S., Morgan, J., Warner, M., and VanderBeek, B. P. (2017). Seismic evidence that black smoker heat flux is influenced by localized magma replenishment and associated increases in crustal permeability. *Geophysical Research Letters*, 44, 1687-1695.

Morgan, J., Warner, M., **Arnoux, G.**, Hooft, E., Toomey, D., VanderBeek, B., and Wilcock, W. (2016). Next-generation seismic experiments—II: wide-angle, multi-azimuth, 3-D, full-waveform inversion of sparse field data. *Geophysical Journal International*, 204(2), 1342-1363.

ACKNOWLEDGMENTS

The process of earning a doctorate and writing a dissertation is long and arduous—and one that requires support and guidance from various people. First and foremost, I would like to thank my wife, Becky, for her endless love and support throughout this process. She helped me immensely during graduate school and without her constant support, encouragement, and understanding, I would not have been able to achieve this educational endeavor. I would be remiss to not mention and thank my advisors, Douglas Toomey and Emilie Hooft, whose expertise, patience, and guidance made my research and this dissertation succeed. They have helped me dramatically evolve as a scientist and person and also provided me with fantastic travel opportunities for both research and recess. I also thank the other members of my dissertation committee, Eugene Humphreys, Paul Wallace, and John Conery, for their helpful feedback throughout the years. I am also grateful for the generosity and guidance of Joanna Morgan and Mike Warner (Imperial College London), who hosted me at their institution (on two separate occasions) and helped me get acquainted with a piece of software integral to my dissertation. I thank my fellow geophysics students, Miles Bodmer, Ben Heath, Brandon VanderBeek, and Joe Byrnes, for their friendships and providing ample entertainment. I must also acknowledge the UO Department of Earth Sciences office staff, who were always there to answer silly and often redundant questions. Lastly, I thank my favorite office mate, Captain Malcolm Reynolds, who helped relieve or impart stress, depending on the day…

This work was partially supported by the National Science Foundation under grants OCE-0454747, OCE-0651123, and OCE-1634786 to the University of Oregon.

For Becky, the love of my life, who made this all possible.

TABLE OF CONTENTS

Chapter Page

LIST OF FIGURES

LIST OF TABLES

Table Page

CHAPTER III

CHAPTER I

INTRODUCTION

Mid-ocean ridges represent one of the most significant geological processes shaping Earth. These systems accounts for a vast majority (~75%) of Earth's annual magma budget, generating over two-thirds of the global crust, and are the primary means of geochemical differentiation within the earth. Magmatic systems beneath oceanic spreading centers drive hydrothermal systems that modulate the long-term chemistry of the ocean, hydrate the crust and mantle, and support enormous ecosystems. However, owing to sparse subsurface observations of these systems, we lack a precise understanding of how melt transport and distribution at mid-ocean ridges influences the structure of oceanic crust and variations in ridge-crest processes. This work seeks to advance our fundamental understanding of mass and energy transfer at mid-ocean ridges and its relation to the generation and evolution of oceanic crust by investigating the following questions: How is melt focused from the broad zone of melt generation within the mantle to the narrow zone of crustal accretion at the ridge axis? What controls the characteristics and distribution of crustal magma bodies? What mechanism controls the intensity of high-temperature hydrothermal systems at mid-ocean ridges? To address these questions, this dissertation analyzes marine active-source seismic data using a variety of geophysical techniques, principle being travel-time tomography and full-waveform inversion, to image the three-dimensional structure of the upper mantle and crust beneath the East Pacific Rise (EPR) and Endeavour segment of the Juan de Fuca Ridge (JdFR). These images are used to place constraints on the physical properties of the oceanic mantle and crust beneath active spreading centers.

Crustal accretion along mid-ocean ridges primarily occurs within a few kilometers of the ridge axis. This, combined with seismic evidence that melt generation occurs over a much broader region of mantle (>100 km), requires that melt be focused laterally to the ridge axis. The mechanics of magmatic focusing, however, are actively debated. In Chapter II, I use travel-time tomography, amplitude versus offset (AVO), and waveform modeling to investigate the origin of off-axis, subcrustal reflections detected in active-source seismic data collected at the EPR and whether or not they relate to the process of magmatic focusing. Tomographic imaging reveals that interfaces lie at depths between 2 and 6 km beneath the crust-mantle boundary, with the deepest interface located near the Clipperton Transform Fault that bounds the northern end of the ridge segment. This ridge-parallel variability in interface geometry correlates, to first-order, with the pattern of mantle upwelling, suggesting that the interfaces are thermally controlled. AVO analysis and waveform modeling show that the reflections originate from a contact between residual mantle, harzburgite, and dunite, a lithologic contact commonly observed in the mantle section of ophiolites. Such dunitic features are inferred to be replacive features that serve as conduits for focused porous flow. On the basis of these results, I suggest that the imaged interfaces are sub-horizontal dunite layers associated with intermittent or former melt flow; the lack of appreciable *S*-waves in the seismic data, combined with results from AVO and waveform modeling, indicates the absence of melt. These results are consistent with both field observations of ophiolites and geodynamic modeling, which suggest focused flow within high-porosity channels at the base of the thermal lithosphere as a mechanism for magmatic focusing beneath mid-ocean ridges.

While Chapter II addresses an outstanding question pertaining to magmatic focusing from the mantle to the ridge, Chapter III investigates how patterns in mantle melt

delivery relate to along-axis variations in magmatic, tectonic, and hydrothermal processes and the structure of the crustal magma reservoir and oceanic crust as a whole. Active-source seismic data is used to constrain the three-dimensional *P*-wave velocity of the topmost mantle and crust beneath the Endeavour segment of the northern JdFR; these velocity images are then used to constrain the segment-scale thermal structure and melt distribution beneath the ridge. Tomographic images reveal a segment-scale skew between the pattern of mantle melt delivery and the ridge-tracking crustal magmatic system. The thermal structure beneath the Endeavour segment suggests that the steep-sided crustal thermal anomaly is shaped by pervasive crustal-scale hydrothermal circulation, whereas the width and trend of the mantle magmatic system is determined by the regional-scale, mantle thermal structure of the northern JdFR. I synthesize these results with geophysical and petrological observations from the Endeavour segment to develop a conceptual model for how this skew governs the segment-scale composition, thermal structure, and melt content of the crust and along-axis variations in ridge-crest processes. In sites of axis-centered mantle melt delivery, the crustal magmatic system is prominent and feeds vigorous hydrothermal activity, whereas sites of off-axis mantle melt delivery are characterized by diminished crustal melt content and hydrothermal activity, and higher degrees of differentiation. These results demonstrate that skew between the mantle and crustal magmatic systems governs mid-ocean ridge magmatic and ridge-crest processes.

Chapter IV is an extension of the work in Chapter III and further explores the connection between magmatic, hydrothermal, and tectonic processes beneath the Endeavour segment using 3-D full-waveform inversion. I construct high resolution (<1 km resolution) *P*-wave images of the upper 3 km of crust beneath the Endeavour hydrothermal system. The velocity and inferred crustal permeability structure within this region of crust

is highly heterogeneous and correlates with along-axis variations in seismicity, hydrothermal heat flux, and depth of the axial magma lens (AML). Beneath the most robust vent fields on the segment, pronounced low-velocities directly overlie the shallowest portion of the AML and are associated with enhanced seismicity related to recent magma injection; the most prominent low-velocity zone beneath the AML is also located in this region. In contrast, the northern vent fields, characterized by the lowest heat fluxes, are underlain by a deeper AML that is capped by a high-velocity zone associated with little seismicity. These results indicate that localized magma recharge, along with induced seismogenic cracking and enhanced permeability, exerts a primary control on the heat flux of high-temperature hydrothermal systems. This work exemplifies the significant link between magmatic, tectonic, and hydrothermal processes at mid-ocean ridges and how they modulate mass and energy exchange between the solid Earth and its hydrosphere.

Chapter II is in preparation for publication and was coauthored with Douglas R. Toomey (University of Oregon). Chapter III was coauthored with Douglas R. Toomey (University of Oregon), Emilie E. E. Hooft (University of Oregon), and William S. D. Wilcock (University of Washington) and was submitted to *Geochemistry, Geophysics, Geosystems* in September 2018. Chapter IV was coauthored with Douglas R. Toomey (University of Oregon), Emilie E. E. Hooft (University of Oregon), William S. D. Wilcock (University of Washington), Joanna Morgan (Imperial College London), Mike Warner (Imperial College London), and Brandon P. VanderBeek (University of Oregon), and published in *Geophysical Research Letters* in February 2017.

CHAPTER II

SEISMIC EVIDENCE THAT SHALLOW MANTLE REFLECTORS BENEATH THE EAST PACIFIC RISE AT 9°30' TO 10°N ARE RELATED TO MELT MIGRATION PROCESSES

This chapter is in preparation for publication with Douglas R. Toomey. I performed the data analysis, wrote the text, and designed the figures. Douglas R. Toomey provided valuable input on the interpretation of my results and edited the initial draft of this chapter.

1.0 Introduction

Seismic reflection and refraction studies have shown that crustal accretion along mid-ocean ridges primarily occurs within several kilometers of the neovolcanic zone (Detrick et al., 1987; Vera et al., 1990). This, combined with seismic evidence that melt generation occurs over a much broader region of mantle—up to hundreds of kilometers in width (e.g., The MELT Seismic Team, 1998)—requires that melt be focused laterally to the ridge axis. The mechanics of magmatic focusing, however, remain incompletely understood and are actively debated (e.g., Kelemen et al., 1997). Much of what we know regarding magmatic focusing is derived from field investigations of ophiolites (Ceuleneer et al., 1996; Kelemen & Aharonov, 1998; Korenaga & Kelemen, 1997; Rabinowicz & Ceuleneer, 2005) and geodynamic modeling (Hebert & Montési, 2010; Sparks & Parmentier, 1991; Spiegelman, 1993a, 1993b). More direct constraints, such as geophysical observations, are few owing to the inaccessibility and associated difficulty of investigating oceanic spreading centers.

Recent geophysical studies shed light on the deep structure of active and paleo oceanic spreading centers. Several observations of melt accumulations at the Moho 22 km off-axis were observed at the East Pacific Rise (EPR) between 12°N and 12°50'N

(Garmany, 1989). Also at the EPR, mid-crustal melt bodies have been observed at distances of a few to 10s of kilometers off-axis (Canales et al., 2012; Durant & Toomey, 2009). At the Juan de Fuca Ridge, off-axis melt sills were imaged near the Moho up to 3.2 km off-axis (Canales et al., 2009) and frozen melt lenses were also detected in a 2-km-thick Moho Transition Zone 20-km off-axis (Nedimović et al., 2005). Such near-Moho and off-axis crustal features may be related to vertical percolation of melt from focused melt channels along the base of the lithosphere (Canales et al., 2009; Hebert & Montési, 2010). Compelling geophysical evidence for melt focusing in the mantle stems from the Western Somali Basin—an extinct spreading center. There, a seismic reflection profile imaged deep mantle reflections 10-20 km beneath the Moho (Sauter et al., 2016). The deepest of these reflections were attributed to frozen melt bodies and remnants of a paleo-melt channel system at the paleo-base of the lithosphere (Sauter et al., 2016). Similar features have yet to be observed near active spreading centers.

Here we present seismic evidence of reflections originating within the topmost mantle beneath an active oceanic spreading center—the fast-spreading EPR between 9°30'N and 10°10'N. We use travel-time tomography, amplitude versus incidence angle, and finite-difference waveform modeling to constrain the location, geometry, and physical properties of the reflection source. We also discuss the potential genesis of the reflection source in the context of the mechanics of mantle-to-crust magmatic focusing beneath mid-ocean ridges.

2.0 Seismic Data

The Undershoot seismic experiment was comprised of six wide-angle, seismic refraction experiments on the EPR. The experiment used 28 four-component, ocean bottom seismometers (OBSs) and 29 ocean bottom hydrophones (OBHs) deployed between the

Siqueiros and Clipperton transform faults to record rise-parallel and rise-perpendicular shooting lines. Previous analyses of the data include: (1) *P*-wave crustal refractions (*Pg*) and reflections from the Moho (*PmP*) to constrain region-scale variations in crustal structure (Canales et al., 2003) ; (2) *P*-wave refractions within the uppermost mantle (*Pn*) to constrain the structure of the topmost mantle beneath the ridge axis (Toomey et al., 2007); and (3) anomalous refracted and reflected arrivals attributed to an off-axis crustal magma body (Durant & Toomey, 2009).

We have identified anomalous high-amplitude, secondary arrivals attributed to reflections from a mantle interface in the northeastern portion of the study area (Figure 1). A total of six stations along the outer and inner eastern shot lines have recorded the anomalous reflections (Figure 1a). The largest and most prominent group of these arrivals are present on OBS 64, located ~20 km east of the ridge axis and ~45 km south of the Clipperton transform fault (Figure 2 and Appendix A, S1). Less prominent reflections are present on nearby stations: OBHs 20, 25, 24 and 16, as well as OBS 54 (Appendix A, Figures S2 and S3). Like *PmP*, the anomalous arrivals have energy between 5-20 Hz (Canales et al., 2003), though they are most easily visible between 20 and 60 Hz and are characterized by relatively high *P*-wave amplitudes on the vertical component and low *S*-wave amplitudes on the radial component (Figures 2 and Appendix A, S1). The travel-time versus range trend of the anomalous *P* phase is hyperbolic and diverges from *Pg* with decreasing source-receiver offset, which is indicative of a reflected phase. Travel-times of the anomalous *P*-wave reflections, hereafter referred to as *PaP*, range from ~5–8 seconds and arrive ~0.2–1.2 seconds after the *PmP* arrivals, indicating they originate within the topmost mantle. The greatest difference in arrival time between *PmP* and *PaP* occurs with smaller offset from the receivers and is larger to the north of the instruments, thereby

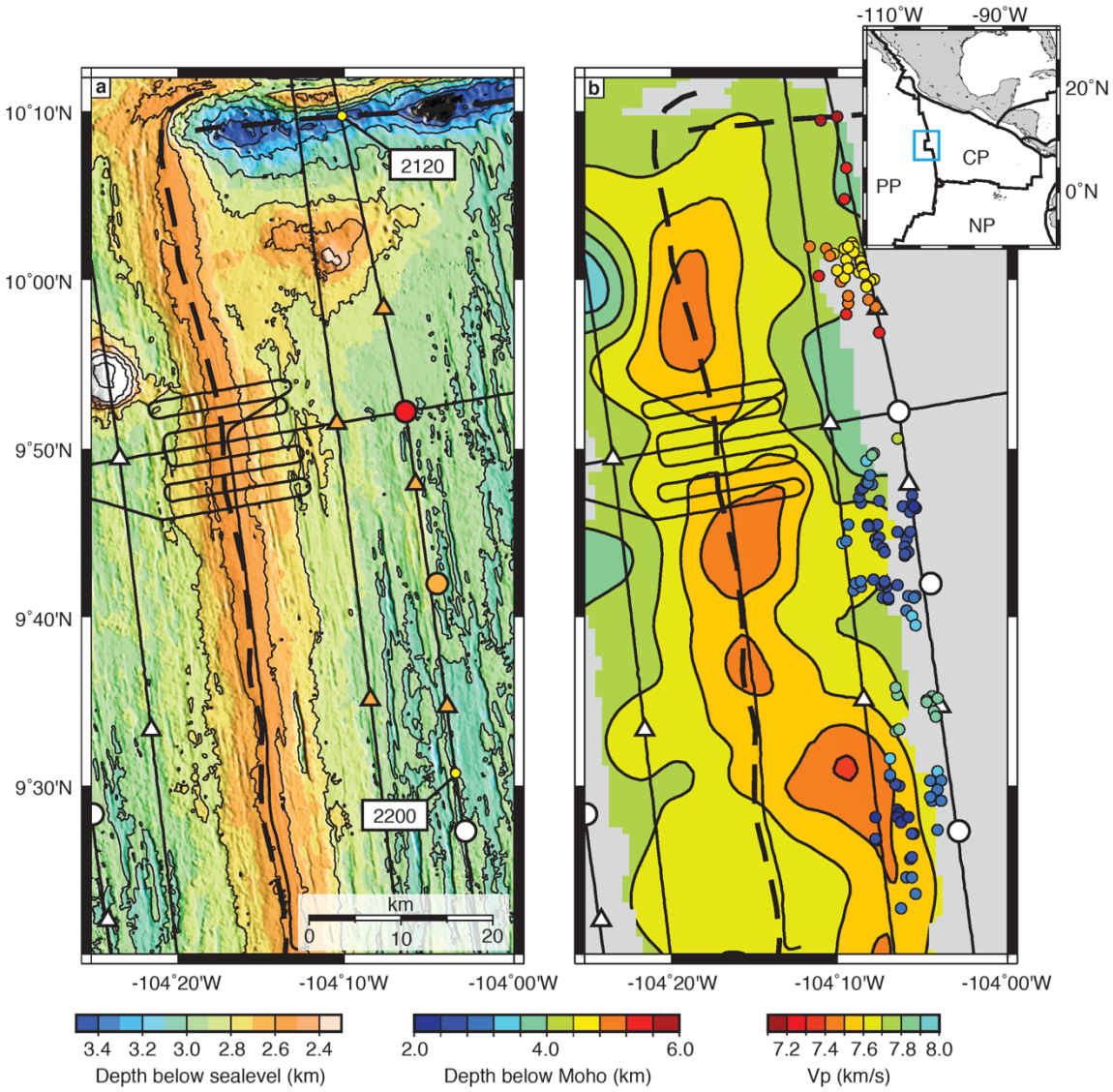

Figure 1. Map of experimental geometry and tomographic image of the mantle low-velocity zone and depth of mantle reflector. (a) Map of the 9°50'N region of the East Pacific Rise, showing locations of three-component ocean bottom seismometers (circles) and hydrophones (triangles) used to record air gun shots fired along tracks shown by the solid black lines. Orange circles and triangles indicate instruments that recorded mantle *P*-wave reflections (*PaP*); red circle corresponds to record sections shown in Figure 2 and whose associated shot locations (yellow circles) are labeled. Dashed black line shows the location of the plate boundary. (b) Tomographic image of mantle *P*-wave velocity from Toomey et al. (2007); contour interval is 0.1 km/s. Colored circles show locations and depths of *PaP* bounce points on the mantle reflector. Inset shows regional location of study area: PP = Pacific Plate, CP = Cocos Plate, and NP = Nazca Plate.

producing asymmetric travel-times about the receivers (Figure 2). The amplitude versus

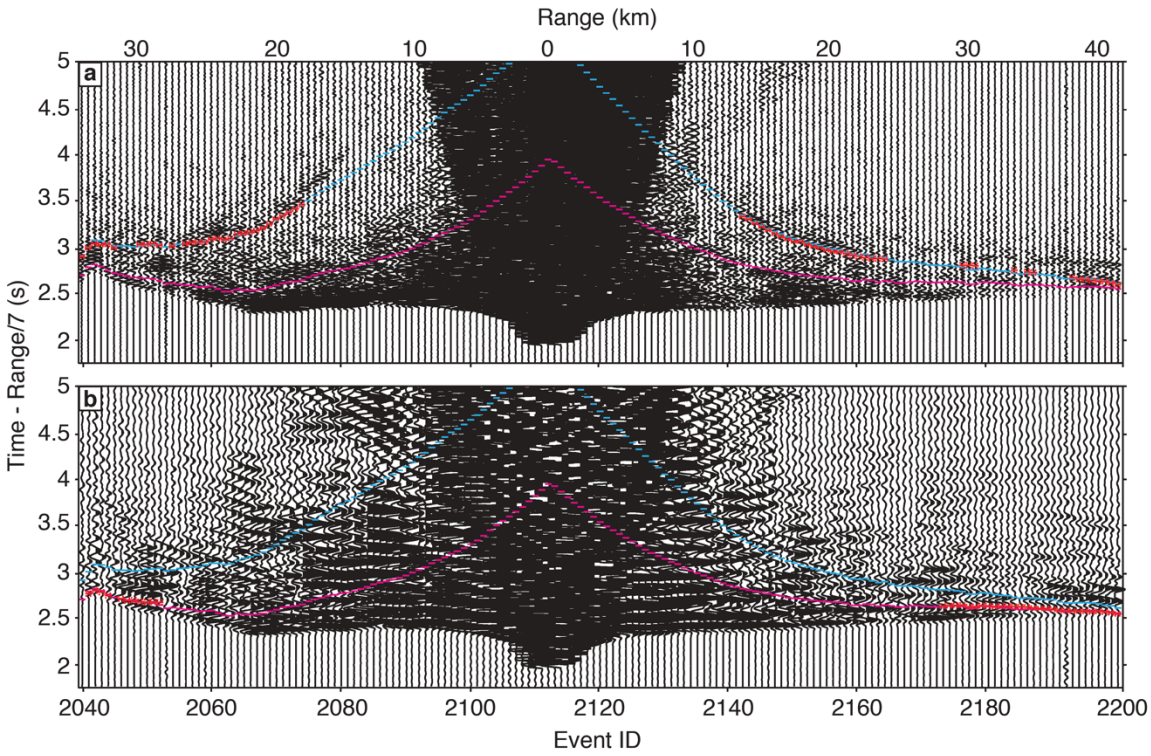

Figure 2. Vertical record sections for OBS 64 shown in Figure 1. (a) Record section band-pass filtered between 20-60 Hz showing the tra picks for *PaP* (red ticks), as well as the best fitting travel-time curves for *PaP* (blue lines) and *PmP* (magenta lines). Note the large amplitude *PaP* arrivals present at offsets ranging from 15 to 25 km and the later arrivals to the north of the receiver. (b) As in (a), except band-pass filtered between 5-20 Hz. Shown are travel-time picks for *PmP* (red ticks). Both record sections are fixed scaled and plotted with a reduction velocity of 7 km/s.

offset behavior of the *PaP* phase is difficult to determine, as they are marked by intermittent energy loss at various offsets and are sometimes difficult to observe owing to low signal-to-noise ratios. However, the arrivals systematically display large amplitudes out to ~30 km offsets. Of note, is that these reflections are restricted to the northeastern portion of the study are and not clearly observed elsewhere within the Undershoot data.

Our analysis includes travel-times from 568 *PaP* arrivals identified through manual picking and cross-correlation. We cross-correlated the characteristic *PaP* waveform (see section 3.1) with other traces to identify groups of *PaP* arrivals and assigned picking uncertainties between 20-30 ms to these arrivals depending on the magnitude of the

correlation coefficient and signal-to-noise ratio of the data. Following this, we further inspected and modified these arrivals according to local trends in the *PaP* waveforms. The root-mean squared (RMS) picking uncertainty of the arrivals is 22.5 ms.

3.0 Methods

3.1 Travel-Time Inversion for Interface Geometry

Seismic imaging is conducted using travel-time data and an iterative tomographic technique (Toomey et al., 1994; Dunn et al., 2005) to construct a 3-D velocity model and 2-D Moho interface to constrain the geometry of the reflector. To construct our starting model, we interpolated the 2-D velocity models and crustal thickness measurements previously constrained using ~7000 *Pg* and ~2400 *PmP* travel-times (Canales et al., 2003) onto a 3-D grid with spacing of 200 m in the x-, y-, and z-dimensions. The Moho interface is included as a gridded surface whose lateral positions are coincident with the velocity model's x and y positions, but whose z positions are allowed to vary independently from the z positions of the velocity model. Perturbational nodes for the model are spaced every 2 km in the ridge-parallel and perpendicular directions, whereas nodes are spaced every 250 m in the z-direction. Perturbational nodes for the interface are spaced every 2 km in the ridge-parallel and perpendicular directions. Model parameters for azimuthal anisotropy are excluded from the inversion. We then invert the travel-times from the previous analysis of Canales et al. (2003), with modified picking uncertainties (mean uncertainty of 10.7 and 25 ms for *Pg* and *PmP*, respectively), in addition to ~3000 line-crossing *Pg* arrivals not included in the analysis of Canales et al. (2003) to constrain the three-dimensional crustal velocity structure and crustal thickness; the resulting model is similar to the 2-D results and converged to a RMS of 10.7 (χ^2=1.0) and 25.8 ms (χ^2=1.07) for *Pg* and *PmP*, respectively. This 3-D crustal model is then used as the starting model for subsequent

inversions of the 568 *PaP* arrivals to determine the approximate depth and geometry of the shallow mantle reflector. The initial interface for the *PaP* inversions is draped from a smoothed version of the seafloor at 10.6 km depth with a homogenous sub-crustal velocity of 7.8 km/s; a change of 0.2 km/s in the sub-crustal velocity would change the interface depth by less than 400 m. In these inversions, we only invert for the interface geometry and avoid perturbations to velocity.

3.2 Amplitude Versus Offset Analysis

Amplitude versus offset (AVO) analysis, in conjunction with phase-weighted stacking (PWS), is used to elucidate the potential lithology of the contact characterizing the reflective interface. AVO for the *PaP* events is examined by aligning a subset of good quality *PaP* arrivals (events 2142-2164 on OBS 64) via static correction using the manually-picked arrival time of each reflection event (Appendix A, Figure S4). The AVO trend is compared with theoretical reflection coefficients for a *P*-wave incident upon a half space interface (Appendix A, Figures S4c-f). In all cases, the incident layer is residual mantle peridotite, or harzburgite (Vp = 7,800 m s^{-1}; Vs = 4,100 m s^{-1}; ρ = 3,130 kg m^{-3}), and the physical properties of the lower layer vary according to the expected lithologies within the shallow mantle and were chosen on the basis of previous work (Durant & Toomey, 2009; Nedimović et al., 2005): dunite (Vp = 8,500 m s^{-1}; Vs = 4,710 m s^{-1}; ρ = 3,500 kg m^{-3}), lherzolite (Vp = 8,000 m s^{-1}; Vs = 4,300 m s^{-1}; ρ = 3,400 kg m^{-3}), gabbro (Vp = 6,900 m s^{-1}; Vs = 3,770 m s^{-1}; ρ = 2,850 kg m^{-3}), and gabbro-melt (Vp = 3,200 m s^{-1}; Vs = 0 m s^{-1}; ρ = 2,900 kg m^{-3}). Owing to the low to moderate signal-to-noise ratio of the *PaP* and *Pg* events in the 5-20 Hz range, the characteristic waveforms of *PaP* and *Pg* are determined using PWS on the events used in the AVO analysis; PWS uses the coherence of the instantaneous phase of a signal to enhance the signal-to-noise ratio of the stack, thus

enabling the detection of weak, coherent signals in the presence of noise (Schimmel & Paulssen, 1997). The characteristic waveforms are then compared to determine if the *PaP* arrivals are phase-inverted relative to the source (Appendix A, Figure S4b), as *Pg* is representative of the source waveform.

3.3 Finite-Difference Waveform Modeling

We use 2-D finite-difference waveform modeling to calculate synthetic seismograms to further assess the physical properties of the shallow mantle reflector. We use the finite-difference program E3D (Larsen & Harris, 1993) using a Ricker wavelet as a source (15 Hz). Waveform models consisted of a 100-km-long, rise-parallel cross-section that included a 3-km-deep water layer, a 7-km-thick crust, a sharp crust-mantle boundary, and a 12-km-thick mantle layer (Figure 3). Embedded in the mantle is a thin (50-100 m thick), segmented seismic discontinuity, the lithology and geometry of which is motivated by the AVO and tomography results. We perform over 30 separate waveform modeling experiments where we varied the length, thickness, spatial extent, continuity, depth, and physical properties of the upper mantle anomaly in order to characterize models whose synthetic waveforms were comparable to the observed data on OBS 64. We also used waveform modeling to explore the effects of embedded layers on the resultant waveforms; we varied the thickness, lateral continuity, lithology, and depth of these features. The waveform models are used for qualitative comparison with the data and are not intended to fully match the observed waveforms.

4.0 Results

Our preferred model converged to a RMS of 24.1 ms (χ^2=1.23) for *PaP*. Our results constrain two discrete sections of the interface located at different depths, separated by a gap where no *PaP* reflections are observed (Figure 1b). The southern interface is located

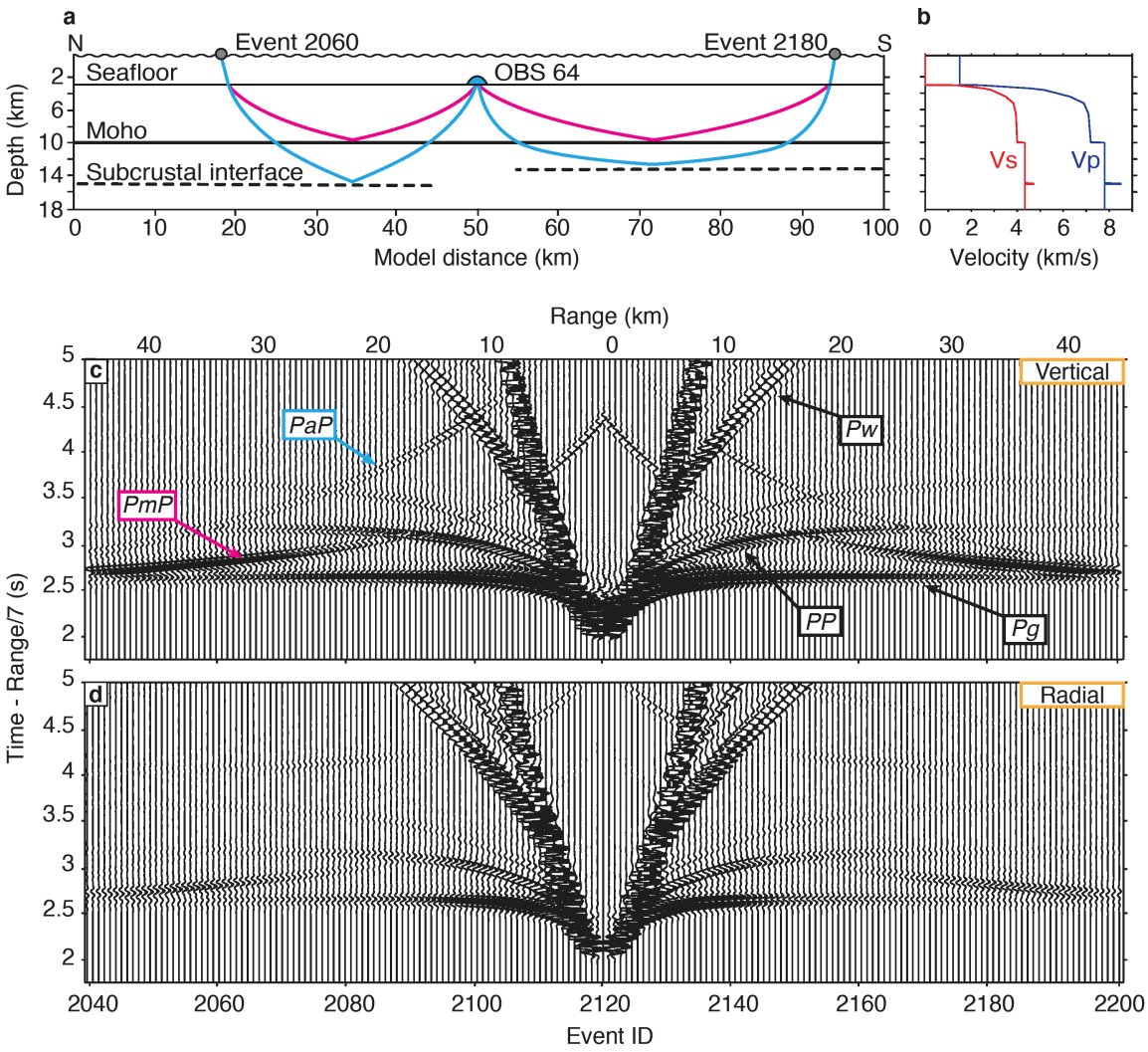

Figure 3. Finite-difference model and synthetic record sections for a model with a 100-m-thick dunite layer embedded within the mantle. (a) Illustration showing the geometry of the finite-difference models and example raypaths for *PmP* (magenta lines) and *PaP* (blue lines) for traces shown in (c) and (d). (b) *P*- and *S*-wave velocity profiles for the finite-difference model. The velocity jump at a model depth of 15 km, corresponding the northern portion of the model space, this represents the velocity of dunite. (c) Synthetic vertical record section showing large-amplitude *PaP* arrivals between 15-25 km offsets. (d) Synthetic radial record section showing lack of *S*-wave arrivals. Record sections are band-pass filtered between 5 and 20 Hz; amplitudes are fixed scaled.

approximately 2 to 4 km below the Moho, whereas the northern reflector is located between 4 and 6 km below the crust; the bounce points off of the interface for *PaP* arrivals used in the inversion are shown in Figure 1b. The lateral variations in the depth of the reflector beneath the Moho are much larger than any that could be produced by uncertainties in the

mantle velocity structure. We note that there is a first-order relationship between the depth of the interface and the location of the mantle low-velocity zone (Toomey et al., 2007), and by inference, regions of on- and off-axis mantle upwelling (Figure 1).

The similarity of the *PaP* and *Pg* waveforms indicates that the reflections originate at a sharp low- to high-velocity discontinuity with increasing depth. *P*-wave reflections originating from such a boundary yield a reflection that is in phase with the incoming *P*-wave (Appendix A, Figures S4c,d), whereas those generated from a high- to low-velocity discontinuity are phase inverted relative to the incoming *P*-wave (Appendix A, Figures S4e,f). The theoretical reflection coefficient for a discontinuity between harzburgite and a layer characterized by higher velocities (e.g., dunite and lherzolite) is consistent with the similar polarity between the *PaP* and *Pg* phases (Appendix A, Figure S4b). Such a contact is also consistent with the observations, as it yields *P*-wave reflections whose amplitude generally increases with offset. A contact between harzburgite and dunite, as opposed to lherzolite, produces a larger reflection coefficient with offset, which is more likely to yield observable reflections. Moreover, neither high velocity layer yields appreciable *S*-wave reflections.

Waveform modeling further suggests that the reflections originate from a low- to high-velocity contact. Such a contact generates reflections that are similar to the AVO trend of those observed in the data, with high amplitudes present at large (15-30 km) offsets (Figure 3). We note that the amplitude of the *PaP* arrival can be affected by constructive interference of reflections from the top and bottom of a high-velocity layer embedded in a lower velocity layer. Our waveform modeling indicates that the tuning thickness of the layer is approximately 100 m, such that a much thinner layer would fail to yield large-amplitude *P* reflections and a much thicker layer would yield paired top and bottom

reflection events of opposite polarity, producing a more complex waveform than is observed. The simplicity, positive polarity, and relatively large and variable amplitude with offset of the *PaP* waveforms are consistent with tuning effects arising from a seismic anomaly that is close to 100 m in thickness. At smaller scales, our data cannot distinguish between a single layer and an anastomosing feature. The inclusion of thin (tens of meters thick), solidified gabbroic layers within the high-velocity layer reduces the amplitudes of the *PaP* arrivals between ~15-25 km offset (Appendix A, Figure S5). The inclusion of a thin (~5 m thick) melt lens yields the opposite effect, increasing the amplitude of the *PaP* arrivals between ~15-25 km offset (Appendix A, Figure S6). Indeed, a laterally discontinuous melt lens may give rise to spatially limited, large-amplitude *P*-wave reflections on the vertical component, though it also produces significant *S*-wave energy on the radial component.

5.0 Discussion

We suggest that the mantle reflections originate from a contact that is genetically linked to melt migration processes. AVO of the *PaP* arrivals and the similar polarity between the *Pg* and *PaP* waveforms suggest that the reflections originate from a contact between harzburgite and dunite, a structural relationship frequently observed in the Oman ophiolite. Within the Oman ophiolite, dunites comprise 5 to 15% of the exposed mantle section (Lippard et al., 1986). A replacive origin for these features is inferred on the basis of field relationships and geochemical data, suggesting dunites represent dissolution channels that facilitate focused porous flow (Kelemen et al., 1995; Kelemen & Aharonov, 1998). On the basis of these observations, we suggest that the reflectors are sub-horizontal dunite/dissolution channels.

Alternatively, the observed reflections may originate from a contact between harzburgite and lherzolite and unrelated to melt migration. Several studies have noted the presence of cpx-harzburgites, or basal lherzolites, near the lithosphere-asthenosphere boundary in ophiolites, which have a more 'fertile' character than typical harzburgite (Godard et al., 2000). These rocks are ascribed to various processes, the predominant being a lower degree of partial melting, which can develop in a propagating and failing ridge system (Takazawa et al., 2003). Alternatively, they may be generated during the opening of a propagating ridge in slightly older lithosphere, where the thermal erosion of the pre-existing lithosphere by the asthenospheric mantle produces a melt-freezing reaction at the expense of the lithospheric mantle (Godard et al., 2000). It is unlikely, however, that such processes have previously or are currently present within our study area. Furthermore, the comparatively pervasive nature of mantle dunites provides a more likely explanation for the observed reflections, as dunite contacts yield reflections that are more comparable to the observations.

The apparent lack of *S*-wave reflections indicates the dunite channels are void of melt, suggesting they may represent relict melt channels or are subject to time-dependent behavior in melt generation or extraction processes. Time-dependent melt generation, for instance, may be caused by a heterogeneous distribution of a low-melting-temperature component that gives rise to variations in the vertical propagation of melt (Sparks & Parmentier, 1991). Similarly, episodic melt extraction may be caused by the expansion and compaction of the matrix in response to variations in melt flux, resulting in the propagation of porosity waves through the solid matrix (Spiegelman, 1993a). This would result in periods of rapid extraction, which serve to drain the channels, alternating with episodes of replenishment. During one of these latter episodes, any remaining melt may crystallize or

the channel could lack melt entirely. Thus, the absence of *S*-waves associated with the *PaP* arrivals suggests that the melt channels are either frozen or exhibit time-dependent behavior, such that a majority of melt flux within the conduits occurs as porosity waves.

The sub-horizontal dunite channels may be related to magmatic focusing at the base of the lithosphere. Numerical modeling supports focused porous flow beneath permeability barriers generated at the base of the lithosphere as a mechanism for magmatic focusing at mid-ocean ridges (Hebert & Montési, 2010; Rabinowicz & Ceuleneer, 2005). This mechanism is predicated on the crystallization of vertically percolating melts as they propagate through the thermal boundary layer (TBL) at the lithosphere-asthenosphere boundary, forming a permeability barrier. Crystallization-driven decompaction of the porous matrix beneath the barrier forms a high-porosity channel that follows the slope of the TBL. Magma is consequently channelized beneath the permeability barrier and focused to the ridge axis. Dissolution could take place within such a channel and result in the formation of dunite. This process is supported by observations of dunitic-troctolitic horizons within the Maqsad area of the Oman ophiolite, which are inferred to represent remnants of melt migration within such melt-focusing channels (Rabinowicz & Ceuleneer, 2005); in this case, the lenses of troctolite represent crystallized melt, whereas the host dunite was formed as melt percolated into the surrounding decompacted channel and subsequently dissolved orthopyroxene. We therefore use a simple half-space cooling model to calculate the 1150°C, 1200°C, 1250°C, and 1275°C isotherms to determine if the depths of the imaged dunite channels correlate with the predicted temperature of permeability barrier formation. Indeed, the depths of the interfaces lie close to the 1250°C and 1275°C isotherms (Figure 4). This, combined with the correlation between the interface depths and pattern of mantle melt delivery in the study area, suggest the interfaces

are thermally controlled and may have formed *in situ* horizontally via dissolution by

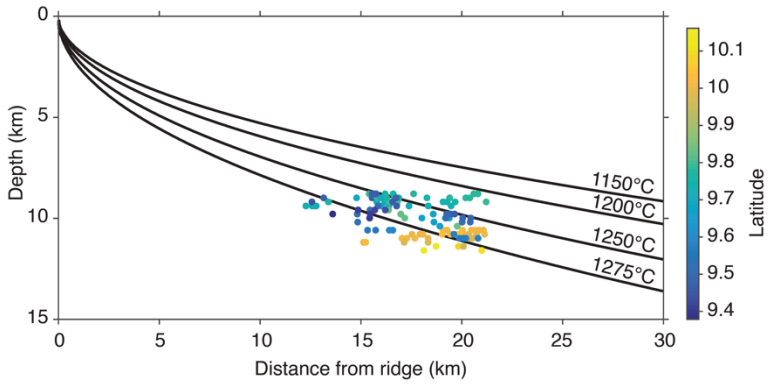

Figure 4. Isotherms calculated using a half-space cooling model of oceanic lithosphere compared to depth of bounce points from the mantle interfaces. Bounce points are colored based upon their latitude.

focused, lateral porous flow.

6.0 Conclusions

Analysis of seismic refraction data collected on the East Pacific Rise between 8°15'N and 10°10'N reveals the presence of off-axis, mantle reflectors to the east of the rise axis between 9°30'N and 10°10'N. The polarity and amplitude variations of the reflections indicate they originate from harzburgite-dunite contacts within the topmost mantle. The dunite layers are deeper near the Clipperton transform fault to the north, reaching a maximum depth of approximately 12 km below seafloor or 6 km below the Moho. While mantle dunites are replacive features formed via dissolution, the correlation of the layer's geometry with patterns of mantle upwelling along the EPR and the predicted isotherms, suggests the dunite layer is thermally controlled. On the basis of these results, we propose the dunite layers formed *in situ* and are genetically linked to focused melt flow along the base of the lithosphere. This interpretation is consonant with field observations in ophiolites and numerical models, which suggest the existence of melt channels at the lithosphere-asthenosphere boundary.

7.0 Bridge

Chapter II presented evidence for sub-horizontal dunite channels beneath mid-ocean ridges that may facilitate magmatic focusing from the mantle to the ridge axis. Reflections sourced from these dunite channels, however, were not consistently observed at the East Pacific Rise, suggesting they may be spatially discontinuous and produce along-axis variations in mantle melt delivery. In Chapter III, I examine how patterns in mantle melt delivery influence the structure of the crustal magma reservoir, oceanic crust, and along-axis variations in ridge-crust processes, such hydrothermal activity, by imaging the segment-scale velocity structure of the Endeavour segment of the Juan de Fuca Ridge. Using these velocity images, I estimate the thermal structure and melt distribution beneath the ridge, revealing a segment-scale skew between the mantle and crustal magmatic systems. Synthesizing these results with geophysical and petrological observations, I provide a conceptual model for how this skew controls magmatic, tectonic, and hydrothermal processes at mid-ocean ridges.

CHAPTER III

SEISMIC IMAGING AND PHYSICAL PROPERTIES OF THE ENDEAVOUR SEGMENT: EVIDENCE THAT SKEW BETWEEN MANTLE AND CRUSTAL MAGMATIC SYSTEMS GOVERNS SPREADING CENTER PROCESSES

From Arnoux, G. M., Toomey, D. R., Hooft, E. E. E., and Wilcock, W. S. (2018). Seismic imaging and physical properties of the Endeavour segment: Evidence that skew between mantle and crustal magmatic systems governs spreading center processes**.** In review at *Geochemistry, Geophysics, Geosystems.*

1.0 Introduction

The global mid-ocean ridge system accounts for ~75% of Earth's annual magma budget (Crisp, 1984). Magmatic systems beneath spreading centers drive high- and low-temperature hydrothermal activity that modulates the long-term chemistry of the ocean, hydrates the crust and mantle, supports novel ecosystems, and deposits valuable mineral resources. The fundamental unit of the global mid-ocean ridge system is referred to as a ridge segment. Within a single ridge segment there are systematic variations in tectonic, volcanic, and hydrothermal processes (Kent et al., 2000; Langmuir et al., 1986; Macdonald et al., 1988). Understanding how mass and energy are transferred within a ridge segment requires mapping mantle and crustal magmatic systems and their relationship to hydrothermal and tectonic processes. Maps of the three-dimensional seismic structure can constrain the size, shape, and location of magma reservoirs, the connections between magmatic and hydrothermal processes, and be used to infer the thermal structure (Carbotte

et al., 2012, 2013; Detrick et al., 1987; Dunn et al., 2000, 2013; Kent et al., 1993, 2000; Seher et al., 2010; West et al., 2001).

Much of what we know regarding mid-ocean ridge crustal magmatic systems is derived from seismic studies of the fast-spreading East Pacific Rise (EPR) (Carbotte et al., 2013; Dunn et al., 2000; Goss et al., 2010). In the cross-axis direction, EPR magmatic systems are characterized by a steep-sided mush zone that is often capped by a narrow, thin melt lens (Dunn et al., 2000). In the rise-parallel direction, EPR crustal magmatic systems are to first-order, two-dimensional features, though there are subtle 3-D structures at a variety of scales (e.g., Toomey et al., 1990; Kent et al., 1993, 2000; Wilcock et al., 1993; Hooft et al., 1997; Carbotte et al., 2013). To what degree crustal magmatic systems at other spreading rate ridges resemble their fast-spreading counterparts is not well known.

At the intermediate-spreading, back-arc Eastern Lau Spreading Center, a narrow, seismic low-velocity volume is imaged into the mid-crust beneath all surveyed ridge segments (Dunn et al., 2013). At the intermediate-spreading Juan de Fuca Ridge (JdFR), an axial magma lens (AML) reflector underlies most ridge segments, though it is less laterally continuous and its along-axis depth variation is more pronounced than that at the EPR (Van Ark et al., 2007; Carbotte et al., 2006, 2008). This reflector may overlie a lower crustal mush zone that is comparable to the EPR, with steep sides that are consistent with rapid convective cooling at lower crustal depths (e.g., Henstock et al., 1993; Hasenclever et al., 2014), and with a mush zone that extends to the Moho and varies slowly along axis, as one might expect for a largely 2-D (vertical) melt transport through the lower crust (Carbotte et al., 2013; Sinton & Detrick, 1992; Toomey et al., 1990). Alternatively, the lower crustal mush zone at intermediate-spreading ridges may be more three-dimensional and consistent with focused melt transport through the lower crust, along-axis transport of

magma at mid-crustal depths, and uneven rates of hydrothermal cooling. Such along-axis variations in melt transport could have significant implications for the observed segmentation of mid-ocean ridges defined by systematic along-axis variations in tectonic and magmatic processes.

The origin of mid-ocean ridge segmentation is commonly attributed to three-dimensional mantle upwelling (Macdonald et al., 1988, 1991; Schouten et al., 1985). In this view, the supply of magma from the mantle is enhanced beneath intrasegment highs (Francheteau & Ballard, 1983; Macdonald et al., 1988; Whitehead et al., 1984). This model would thus predict thickened crust beneath axial depth minima or segment-scale redistribution of magma. Crustal thickness at the 9°N segment of the EPR, however, does not correlate with ridge crest depth (Barth & Mutter, 1996; Canales et al., 2003; Toomey & Hooft, 2008). The thickest crust is located in the wake of the 9°03'N OSC, whereas thinner crust underlies the segment near 10°N where the ridge crest is shallower (Barth & Mutter, 1996; Canales et al., 2003). Additional observations of segment-scale variations in crustal thickness are required to further assess this hypothesis.

An alternative model for the origin of ridge segmentation is that of skew between the axes of mantle upwelling and plate spreading. At shallow mantle depths, results from the EPR (Toomey & Hooft, 2008; Toomey et al., 2007) and Endeavour segment of the JdFR (VanderBeek et al., 2016) suggests that skew or misalignment between tectonic rifting, mantle divergence, and segment-scale delivery of mantle melt to the crust governs along-axis variations in ridge-crest volcanic, hydrothermal, and tectonic activity. In this model, axis-parallel variations in ridge processes are not simply a function of magma supply or the along-axis redistribution of magma away from a mantle source beneath the center of the ridge segment, as is predicted by the magma supply model (Bell & Buck,

1992; Macdonald et al., 1988, 1991). Rather, the cross-axis offset between the locus of mantle melt supply and the ridge axis governs along-axis variations in ridge crest processes (Toomey et al., 2007; VanderBeek et al., 2016). This model predicts frequent magma injection into the rift, frequent extrusive volcanism, and more vigorous hydrothermal venting that would shape a narrow, robust crustal magmatic system in sites of axis-centered mantle melt delivery. In contrast, sites of off-axis mantle melt delivery would be characterized by less frequent magma injection and extrusive volcanism, less intense hydrothermal activity, comparatively higher degrees of magmatic differentiation, and a weaker crustal magmatic system. To date, however, no studies have imaged the segment-scale structure of the magmatic system in its entirety, from the shallow mantle to upper crust, in regions where skewed mantle melt delivery is observed.

In this study, we utilize seismic tomographic methods to constrain, for the first time, the three-dimensional segment-scale variations in the isotropic and anisotropic velocity structure of the topmost mantle and crust beneath an entire ridge segment. Our results provide new insight into the thermal and magmatic structure beneath the Endeavour segment, in addition to crustal thickness variations beneath the rise axis. We discuss the implications of our results on (1) the magma plumbing system beneath the Endeavour segment, (2) the relationship between skewed delivery of mantle melt and the structure of the crustal magmatic system, and (3) the relationship between crustal thickness, magma supply, and the tectonic evolution of the Endeavour segment.

2.0 Background

The Endeavour segment is a 90-km long intermediate-rate spreading center (57 mm/year (DeMets et al., 2010)) located on the northern end of the Juan de Fuca Ridge (Figure 1). It lies at the southern edge of the diffuse Explorer plate boundary, a deformation

zone that extends to the Cobb overlapping spreading center (OSC) and bounds the southern end of the Endeavour segment (Dziak, 2006) (Figure 1). To the north, the Endeavour segment is bounded by the Endeavour-West Valley (E-WV) OSC. The tectonic history of the Endeavour segment is dominated by series of ridge propagation events. The Cobb OSC, which separates the Endeavour and Northern Symmetric segments by >30 km, propagated northward ~4.5 Ma (Wilson, 1993). At ~0.8 Ma, the Endeavour segment propagated southward, forcing retreat of the Cobb OSC to approximately 47°35'N (Shoberg et al., 1991). Propagation again reversed within the past 0.1 Ma, with the northern end of Northern Symmetric segment currently located at 47°46'N. The E-WV OSC to the north separates the Endeavour and West Valley segments by 15 km and formed within the past 0.2 Ma when the spreading center jumped from the Middle Valley segment to West Valley segment (Figure 1) (Davis & Lister, 1977; Davis & Villinger, 1992).

The central portion of the Endeavour segment hosts five large hydrothermal vent fields that are spaced 2-3 km apart along the ridge axis (Figure 1) (Kelley et al., 2002). These vent fields mine heat from a crustal magmatic system capped by an axial magma lens (AML) that is located 2.1-3.3 km below the seafloor and extends ~20 km along-axis (Van Ark et al., 2007). The vent fields are characterized by significant along-axis

Figure 1 (next page). Bathymetric map of the Endeavour region of the Juan de Fuca Ridge showing the major tectonic features. Solid black lines demarcate plate boundaries. The white arrows show spreading direction and full-spreading rate (Gripp and Gordon, 2002). The green arrow indicates the azimuth of seismic anisotropy within the mantle (this study). Red lines indicate propagator wakes and the gray box outlines the Cartesian coordinate system, in kilometers, for the areas shown in Figures 5 and 7, as well as Figures S4 and S5 in Appendix B. Recent rotation in the Euler pole of the Juan de Fuca—Pacific plate system is indicated (Wilson, 1988). Top left inset, modified from Byrnes et al. (2017), shows the tectonic context of the Endeavour segment. Shown are spreading centers (double lines), transform faults (black lines), direction of ridge migration (thin arrow), the Cascadia megathrust (black line with triangles), and the diffuse Explorer plate boundary (streaked area) (Dziak, 2006).

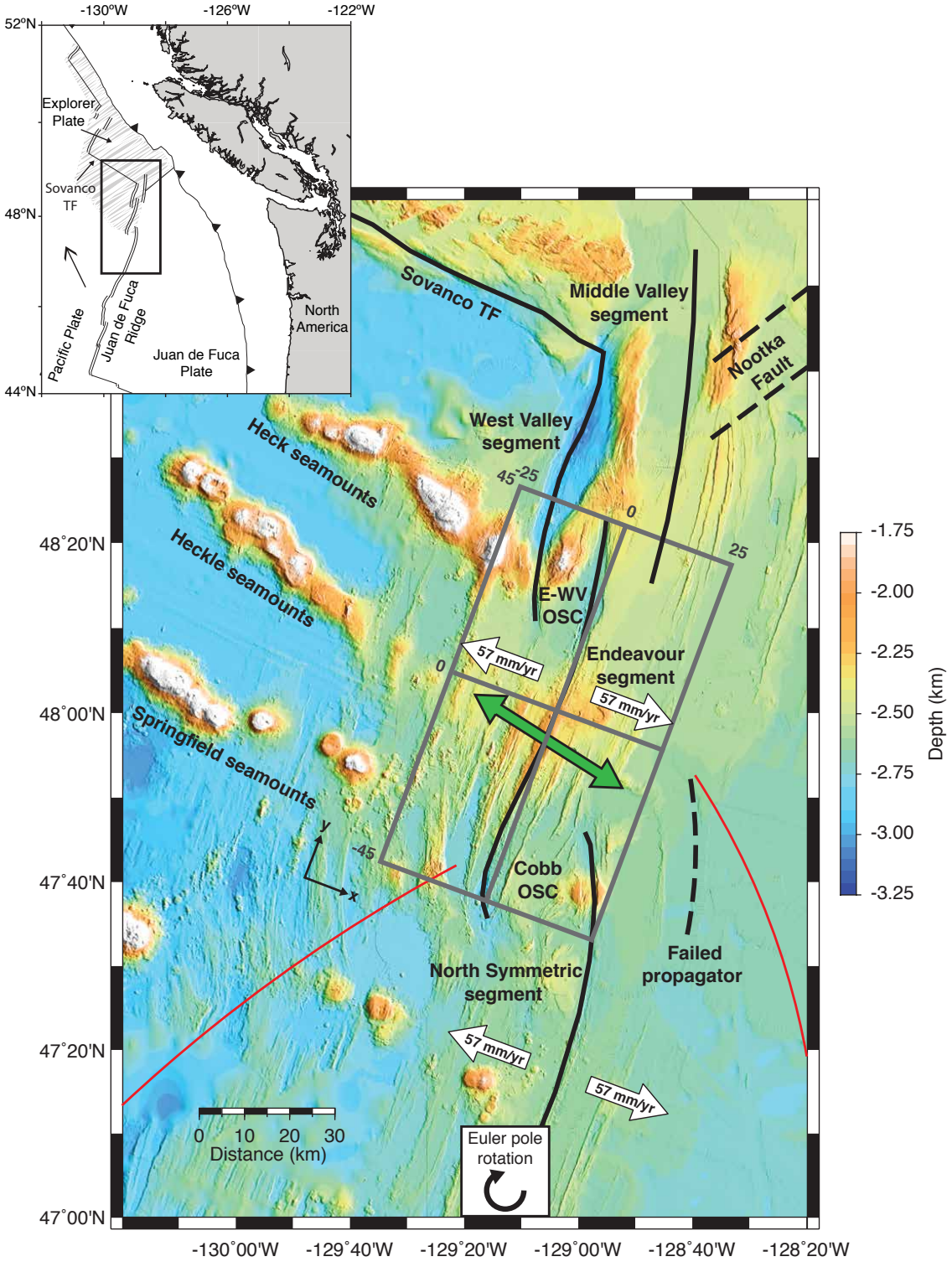

variability in chemistry, temperature (Butterfield et al., 1994; Kelley et al., 2002, 2012), and heat flux (Kellogg, 2011). Along-axis gradients in heat flux correlate with concentrations of seismicity related to recent magma chamber inflation (Wilcock et al.,

2009) and imaged variations in low-velocities above and beneath the AML (Arnoux et al., 2017), with the most intense seismicity and lowest velocities occurring beneath the High Rise and Main Endeavour vent fields, which have the highest heat fluxes (Kellogg, 2011).

A six-year long, non-eruptive spreading event ruptured the Endeavour from 1999-2005 (Weekly et al., 2013). The initiation and termination of the spreading episode were defined by large seismic swarms linked to intrusive volcanism and lateral dike propagation (Bohnenstiehl et al., 2004; Hooft et al., 2010). During the 1999 swarm, the initial pulse of seismicity was distributed along-axis in the region of the imaged AML and subsequently migrated ~12 km south along the Endeavour segment (Bohnenstiehl et al., 2004). The 2005 seismic sequence, marking the termination of the spreading episode, initiated at the northern end of the Endeavour segment near the E-WV OSC and progressed 20 km south toward the segment center over the course of 5 days (Hooft et al., 2010). Smaller dike intrusions on the propagating tip of the West Valley segment were also detected during the 2005 swarm (Hooft et al., 2010; Weekly et al., 2013).

The axial high at Endeavour is located within a 40-km-wide plateau that is elevated 300 m relative the rest of the segment (Carbotte et al., 2008). The plateau is characterized by thickened crust, on the order 0.5-1 km thicker than average flank crust (Carbotte et al., 2008; Soule et al., 2016). It has been postulated that the plateau is the result of enhanced crustal production due to the interaction of the Endeavour segment with a shallow mantle thermal anomaly related to the Heckle Seamount chain (Carbotte et al., 2008). Alternatively, the plateau may be the product of the propagation history of the Cobb OSC, in which the southward migration of the Endeavour segment 0.71 Ma generated thicker crust by tapping melt pooled beneath the Cobb OSC (Soule et al., 2016).

3.0 Experiment Geometry and Data

The seismic data were collected in 2009 during the Endeavour seismic tomography (ETOMO) experiment. The seismic experiment was comprised of 68 four-component (three orthogonal geophones and a hydrophone) ocean bottom seismometers (OBSs) deployed at 64 unique sites that recorded ~5500 air gun shots from the 36 element, 6600 in^3 air gun array of the *R/V Marcus G. Langseth* (Figure 2a). The objective of the experiment was to image the crustal and mantle structure from the segment- to vent-field scales (Arnoux et al., 2017; Soule et al., 2016; VanderBeek et al., 2016; Weekly et al., 2014). To accomplish this, a nested source receiver geometry was used to record data that densely sampled the crust and topmost mantle within a 90-km-by-50-km area centered on the ridge segment (Figure 2a). This nested geometry consisted of three grids: (i) the segment-scale undershoot grid designed to image the topmost mantle structure using six rise-parallel 105-km-long lines shot within 30 km of the ridge axis and two rise-perpendicular lines shot on the northern and southern margins of the experiment; (ii) the crustal grid devised to image the off-axis crustal structure and along-axis variation of the crustal magmatic system, composed of 19 shot lines spaced 1 km apart within a 20-by-60-km^2 area centered on the central plateau of the segment; and (iii) the fine-scale hydrothermal grid designed to image the detailed structure of the shallow crust beneath and near the hydrothermal vents, consisting of the densest shot-receiver distribution within the Endeavour tomography experiment with ten 20-km long shot lines embedded within the center of the crustal grid and for a net spacing of 500 m. Shot spacing along all lines was 450 m. The data have been used to constrain the isotropic and anisotropic *P*-wave velocity structure of the upper crust (Arnoux et al., 2017; Morgan et al., 2016; Weekly et al., 2014), near-axis crustal velocity structure and thickness (Soule et al., 2016), and mantle velocity

and anisotropy structure (VanderBeek et al., 2016). Until now, the data have not been used to image the lower crustal velocity structure and crustal thickness beneath the rise axis.

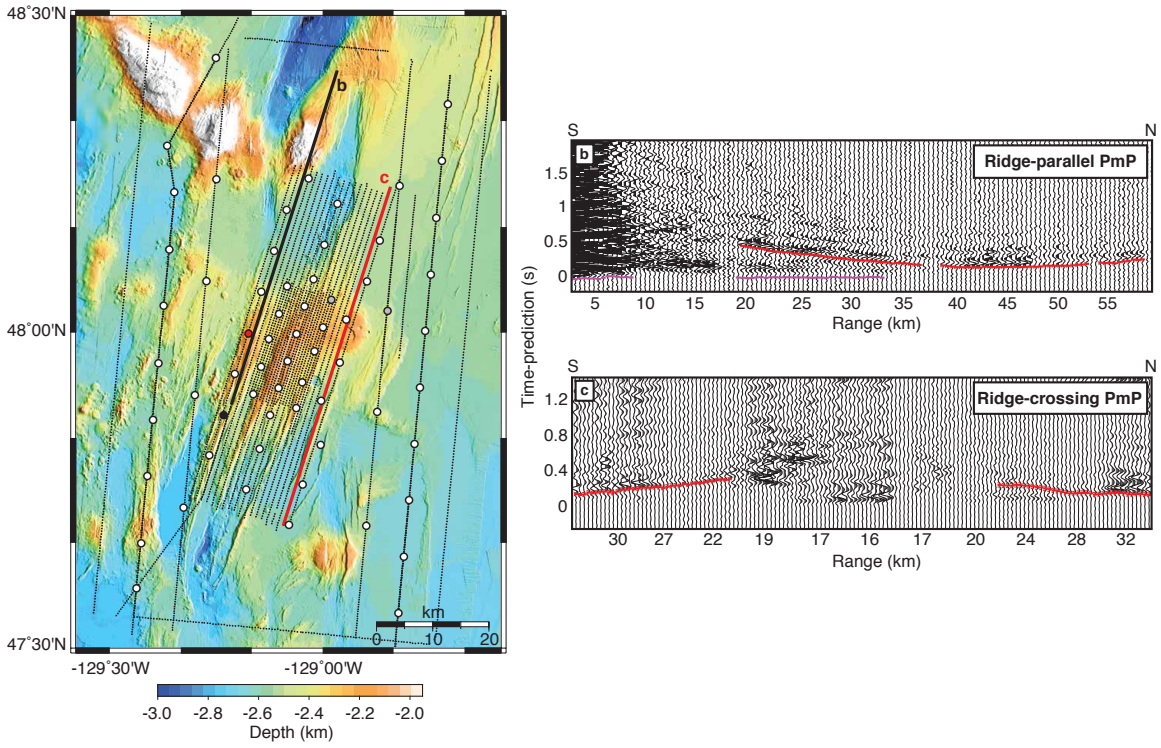

Figure 2. Geometry of the Endeavour tomography (ETOMO) experiment and example record sections. (a) Configuration of the ETOMO experiment, consisting of 68 four-component ocean-bottom seismometers (white circles) recorded ~5500 airgun shots (black dots). Two OBSs did not record useable data (grey circles). Bathymetry is shaded every 100 m. The black circle and thick black lines show the location of the receiver and sources shown in (b), whereas the red circle and thick red line show the location of the receiver and sources shown in (c). (b) Ridge-parallel record section showing *PmP* travel-time picks (red lines with dotted lines showing assigned picking errors) and *Pg* arrivals (Weekly et al., 2014). (c) Record section for ridge-crossing *PmP* arrivals (red dashes). Traces are aligned by range of shots in kilometers. Record sections are plotted after applying a 5-20 Hz bandpass filter and times are zeroed at the predicted *Pg* arrival time for the preferred model to remove complex bathymetric effects.

Our tomographic analysis includes travel-times from 96,155 primary crustal arrivals (*Pg*), 105,000 Moho- (*PmP*), and 12,000 mantle-turning (*Pn*) arrivals. Of the *PmP* picks included, 55,000 are rise-parallel and 50,000 are rise-crossing (Figure 2b and 2c); we detail the process of picking *PmP* arrivals in Text S1. The root-mean squared (RMS) picking uncertainty for the entire *PmP* data set is 18.7 ms. Previous tomography studies

have modeled *Pg* (Weekly et al., 2014) and *Pn* arrivals (VanderBeek et al., 2016) and 40% of the rise-parallel *PmP* (Soule et al., 2016). No previous work has incorporated rise-crossing *PmP* arrivals.

4.0 Tomographic Method

We used a three-dimensional tomographic technique to invert travel-time data to constrain isotropic slowness and seismic anisotropy within the crust and topmost mantle, in addition to Moho depth (Dunn et al., 2005; Toomey et al., 1994). The inverse technique involves computing three-dimensional seismic ray paths between sources and receivers to calculate travel-times through a starting model. The inverse problem is linearized about this starting model to obtain a set of equations mapping model perturbations into travel-time residuals. User-prescribed values for model smoothness and variance are included via additional equations. The model is then updated with a correction calculated via a least squares procedure utilizing either a creeping or jumping inversion strategy (Shaw & Orcutt, 1985), and subsequent iterations are performed until the RMS travel-time residuals converged. Our preferred model converged to a RMS of 11 ($\chi^2 = 1.02$), 16 ($\chi^2 = 0.87$), and 11.2 ms ($\chi^2 = 1.2$) for *Pg*, *PmP*, and *Pn*, respectively. A detailed description of the inversion approach is presented in Appendix B, Text S2.

4.1 Forward Problem

The velocity model is parameterized in terms of slowness with nodes defined on a regular grid aligned with the trend of the ridge axis. Nodes are spaced every 200 m in the x- and y-dimensions and 250 m in the z-dimension. The model extends 90 km in the cross-axis direction, 120 km in the rise-parallel direction, and 11 km beneath the seafloor. The forward problem utilizes a shortest-path ray tracing method that accounts for anisotropic structure (Dunn et al., 2005) and incorporates seafloor topography by vertically shearing

columns within the velocity model to follow local seafloor relief (Toomey et al., 1994). Anisotropic slowness is parameterized assuming a hexagonal symmetry system on the slowness grid:

$$u(r) = \frac{u_{iso}(r)}{1 + \kappa\{A(r)\cos[2\theta(r)] + B(r)\sin[2\theta(r)]\}}$$

where κ represents the symmetry system and is defined as ±1 (positive and negative for fast and slow symmetry, respectively), u_{iso} is the isotropic slowness, r is the position, θ is the ray azimuth measured from the x-axis at position r, and A and B are scale terms that control the magnitude and azimuthal orientation of the anisotropy symmetry axis (fast or slow axis depending on κ) , defined as $2(A^2 + B^2)^{0.5}$ and $\text{atan}(B/A)/2$, respectively. The modification to this equation, κ, allows for the inclusion of two distinct symmetry systems within the model space that approximate: (i) penny-shaped cracks (slow symmetry axis), characterized by one slow and two fast axes and (ii) olivine-dominated peridotite (fast symmetry axis), defined by one fast and two slow axes. Crustal anisotropy is caused by the alignment of fluid-filled cracks perpendicular to the minimum compressive stress direction, resulting in an axis of symmetry (slow direction of *P*-wave propagation) that is oriented sub-perpendicular to the ridge axis. Mantle anisotropy is the result of lattice-preferred orientation of olivine crystals, in which the crystallographic a-axis of olivine (the fast direction of *P*-wave propagation) aligns parallel to the direction of maximum shear and thus tracks the mantle divergence direction (e.g., VanderBeek et al., 2016). We therefore define κ as a grid with the same dimensions as the slowness model with all crustal and mantle values set to +1 and -1, respectively.

The Moho reflection surface is defined on a separate gridded surface with the same x- and y-dimensions as the slowness grid, but for which the z grid points vary

independently of the slowness grid (Dunn et al., 2005). If the Moho is raised or lowered within the model space, values on the velocity grid are modified to maintain any velocity contrast associated with the interface.

4.2 Inverse Problem

The inverse problem is regularized with damping and smoothing constraints requiring user-defined a priori model uncertainties and smoothing parameters that operate on perturbational models parameterized for isotropic slowness, anisotropy, and Moho depth. The perturbational models for isotropic and anisotropic slowness were composed of rectilinear grids that were denser within 10 km of the ridge axis to reflect the greater number of raypaths; horizontal node spacing was 0.5 km within and 1 km beyond this region. Vertical node spacing varied to account for the decrease in raypath density with depth, with a minimum spacing of 500 m in the upper 3 km of crust and 1 km spacing below. Perturbation nodes for the Moho were spaced every 3 km. The inverse problem is similar to that of Dunn et al. (2005) with a modification to their equation A17 to account for the two possible anisotropy symmetry axes:

$$\frac{\partial \alpha'}{\partial \alpha} = \frac{1}{1 + \kappa\{A(r)\cos[2\theta(r)] + B(r)sin[2\theta(r)]\}}$$

where α'and α are anisotropic and isotropic slowness perturbations, respectively.

We sought to minimize a functional of the form:

$$s^2 = \Delta t'^{C_d^{-1}} \Delta t + \lambda_p (m_0 + \Delta m)' C_m^{-1} (m_0 + \Delta m)$$

$$+\lambda_V (m_0 + \Delta m)' C_V^{-1} (m_0 + \Delta m) + \lambda_H (m_0 + \Delta m)' C_H^{-1} (m_0 + \Delta m)$$

where Δt is a vector containing the difference between observed and calculated travel-times; C_d is a diagonal matrix containing the data variance composed of the squares of travel-time uncertainties; m_0 is a vector of the cumulative perturbation to the isotropic,

anisotropic, and interface model parameters from previous iterations; Δm is a vector containing model perturbation to be determined; C_m is a diagonal matrix containing the a priori model variance; C_v and C_h are matrices that apply vertical and horizontal nearest-neighbor smoothing, respectively, to each model parameter; and λ_p, λ_v, and λ_h are weighting parameters that define the relative importance of damping, vertical smoothing, and horizontal smoothing constraints, respectively.

5.0 Results

Previous results constrain the isotropic and anisotropic structure of the upper crust (Weekly et al., 2014) and topmost mantle (VanderBeek et al., 2016), as well as isotropic structure of off-axis lower crust and crustal thickness (Soule et al., 2016). Our study is the first to synthesize these results and provides novel constraints on the crustal velocity structure and thickness beneath and near the rise axis and the relationship between crustal and upper mantle structures along an entire ridge segment. We describe the characteristic velocity structure of different regions within the study area (Figure 3), depth variations in the velocity structure (Figure 4), along- and cross-axis velocity variations (Figure 5), and compare bathymetry, crustal thickness, and velocity (Figure 6). We assess the resolution of the preferred model by analyzing the spatial distribution of raypaths and conducting synthetic checkerboard tests in Appendix B, Text S3 and Figure S1. We also describe the mantle and crustal anisotropic structure of our preferred model in Appendix B, Text S2 and Figure S2, respectively.

5.1 Mantle Velocity Structure

Velocities within the mantle are low along the entire length of the Endeavour segment and similar to those of VanderBeek et al. (2016) (Figure 6e). The north-south trend of the mantle low-velocity zone (MLVZ) connects the two OSCs bounding the

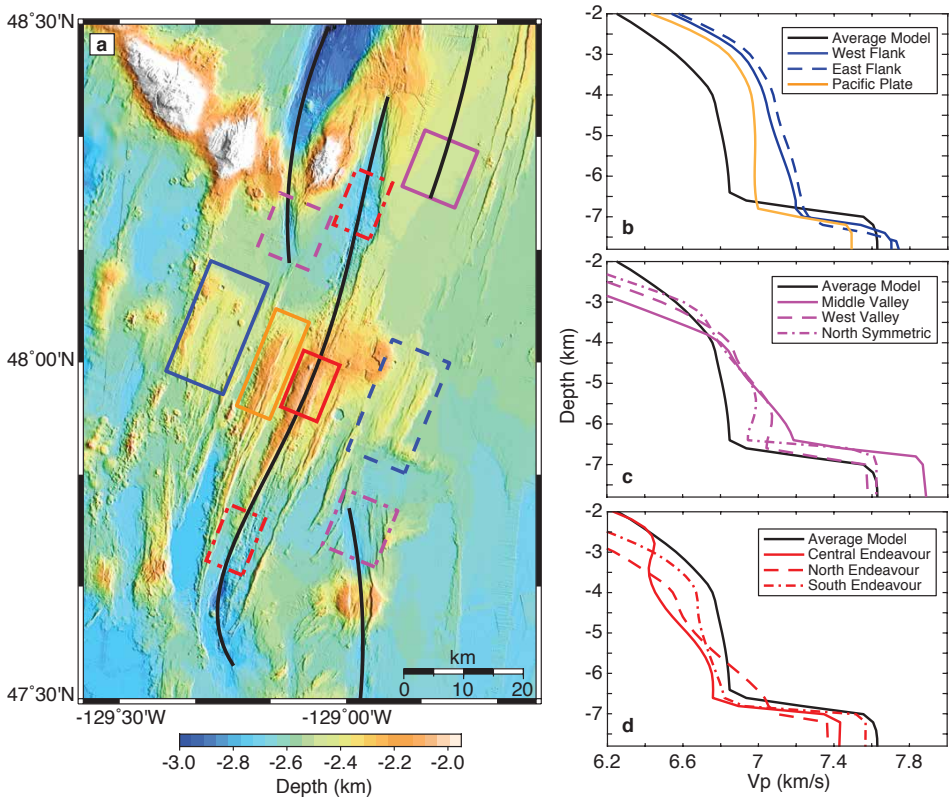

Figure 3. One-dimensional *P*-wave velocity profiles. (a) Bathymetric map with regions for which average 1-D profiles are calculated (colored boxes). The traces of the segments are shown by black lines and the vent fields by green stars. (b) 1-D vertical profiles for the western (dashed blue) and eastern flanks of the segment center (solid blue), as well as for a region not associated with thickened ridge flank crust (solid orange). (c) Profiles for currently and formerly propagating limbs: Middle Valley (solid magenta), West Valley (dashed magenta), and North Symmetric (dotted magenta). (d) Profiles for the southern (dotted red), northern (dashed red), and central (solid red) portions of the Endeavour segment. The horizontal average of the isotropic component of the preferred velocity model (solid black) are shown in (b) through (d) for comparison.

segment, subparallel to the regional trend of the northern Juan de Fuca plate boundary, and is rotated anticlockwise relative to the trend of the ridge axis. Moreover, the MLVZ is not perpendicular to the anisotropic component of our model (Figure 6e), as is the case for the fast-spreading EPR (Toomey et al., 2007). The magnitude of the MLVZ is greatest beneath the two OSCs, though three distinct low-velocity minima punctuate the MLVZ beneath the central Endeavour segment (Figure 6e). As a result of the skew between the trend of the

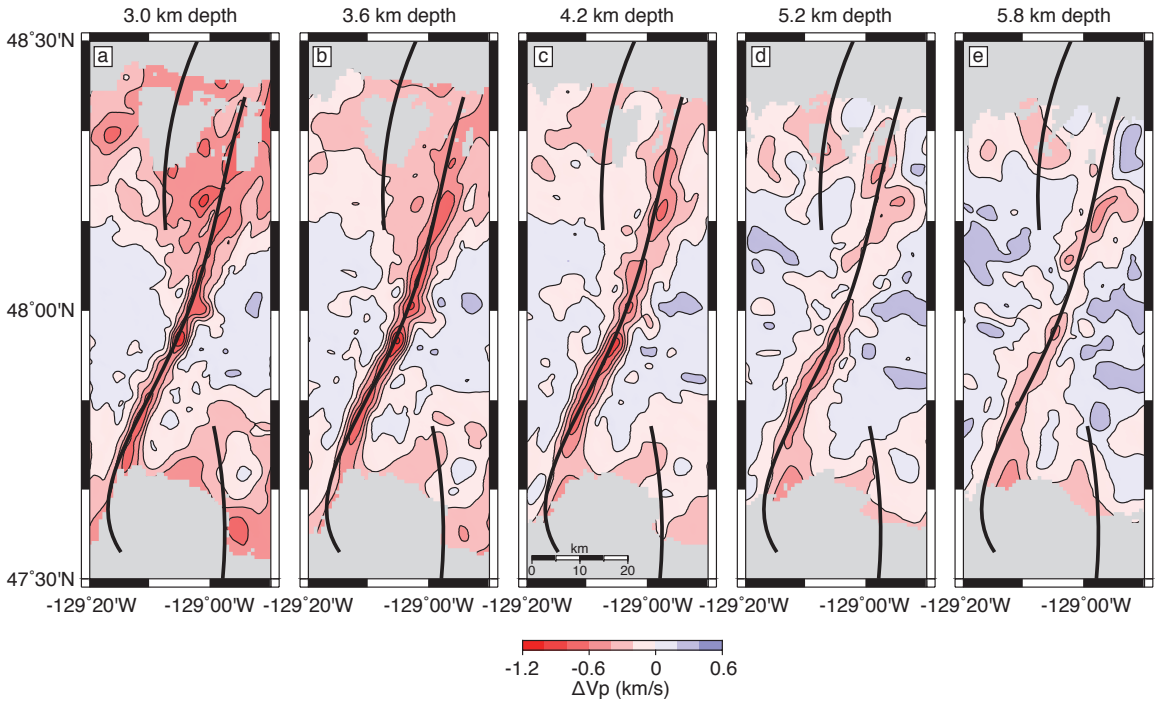

Figure 4. Map-view sections through the preferred velocity model at (a) 3.0 km depth, (b) 3.6 km depth, (c) 4.2 km depth, (d) 5.2 km depth, and (e) 5.8 km depth. Sections show 3-D velocity perturbations relative to the off-axis 1-D velocity model shown in Figure 3b (orange line). The plate boundary (dashed black line) is indicated on each section. The contour interval is 0.1 km/s. Sections are masked where the density of raypaths, or the derivative weight sum (DWS) (Toomey & Foulger, 1989), is less than 10 (see Appendix B).

MLVZ and that of the ridge axis, the cross-axis offset of the MLVZ minima with respect to the ridge axis varies along the segment. The two southern anomalies are roughly aligned with the ridge axis, though the southernmost anomaly is slightly offset to the east by approximately 1-2 km. Conversely, the northern minimum is offset to the west of the ridge axis by approximately 10 km. Of note is that where the MLVZ is axis-centered, the crustal low-velocity zone is more pronounced, as is ridge topography (Figure 6c).

5.2 Crustal Velocity Structure

Average velocity-depth profiles (Figure 3) show significant variability in crustal structure. At the segment center, the flanks of the ridge axis are characterized by the highest average crustal velocities in the study area, increasing from 6.6 km/s at a depth of 2 km to

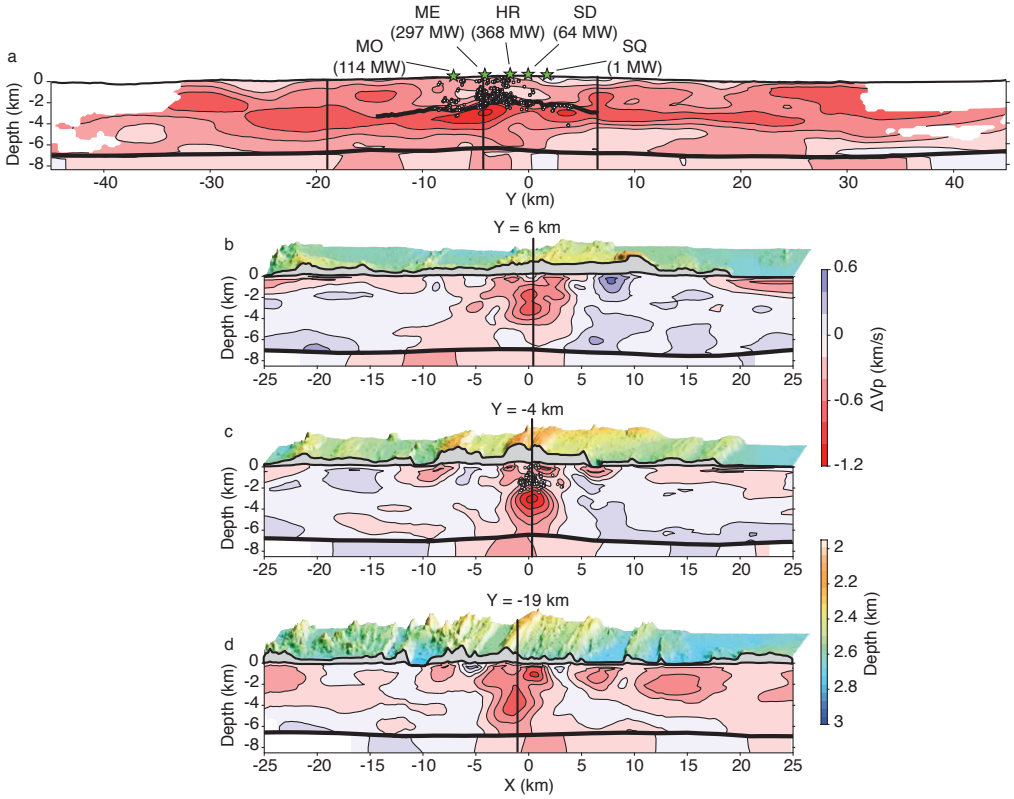

Figure 5. Vertical slices through preferred velocity model. (a) Vertical section showing average velocity perturbations within 400 m of the ridge axis. The axial magma lens reflector (thin black line), Moho (bold black line), hypocenters for earthquakes recorded between 2003 and 2004 (Wilcock et al., 2009) (white circles), and vent fields (green stars) are shown. Vertical black lines show the location of the cross-sections shown in (b-d). (b-d) Vertical sections crossing the ridge axis at (b) Y = 6 km where the mantle magmatic system is offset relative to the ridge axis, (c) Y = -4 km where the mantle magmatic system is aligned with the ridge axis, and (d) Y = -19 km where the magmatic system is slightly offset with respect to the ridge axis. Perspective views of the overlying bathymetry are provided and vertically exaggerated by approximately 35 times. Sections show the Moho (bold black lines), earthquake hypocenters (white circles), and are masked where the DWS is less than 10 (see Appendix B). Vertical black lines show the location of the ridge axis. Velocity perturbations are relative to the off-axis 1-D velocity model shown in Figure 3b (orange line).

7.2 km/s at 6.5 to 7 km depth (blue lines, Figure 3b). These regions correlate with a broad axis-centered plateau characterized by thickened crust (Carbotte et al., 2008; Soule et al., 2016). Average, off-axis lower crustal velocities are up to 0.2 km/s slower than the ridge flanks (orange line, Figure 3b). Mid-crustal (<4 km depth) velocities beneath the West

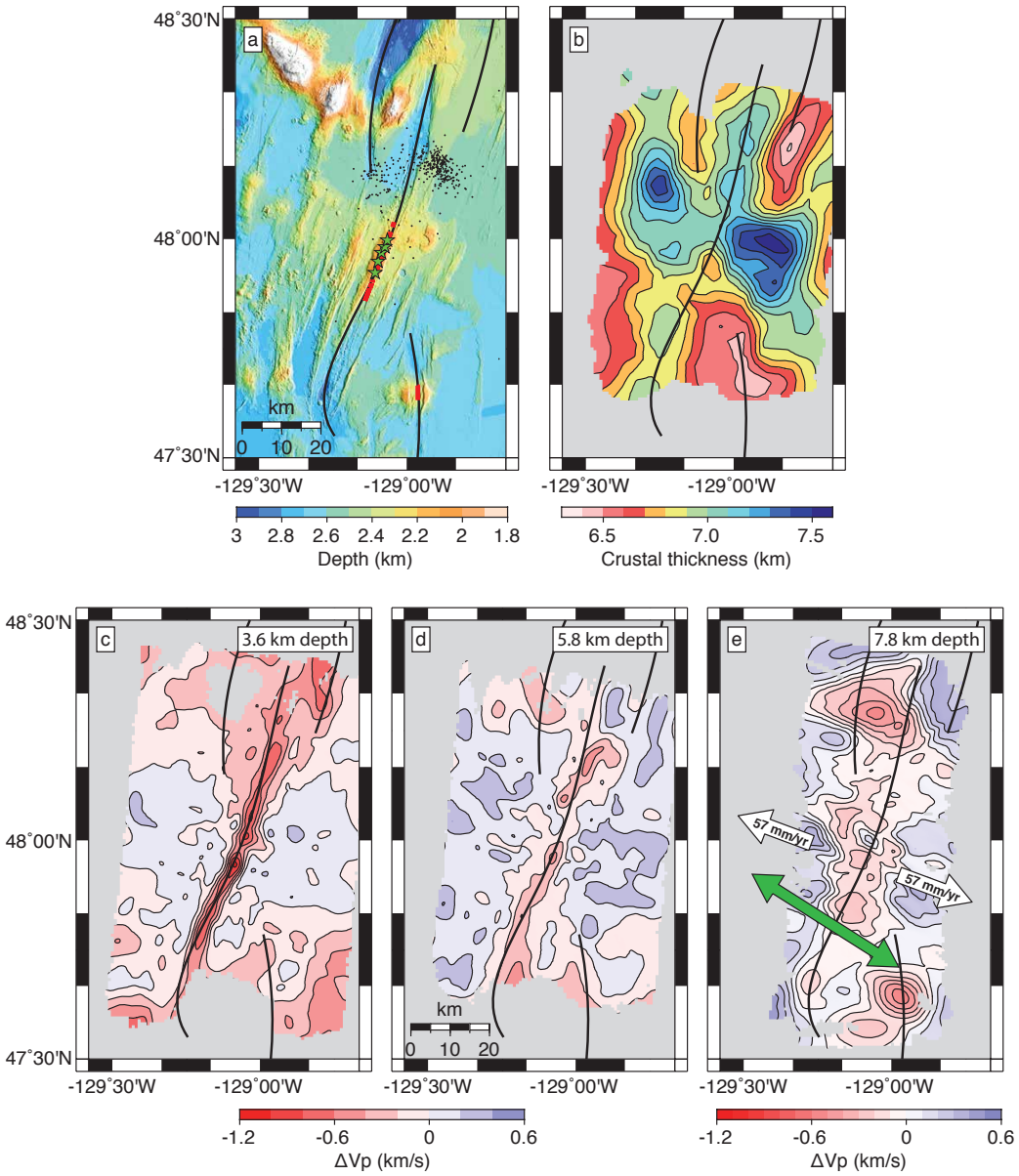

Figure 6. Comparison of bathymetry, velocity structure, and crustal thickness. (a) Bathymetry map of the Endeavour segment showing vent fields (green star), initial seismicity associated with the 2005 diking event (Hooft et al., 2010), and axial magma chamber reflector (red line segments) (Van Ark et al., 2007; Carbotte et al., 2012). (b) Mid-crustal velocity perturbations at a depth of 3.6 km. (c) Lower crustal velocity perturbations at a depth of 5.8 km. (d) Velocity perturbations within the topmost mantle. White arrows show plate spreading direction and full-spreading rate (Gripp and Gordon, 2002) and green arrows show azimuth of seismic anisotropy. Perturbations in b-d are relative to the off-axis 1-D velocity model shown in Figures 3b (orange line). (e) Segment-scale crustal thickness map. Sections show the plate boundary (bold black lines) and are masked where the DWS is less than 10 (see Appendix B).

Valley, Middle Valley, and North Symmetric propagating tips are largely slower than the average model, with Middle Valley displaying the lowest of the three (Figure 3c). Lower crustal velocities beneath these regions, however, are uniformly faster than the model average. The lowest velocities in the study area are located directly beneath the Endeavour segment (Figure 3d), with the segment center characterized by velocities of ~6.4 km/s at 4 km depth. This slow region is capped by higher mid- to upper-crustal velocities that are similar to the average model, a trend not observed elsewhere on the segment. Compared to the crustal isotropic model of Soule et al. (2016), our lower crustal velocities in the off-axis regions (Figure 3b) are up to 0.3 km/s higher owing to the inclusion of anisotropy, whereas velocities beneath the rise axis (solid red line, Figure 3d) are up to 0.3 km/s lower due to the inclusion of rise-crossing *PmP* that constrain this portion of the crust.

The segment-scale velocity structure reveals a continuous mid-crustal low-velocity volume (LVV) that tightly conforms to, and spans the entire length of, the ridge axis (Figure 4). The width of the LVV is approximately 5 km and relatively constant along-axis. Conversely, the velocity reduction of the mid-crustal anomaly varies along-axis and is greatest (ΔVp=-1.2 km/s) beneath the segment center (47°55'N to 47°58'N), correlating with the location of the hydrothermal vent fields, axial magma lens reflector (Van Ark et al., 2007; Carbotte et al., 2008), and seismicity associated with magma injection (Wilcock et al., 2009) (Figure 5). Beneath the OSCs, the mid-crustal LVV becomes more dispersed and the average velocity reduction decreases. The lowest crustal velocities in these regions, however, still conform to the ridge axis.

The along-axis continuity of the LVV diminishes with depth, such that the LVV within the lower crust is bifurcated. From approximately 5.2 km depth to the base of the crust (average depth of 6.8 km), the LVV is reduced between 48°02'N to 48°05'N (Figure

5; Y = 1 to 15 km in Figure 5a). Interestingly, this gap in the lower crustal LVV coincides with a 10-km westward offset of the MLVZ with respect to the ridge axis (Figure 5b). The southern lower crustal LVV largely tracks the ridge axis to the Cobb OSC and is largely continuous from the mantle to upper crust (Figures 5c,d). Conversely, the northern lower crustal LVV, which extends from 48°08'N to 48°13'N, is largely offset 2 km to the east of the ridge axis and coincides with the location of the inferred diking event that initiated the 2005 seismic swarm (Figure 6) (Hooft et al., 2010). Resolution tests indicate the geometry of features on the order of 6x6x2 km^3 is largely resolvable in this region of the lower crust (Appendix B, Figure S1), though the magnitude is under recovered (see Appendix B, Text S1). We note that the 2002 MCS survey did not detect an AML beneath this section of the ridge (Van Ark et al., 2007; Carbotte et al., 2008, 2012), which may be due to the eastward offset of the crustal LVV relative to the track of the MCS line.

5.3 Crustal Thickness Variations

Propagating limbs of the OSCs are characterized by the thinnest crust within the study area (Figure 6b). The Northern Symmetric, West Valley, and Middle Valley limbs have an average crustal thickness of ~6.6 km, 0.2 km thinner than the model average, with Middle Valley limb underlain by the thinnest crust (6.4 km) (Figures 3c and 6b). The thinned crust beneath North Symmetric and West Valley extend north and south of the limb tips, respectively, forming a north-south swath that projects onto the ridge axis at approximately 47°57'N, coinciding with the northern extent of the axis-centered MLVZ minima (Figure 6e). Similarly, thinned crust beneath the Middle Valley limb extends further south than the limb tip.

The Endeavour segment is characterized by along-axis variability in crustal thickness. The thinnest crust (~6.7 km) is located beneath the central portion of the segment

and is 0.2 and 0.4 km thinner than at the southern and northern ends of the segment, respectively (Figure 6b). Crustal thickness beneath the southern portion of the segment is largely uniform (~7.0 km), though it is thinner than the northern section of the segment, which is characterized by the thickest crust beneath the ridge axis (~7.2 km). The thickened crust beneath the northern section of the Endeavour ridge extends toward the segment center to approximately 48°00'N, roughly correlating with the 10-km westward cross-axis offset of the MLVZ and associated gap in the lower crustal magmatic system (Figure 6). Within this section of the segment, the crust rapidly thickens with distance from the ridge, with a more pronounced gradient to the east of the ridge axis. This thickening gives way to the thickest crust in the study area located beneath the ridge flanks.

Thickened crust is observed beneath the flanks of the segment center, coincident with the axis-centered bathymetric plateau (Figure 6b). The width and depth of the thickened crust is asymmetric about the axis, reaching a maximum thickness of 7.8 km beneath the Juan de Fuca (JdF) plate, compared to a maximum of 7.4 km beneath the Pacific plate. On the Pacific plate, the region of thickened crust is 3 km wider than that on the JdF, coinciding with a similar asymmetry in the Brunhes/Matuyama magnetic anomaly thought to be related to the recent eastward jump of the ridge ~0.1 Ma (Carbotte et al., 2008). The region of thickened crust (i.e., crustal thickness >7.1 km) beneath the Pacific plate is also more confined, extending from approximately 10-23 km off-axis, compared to the 0-20 km off-axis extent of thickened crust beneath the Juan de Fuca plate (Figure 6b). Moreover, the thickened crust beneath the Pacific plate is located further north, centered southwest of West Valley segment. This observed asymmetry in crustal thickness is roughly coincident with the increasing westward offset of the MLVZ relative to the ridge

axis to the north (Figure 6). Specifically, the MLVZ underlies the thinner crust separating the Pacific Plate crustal thickness anomaly and the ridge axis (48°01'N, -129°08'W).

6.0 Discussion

We constrain, for the first time, the three-dimensional segment-scale structure of the topmost mantle and crust beneath an active oceanic spreading center. Our results allow us to estimate the physical properties of the axial region. The observed low-velocity volume (LVV) extending from the mantle to the mid-crust cannot be entirely explained by variations in sub solidus temperature and requires the presence of partial melt. We infer that this LVV reflects the geometry of the axial magmatic system. Thus, our results provide novel insights into the magma plumbing system beneath an entire ridge segment, the influence of skewed delivery of mantle melt on along-axis variability in magmatic and hydrothermal processes, and the relationship between crustal thickness, magma supply, and the tectonic evolution of a ridge segment. We discuss each of these topics in turn.

6.1 Estimates of Physical Properties

To estimate the temperature and melt fraction variations consistent with the tomographic results, we apply the method of Dunn et al. (2000). This process involves two steps: (i) estimating the velocity reduction that can be attributed to a thermal anomaly, and (ii) interpreting the remaining velocity reduction in terms of melt fraction. The former attempts to explain the sensitivity of seismic velocity to the anharmonic and anelastic effects of temperature (Karato, 1993):

$$\frac{\partial lnVp}{\partial T} = \frac{\partial lnVp}{\partial T}\Big|_{anharmonic} - F(\alpha)\frac{Q(f,T)^{-1}}{\pi}\frac{H^*}{RT} \qquad (1)$$

where Vp is the compressional wave velocity, T is temperature, $F(\alpha)$ has a value near 1, α is the frequency dependence of Q, Q is the quality factor, f is frequency, H^* is an activation enthalpy, and R is the universal gas constant. The first term on the right-hand side of

equation (1) represents the temperature derivative due to anharmonic effects, which do not involve seismic energy loss and are independent of frequency. The second term represents the temperature derivative due to anelastic effects, which are associated with intrinsic attenuation and are frequency-dependent. The anelastic term is spatially variable owing to the spatial dependence of Q, H^*, and T. In regions where Q is large (>500), the anelastic term is negligible. Conversely, where Q is small (<100), the anelastic term is significant. We define the reference Q structure to be the average off-axis Q structure for the EPR (Wilcock et al., 1995). The axial Q structure is subsequently modified based upon the anharmonic thermal structure, discussed below. We define two values of H^* for the crust and mantle and set those values within the model to the appropriate value in Table 1. There is significant uncertainty in the values that control the anelastic term. We therefore assume the maximum possible contribution of the anelastic term by setting $F(\alpha) = 1$ and substitute the appropriate values in Table 1 into equation (1).

Table 1. Scaling relations and constants

Relation	Value	Reference
H^*_{crust}	276 kJ mol^{-1}	(Caristan, 1982)
H^*_{mantle}	500 kJ mol^{-1}	(Jackson et al., 1992)
$\left(\frac{\partial lnVp}{\partial T}\right)_{crust,\ anharmonic}$	-8.1 x 10^{-5} K^{-1}	(Christensen and Salisbury, 1979)
$\left(\frac{\partial lnVp}{\partial T}\right)_{mantle,\ anharmonic}$	-6.2 x 10^{-5} K^{-1}	(Isaak, 1992)
$\left(\frac{\partial lnVp}{\partial \phi}\right)_{gabbro,\ melt\ in\ tubules}$	-0.76	(Mavko, 1980; Canales et al., 2014)
$\left(\frac{\partial lnVp}{\partial \phi}\right)_{peridotite,\ melt\ in\ tubules}$	-0.86	(Mavko, 1980; Canales et al., 2014)
$\left(\frac{\partial lnVp}{\partial \phi}\right)_{melt\ in\ films}$	-3	(Schmeling, 1985; Dunn et al., 2000)

We derive a thermal model for the preferred velocity structure that considers both anharmonic and anelastic effects (Figure 7a). To estimate the thermal structure, the velocity

perturbation model is used to calculate temperature perturbations relative to a reference, 10-km off-axis, one-dimensional temperature profile characteristic of oceanic crust (Dunn et al., 2000) (Appendix B, Figure S3). Since subaxial temperatures are not expected to exceed 1150°C (Sinton & Detrick, 1992), we prevent perturbations that exceed this temperature so as to explain as much of the velocity reduction as possible in terms of a thermal anomaly; if we did not do so, temperatures in excess of 3000°C would be required to explain the observed velocity reduction in terms of anelastic temperature alone. We first calculate an anharmonic thermal model using only the first term of (1) (Appendix B, Figure S4a), which serves as the initial thermal structure for subsequent calculation of the anelastic thermal model and is used to modify the Q structure. Specifically, we set Q=100, the average Q value of the lower crust in the axial region of the EPR (Wilcock et al., 1995), where the anharmonic temperature estimate is above the temperature cutoff of 1150°C. To construct the anelastic thermal model, we used the appropriates values in Table 1 and the anharmonic T and Q models. Because the temperature derivative is itself

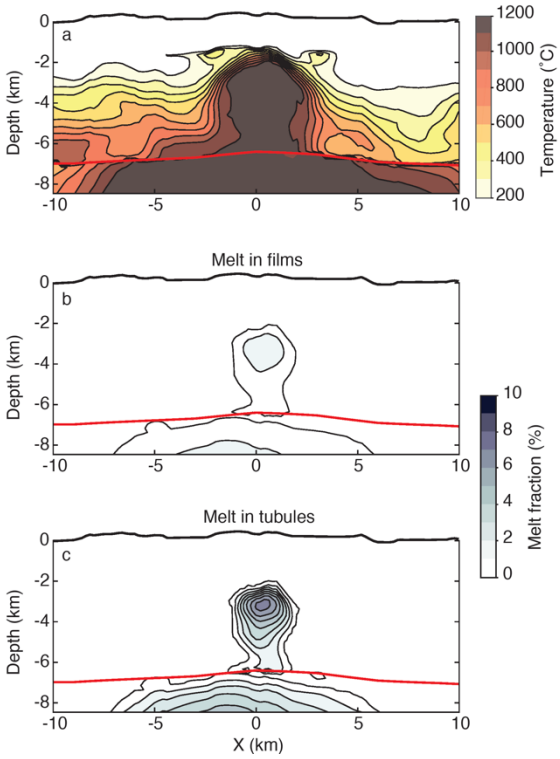

Figure 7. Temperature and melt fraction models computed from the cross-axis section in Figure 5c. Temperature and melt fraction are contoured at 100°C and 1%, respectively. (a) Temperature model assuming anharmonic and anelastic effects. (b) Melt fractions calculated assuming anharmonic plus anelastic effects for which melt resides in thin films. (c) As for (b), except for melt residing in tubules. Large velocity reductions above 2 km depth (e.g., Figure 5) are attributed to porosity variations and are therefore removed from the temperature and melt fraction calculations.

temperature dependent, we ran several iterations of equation (1) to derive the anelastic temperature. Beginning with the anharmonic thermal structure, we calculated a new temperature derivative and thermal structure for each iteration. The resultant thermal structure was then used as the new temperature model for the subsequent iteration. Iteration was ended once the maximum difference between the current and previous iteration was everywhere less than 10°C.

As at the EPR, the predicted cross-axis thermal structure beneath the Endeavour segment is steep-sided (Figures 7a and Appendix B, S4a) (Dunn et al., 2000). Moreover, our thermal model shows that anomalously high crustal temperatures are restricted to a narrow region within ~5 km of the ridge axis, similar to results from the EPR (Dunn et al., 2000). Off-axis isotherms, however, are not completely horizontal as at the EPR and instead have depressions that coincide with the edges of the MLVZ (X = -6 and 8 km, Figure 7a), a feature that is asymmetric about the rise axis. To the west of the ridge axis, the isotherms are largely horizontal, with the exception of a small depressed zone located approximately 5.5 km off-axis. A more pronounced zone of depressed isotherms is located 6 to 8 km to the east of the ridge axis. Both of these zones coincide with the location of prominent elongate abyssal hills on the seafloor, inferred to be the former ridge axis (Carbotte et al., 2008). Thus, these depressions could be indicative of enhanced hydrothermal circulation further off-axis or alternatively, the result of patterns of melt delivery, which we discuss in section 6.2.

Temperature alone cannot fully explain the magnitude of the velocity anomaly and melt must be present to explain a significant portion of the LVV. The thermal contribution to the observed velocity reduction is 46% and 57% for the anharmonic and anharmonic plus anelastic case, respectively. An estimate of the melt fraction with a LVV depends upon

the melt distribution within the rock matrix (Mavko, 1980; Schmeling, 1985). Here, we estimate melt content using the residual velocity anomalies (i.e., with thermal effects removed) for two possible cases of melt distribution: films and tubules. We use the *Vp* dependence on melt fraction for relaxed films reported by Dunn et al. (2000), using the formulation of Schmeling (1985) (Table 1). For tubules, we implement the *Vp* dependence on melt fraction for crustal and mantle rocks derived by Canales et al. (2014) using the formulation of Mavko (1980) (Table 1). These values provide lower and upper bounds for the melt fraction in regions where temperature alone cannot account for observed velocity anomalies. For the anharmonic case, we get maximum melt percentage of 3% and 12% for melt residing in films and tubules, respectively (Appendix B, Figures S4b,c). We get a maximum melt percentage of 2% and 7% for films and tubules in the case where anelasticity is important (Figures 7b,c). On the basis of these results, we infer the LVV that persists from the topmost mantle to mid-crust to be the magmatic system.

Computing temperatures and melt fractions from velocity is complicated by large sources of uncertainty. Principle among these are the (1) reference thermal structure used to compute the temperatures within the LVV, (2) *Q* structure and frequency effects, (3) geometry of the interstitial melt distribution, and (4) under-resolution of velocity anomalies. Consequently, a suite of feasible choices of parameters exist that give rise to substantially different estimates of these physical parameters. For instance, choosing a colder reference thermal structure (Appendix B, Figure S3) produces a thermal model that requires less melt and a narrower melt-containing region at mid-crustal depths (Appendix B, Figure S5). Conversely, our study underestimates the amplitude of velocity anomalies by approximately 50%, though it does provide a good indication of spatial variations in velocity and hence, relative melt content (Appendix B, Figure S1). Our analysis therefore

provides a first-order estimate of the thermal structure and melt distribution beneath the Endeavour segment.

6.2 Melt Distribution within the Mantle and Crustal Magmatic Systems

Significant variations in melt volume are observed beneath the non-overlapping portion of the Endeavour segment (Figure 8). Mantle melt volume in the non-overlapping domain is characterized by three prominent maxima (labeled I, II, and III in Figures 8c and 8d), with the two southern maxima roughly correlating with elevated crustal melt volumes and the along-axis extent of the axial magma lens (AML) (47°52'N to 48°02'N) imaged beneath the Endeavour (Van Ark et al., 2007; Carbotte et al., 2012). Crustal melt volumes within this section of ridge diminish northward, coincident with the increasing westward offset of the melt-containing region in the mantle (Figure 8). The minimum crustal melt volumes observed along the entirety of the Endeavour segment are associated with the maximum (10 km) offset of the mantle magmatic system with respect to the ridge axis (48°02'N to 48°05'N; Figure 8d); within this portion of the segment, the lower crust has little to no melt present (Figure 8b). Interestingly, the southern (48°02'N) extent of this low-melt zone is coincident with a deval (Karsten et al., 1990), or deviation from axial linearity, and the northernmost extent of the AML. Similarly, the northern (48°05'N) extent of this zone coincides with an abrupt discontinuity in tectonic fabric (Karsten et al., 1986). Another deval, located at 47°55'N (Karsten et al., 1990), correlates with the southern extent of the prominent, mid-crustal melt anomaly (Figure 8a). These results suggest a significant link between the skew of the mantle and crustal magmatic systems, the efficiency of melt transport from the mantle to the crust, and tectonic structure of the ridge.

Coincidence between along-axis variations in melt content beneath the Endeavour and seafloor features are similar to results from the EPR, suggesting that variations in

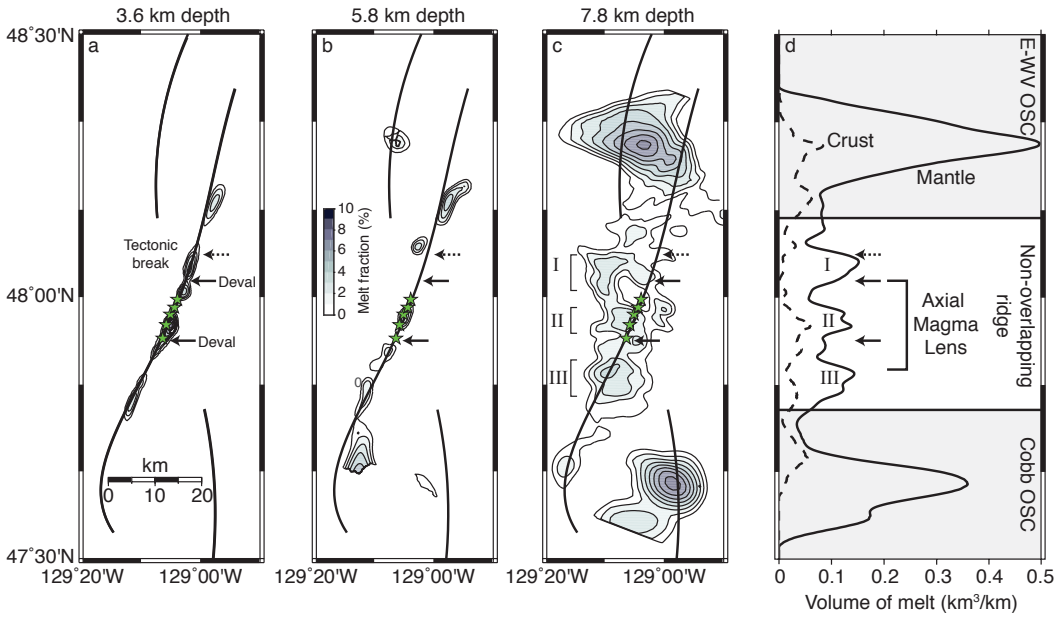

Figure 8. Along-axis variations in melt content. (a-c) Map-view sections are taken at (a) 3.6, (b) 5.8, and (c) 7.8 km depth below seafloor, corresponding to the mid-crustal, lower-crustal, and mantle portions of the magmatic system, respectively. Sections are for the model in Figure 7c. (d) Along-axis melt volume per kilometer of crust (dashed black line) and mantle (solid black line). The along-axis extent of the axial magma lens reflector is also shown (Van Ark et al., 2007). Solid black arrows denote devals (Karsten et al., 1990) and the dashed arrow indicates an abrupt discontinuity in the tectonic fabric (Karsten et al., 1986). Calculated melt fractions assume anharmonic and anelastic effects with melt residing in tubules. Regions with a DWS <10 do not contribute to the estimation, nor do regions in the model space with >4% anisotropy.

mantle melt delivery induce tectonic and magmatic segmentation. At the EPR, away from tectonic discontinuities such as transform faults or OSCs, the ridge is segmented at the scale of ~20-25 km, referred to as third-order or volcanic segments (Langmuir et al., 1986; Macdonald et al., 1988; Toomey et al., 2007; White et al., 2002). The centers of those third-order segments are associated with higher eruption effusion rates (White et al., 2002) and their boundaries coincide with discontinuities in the AML (Carbotte et al., 2013; Marjanović et al., 2014), giving rise to the notion that each third-order segment is fed by a distinct crustal magmatic system consisting of a central volcano and associated dikes and fissures (White et al., 2000, 2002). Centers of mantle melt delivery beneath the EPR are similarly spaced at intervals of ~25 km, suggesting the third-order segmentation and

associated magmatic segmentation is governed by variations in mantle melt delivery (Toomey et al., 2007). While third-order segmentation has hitherto been poorly defined at the Endeavour segment, the coincidence between the imaged LVVs with seafloor features suggest that it is segmented at a scale of ~15-20 km (Figure 8). Similar to the EPR, third-order segmentation of the Endeavour appears to be related to mantle melt delivery.

The northernmost crustal melt anomaly beneath the Endeavour segment, extending from 48°08'N to 48°13'N, is associated with a section of the ridge that overlaps the West Valley segment (Figure 8b). Here, the crustal melt anomaly is centered approximately 2 km to the east of the ridge axis and is vertically continuous from lower to mid-crustal depths. Of note is that this crustal anomaly does not directly overlie a mantle melt anomaly, though it is centered approximately 10 km south of the broad region of enhanced melt beneath the E-WV overlapping spreading center (OSC; Figures 8b,c). Resolution within this portion of the model space suggests that the northern extent of the crustal melt anomaly is not well-recovered within the lower crust (Appendix B, Figures S1b,c). We therefore postulate that this feature is associated with the E-WV mantle melt region.

The greatest volumes of mantle melt are located beneath the two second-order discontinuities bounding the segment. By volume, the Cobb and Endeavour-West Valley (E-WV) OSCs contain up to 70% and 60% more mantle melt than the non-overlapping region of the Endeavour segment, respectively (Figure 8d). This is consistent with previous results that suggest OSCs are regions of enhanced mantle melt retention (VanderBeek et al., 2016). Enhanced crustal melt retention beneath OSCs has also been inferred from seismic imaging of crustal structure along the EPR (Bazin et al., 2003) and Lau Spreading Center (Dunn et al., 2013; Turner et al., 1999), which identify anomalously broad crustal magmatic systems spanning OSCs. Moreover, multichannel seismic imaging experiments

from both the EPR (Kent et al., 2000) and Lau Basin (Collier & Sinha, 1992) reveal that widespread crustal melt lenses are characteristic of OSCs. Our crustal resolution, however, is poor beneath the OSCs such that we are unable to accurately estimate the volume of crustal melt in these regions (Appendix B, Figure S1). Yet, we do observe an increase in crustal melt content and width of the LVV as it approaches both the northern and southern limbs of the Endeavour and boundaries of our resolution, which may suggest that there is broader magmatic system and enhanced crustal melt retention beneath the OSCs (Figures 8b and 8d). No such trend is observed beneath the E-WV OSC, however, which is instead characterized by two distinct crustal melt bodies, one beneath the West Valley segment (48°18'N) and another, larger body 2 km east of the Endeavour segment (48°11'N). Thus, while our results agree with previous studies that infer second-order discontinuities are sites of enhanced mantle melt retention, they cannot confirm whether they are also sites of broad, enhanced crustal melt retention owing to limited resolution.

6.3 Skew Between the Mantle and Crustal Magmatic Systems

We infer that the observed skew between the mantle and crustal magmatic systems is a direct result of differences in mechanisms of heat transfer at crustal and mantle depths. At crustal depths we infer that hydrothermal processes extend throughout the crust and efficiently transport heat giving rise to a steep-sided, relatively narrow magmatic system confined to the axis of tectonic rifting (Figures 7a). Asymmetry in shape of thermal structure may indicate uneven rates of hydrothermal cooling, whereas depressed isotherms up to 10-km off-axis may further suggest a significant component of off-axis circulation, though this remains speculative as we are unable to discern between compositional changes and thermal variations off-axis, which could also give rise to the observed velocity variations (Figure 5c). Pervasive crustal-scale hydrothermal circulation has previously

been inferred from in situ analysis of the Oman ophiolite (e.g., Gregory & Taylor, 1981), the thermal structure of young oceanic crust (Dunn et al., 2000), and hydrothermal circulation models (Hasenclever et al., 2014). While tectonic extension along the plate boundary defines the location of magma intrusion, it is pervasive crustal-scale hydrothermal circulation that controls the depth of the melt lens (Chen & Morgan, 1996), determines the thermal structure of young oceanic crust (Hasenclever et al., 2014), and controls the cross-axis width of the crustal magmatic system (Dunn et al., 2000). On the basis of our results and those from the EPR, we conclude that when a long-lived, crustal melt lens is present at fast- or intermediate-spreading rates, the overall shape of the magmatic system is governed by a thermal structure that results from the interplay among tectonic extension, magma injection, and crustal-scale hydrothermal circulation.

Our results, together with those of VanderBeek et al. (2016), strongly suggest that at mantle depths advective heat removal is greatly diminished and conduction is the primary means of heat transport. This inference is consistent with the abrupt increase in the width of magmatic system from 5 km to 20 km width (Figure 7a). VanderBeek et al. (2016) suggest that shallow mantle melt distribution beneath mid-ocean ridges is controlled by 3-D variations in the thickness of near-ridge lithosphere. In this case, mantle melt accumulations would increase wherever the lithosphere is youngest and thinnest, owing to the topography of the thermal boundary layer (Sparks & Parmentier, 1991). Indeed, the N-S trend of the mantle magmatic system is subparallel to the thinnest crust, and by inference, the hottest and thinnest lithosphere (Figures 6b and 6e). The lack of advective heat removal at mantle depths is likely a result of permeability reduction at these depths via serpentinization of ultramafic mantle rocks and associated, large volume increases of over 50%, effectively reducing the efficiency of hydrothermal circulation across the Moho

(Wilcock & Delaney, 1996). We therefore conclude that the width and trend of the mantle magmatic system is determined by the regional-scale, mantle thermal structure of the northern Juan de Fuca Ridge, which is in turn controlled by the overlying rift geometry. Conductive heat loss is proportional to the thermal gradient and will be greater where isotherms are shaped by hydrothermal circulation at crustal depths. Thus, the mantle magmatic system is narrow beneath the segment center where hydrothermal circulation is vigorous and broad beneath the OSCs, where heat is less efficiently mined via advection.

We observe that magmatic and hydrothermal activity correlates with the cross-axis offset between accumulations of mantle melt and the much narrower crustal magmatic system. Within the central portion of the Endeavour segment, mantle melt delivery is axis-centered, coincident with the presence of an AML, enhanced crustal melt volume, and extensive hydrothermal activity consisting of >800 individual chimneys within a 15-km along-axis span (Kelley et al., 2012 and references therein) (Figures 6 and 8). This region was also a site of intense seismicity associated with magma lens replenishment (Wilcock et al., 2009). Ridge topography in the segment center, consisting of an axial high and prominent abyssal hills, indicate enhanced magmatic activity within the recent geologic past (Clague et al., 2014). In contrast, where mantle melt delivery is predominantly off-axis (to the north and south of the segment center), an AML is absent, crustal melt volumes decrease, and hydrothermal activity is diminished (Figure 8). The lowest crustal melt volumes present along the Endeavour segment are found where the MLVZ is farthest from the rise crest (48°02’N to 48°05’N, Figure 8d). These relations suggest axis-centered delivery of mantle melt exerts a primary control on magmatic and hydrothermal activity at mid-ocean ridges.

Our results, combined with those of previous studies, provide a conceptual model of how skew between mantle and crustal magmatic reservoirs governs along-axis, segment-scale variations in volcanic, magmatic, and hydrothermal activity at mid-ocean ridges (Figure 9). Beneath non-overlapping ridge segments, mantle-derived melts are focused and efficiently transported from the mantle to the crust where the magma reservoirs are vertically aligned (Figures 9a,b,d), resulting in a continuous magmatic system that extends from the topmost mantle to the mid-crust. We suggest that this efficient melt transport results in more frequent crustal magma injection events and high degrees of partial melt at crustal depths. The frequency of magma injection is thought to determine the permeability structure of the overlying crust (Wilcock et al., 2009) via seismogenic cracking of the thermal boundary layer separating the magmatic and hydrothermal systems, thereby maintaining permeable pathways and facilitating efficient hydrothermal circulation (Arnoux et al., 2017). Thus, where the cross-axis offset between the mantle and crustal magmatic systems is minimal, crustal magmatic and hydrothermal activity are enhanced. This is supported by the correlation between the vertically aligned magmatic systems in the segment center with seismicity associated with a magma injection event (Wilcock et al., 2009) and the presence of vigorous, high-temperature hydrothermal venting (Figure 5). Alternatively, where the locus of the mantle melt delivery is predominantly off-axis and the mantle and crustal magmatic systems are not vertically aligned, such as between 48°02'N and 48°05'N (Figure 8b), vertical melt transport is less efficient (Figure 9c). Owing to this inefficient melt delivery, magma injection is less frequent, resulting in the closure of permeable pathways and diminished hydrothermal venting (Figure 9c). It may be that in such sections of ridge, along-axis transport of melt within the mid-crustal reservoir plays a more prominent role in upper crustal accretion. The tectonic fabric may

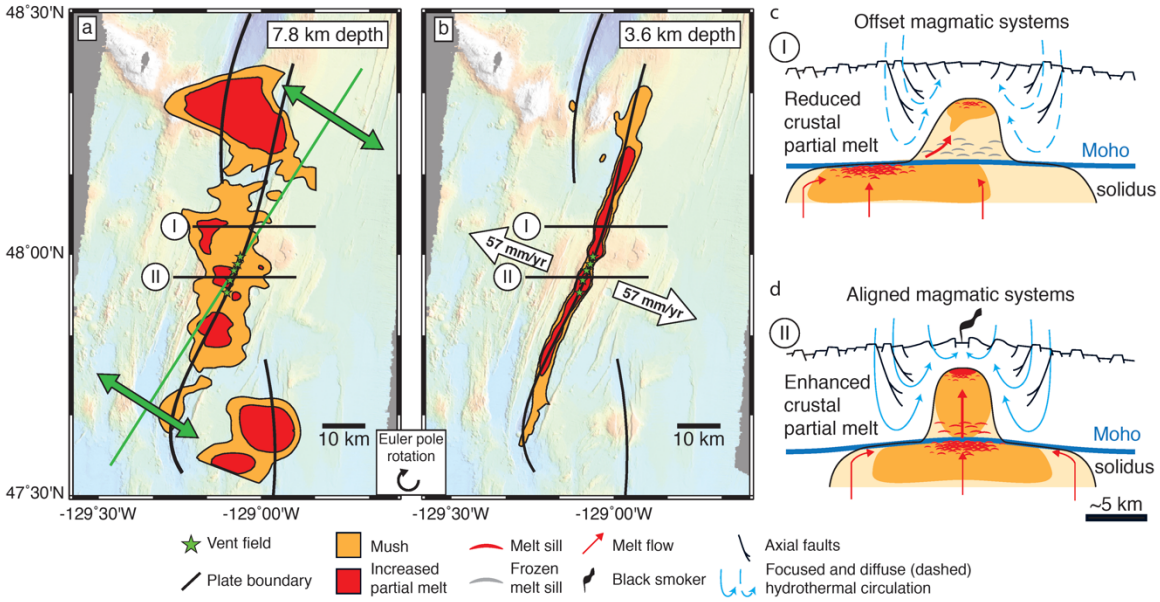

Figure 9. Conceptual diagram illustrating how skew within the magmatic system influences magmatic and hydrothermal activity. (a) Map-view section showing the north-south structure of the mantle magmatic system. The axis (green line) and direction (green arrows) of mantle divergence are overlain. Yellow and red contours in (a) demarcate regions containing low (~0%) and higher (3%) melt fractions, respectively (Figure 10c). (b) Map-view section showing the ridge-tracking structure of the crustal magmatic system. Yellow and red contours show region characterized by velocity reductions of -0.6 and -0.8 km/s, respectively (Figure 5b). Recent rotation in the Euler pole of the Juan de Fuca—Pacific plate system is indicated (Wilso*n*, 1988). (c) If the mantle and crustal magmatic systems are offset, melt transport from the mantle to the crust is inefficient, resulting in less frequent crustal replenishment. Consequently, low degrees of partial melt are present within the crust and hydrothermal clogging reduces crustal permeability, resulting in diffuse hydrothermal activity. (d) If the mantle and crustal magmatic systems are aligned, melt transport from the mantle to the crust is focused and efficient, such that enhanced partial melt is present at crustal depths. The frequent crustal replenishment induces seismogenic cracking that locally enhances crustal permeability (Wilcock et al., 2009), facilitating vigorous hydrothermal circulation.

also be influenced in cases of off-axis delivery of mantle melt, such as the abrupt discontinuity observed at 48°05'N (Figure 8) (Karsten et al., 1986).

Our model predicts that magma entering the crustal system where the two magmatic systems are vertically aligned will have undergone rapid ascent and relatively less differentiation. Extreme variability in lava enrichment is observed in the center of the Endeavour segment, coincident with axis-centered mantle melt delivery. Such a breadth of

enrichment suggests reduced magma mixing and more rapid magma ascent so as to preserve distinct mantle signatures (Karsten et al., 1990). Lower crustal velocities near the segment center are higher than elsewhere along the ridge (Figures 4 and 5c) and further support that it has undergone comparatively less differentiation (Soule et al., 2016). A progressive decrease in the level of lava enrichment northward from the segment center is consistent with mixing of magmas or sources (Karsten et al., 1990). Interestingly, this trend coincides with increasing off-axis mantle melt delivery and a decrease in lower crustal velocities flanking the magmatic system (e.g., Figure 5d), potentially indicating higher degrees of differentiation (Toomey & Hooft, 2008). In our model, the vertical alignment of the mantle and crustal magmatic systems not only controls the frequency of crustal magma injection, but also magma residence time and differentiation.

6.4 Segment-Scale Magma Transport

Along-axis crustal thickness variations do not require centralized, focused magma supply. The segmentation of mid-ocean ridges has often been attributed to magma supply (Francheteau & Ballard, 1983; Macdonald et al., 1988, 1991; Schouten et al., 1985; Whitehead et al., 1984), which predicts that the morphology of the ridge axis reflects the local supply of magma, with enhanced magma supply and hence, the thickest crust, at the center of ridge segments (Macdonald et al., 1988, 1991; Schouten et al., 1985). Conversely, segment ends are predicted to be magma-starved (i.e., reduced magma supply) and thus characterized by thinner crust and greater axial depth. We observe the opposite spatial relationship to these predictions at the Endeavour segment. Within the central portion of the segment, where the mantle and crustal magmatic systems are aligned and vigorous hydrothermal and magmatic activity persists, crustal thickness is 0.2-0.4 km thinner than the segment ends (Figure 6b). A similar association between axis-centered mantle melt

supply and thin crust has been inferred at the EPR from 9°40'N to 9°50'N (Barth & Mutter, 1996; Canales et al., 2003; Toomey et al., 2007) and analysis of flow structures in lower crustal and mantle rocks in the Oman ophiolite show that localized upwelling zones underlie the thinnest crust and crustal thickness gradually increases away from such zones (Nicolas et al., 1996). Furthermore, observations of diking events on the Endeavour provide evidence for along-axis melt transport not only from the segment center towards the segment end (Bohnenstiehl et al., 2004), but also from the segment end to the segment center (Hooft et al., 2010). Our results, in conjunction with these observations, are inconsistent with enhanced melt supply beneath the segment center that is redistributed toward segment ends. In agreement with previous studies (Barth & Mutter, 1996; Canales et al., 2003; Toomey & Hooft, 2008), we infer that the relationship between magma supply, crustal thickness, and axial depth is not as straightforward as commonly assumed.

Correlation between the diking events and intrasegment velocity structure suggests that vertical melt transport is significant and likely controls the observed along-axis crustal thickness variations. The 1999 diking event, seismic activity initiated near the central portion of the segment, roughly coincident with vertically aligned magmatic system and the location of a shallow AML (Van Ark et al., 2007; Carbotte et al., 2012), and subsequently migrated ~12 km to the south along the southern end of the Endeavour segment (Bohnenstiehl et al., 2004). Contrary to the 1999 diking event, the 2005 diking event was initiated in the northern end of the segment (48°10'N) and propagated ~20 km from segment end toward the segment center (Hooft et al., 2010; Weekly et al., 2013). The initiation of the 2005 event correlates with the eastward offset of the crustal LVV (Figures 6), though the connection of this crustal anomaly to the mantle is unclear. One possibility is that it is linked to the MLVZ beneath the E-WV OSC. Our resolution, however, is

insufficient to confirm this. Of note is the 15-km-long zone of high velocities within the lower crust separating the two sites where the diking events initiated (Figure 5a); this zone is characterized low melt content and its boundaries generally coincide with changes in seafloor fabric (Figure 8). On the basis of these observations, we suggest that melt transport within the lower crust is predominantly vertical and fundamental to the genesis of oceanic crust at the Endeavour segment.

What gives rise to the highly heterogeneous nature of crustal thickness off-axis is equivocal. For instance, asymmetric, thickened crust beneath the broad axis-centered plateau may be consistent with either enhanced magmatism in the past relative to the rest of the segment (Carbotte et al., 2008), or the southward propagation of the Endeavour segment 0.71 Ma and associated tapping of mantle melt pooled beneath the Cobb OSC (Figure 6b) (Soule et al., 2016; VanderBeek et al., 2016). Similarly, thinned crust associated with the propagating limbs in the region may be consistent with tectonically-driven ridge propagation, or indicative of crustal thinning induced by propagation itself, such as that inferred for parts of the Mid-Atlantic Ridge (Kleinrock et al., 1997). Thus, the significant heterogeneity in off-axis crustal thickness is an enigma stemming from the complex tectonic reorganization of the Endeavour segment and, consequently, difficult to explain with simple models of mid-ocean ridge segmentation.

7.0 Conclusions

1.) We image a distinct difference between the trend of the crustal and mantle low-velocity volumes (LVVs). The crustal LVV closely tracks the ridge axis, whereas the mantle LVV trends north-south, sub-parallel to the regional trend of the northern Juan de Fuca plate boundary, connecting the two overlapping spreading centers bounding the segment.

2.) We estimate, to first order, the thermal structure and melt distribution beneath the Endeavour segment. The steep-sided and narrow nature of the crustal thermal anomaly indicate pervasive crustal-scale hydrothermal circulation controls the thermal regime at crustal depths. An abrupt increase in width of the thermal anomaly across the Moho suggests that advective heat removal does not penetrate into the mantle, which is likely related to permeability reduction at these depths associated with serpentinization of ultramafic mantle rocks (William S.D. Wilcock & Delaney, 1996). We conclude that the width and trend of the mantle magmatic system is instead determined by the regional-scale, mantle thermal structure of the northern Juan de Fuca Ridge.

3.) Segment-scale skew between the mantle and crustal magmatic systems induces segment-scale variations in magmatic and hydrothermal activity at mid-ocean ridges. Previous studies have proposed a model in which sites of axis-centered melt delivery are characterized by frequent crustal magma replenishment, vigorous hydrothermal activity, and other ridge crest processes (Douglas R Toomey et al., 2007; VanderBeek et al., 2016). Conversely, sites of off-axis melt delivery are characterized by infrequent crustal magma replenishment and decreased hydrothermal activity. Ours is the first study to image the segment-scale structure of the magmatic system from the topmost mantle to upper crust and show such a link exists. The crustal magmatic system is most prominent where mantle melt delivery is axis-centered, coincident with vigorous hydrothermal venting, the along-axis extent of the imaged axial magma lens (Van Ark et al., 2007; Carbotte et al., 2012), and recent magma chamber inflation (Wilcock et al., 2009). Conversely, where mantle melt delivery is off-axis, estimated crustal melt content

is greatly reduced, hydrothermal activity is weak or absent, and an axial magma lens is nonexistent.

4.) Correlation between along-axis variations in estimated melt content and transitions in seafloor fabric suggest tectonic and magmatic segmentation on the order of ~15-20 km.

5.) Along-axis crustal thickness variations do not require centralized magma supply. The magma supply model predicts enhanced magma supply and thickened crust beneath segment centers, whereas segment ends are magma-starved and characterized by thinner crust (Macdonald et al., 1988, 1991; Schouten et al., 1985). We observe the opposite spatial relationship to these predictions, in which the segment ends are characterized by thicker (0.2-0.4 km) crust relative to the segment center. Moreover, dike propagation events along the Endeavour (Bohnenstiehl et al., 2004; Hooft et al., 2010; Weekly et al., 2013) have propagated from segment center to end, as well as segment end to center, indicating along-axis melt transport initiates from both the segment center and ends.

8.0 Bridge

Chapter III presented evidence for a segment-scale skew between the mantle and crustal magmatic systems that modulates the efficiency and frequency of mantle to crust melt transport and ridge-crest processes, including hydrothermal circulation. In sites of axis-centered mantle melt delivery, melt transport to the crust is efficient, resulting in a robust crustal magmatic system that feeds vigorous hydrothermal circulation. Previous studies have linked high-temperature hydrothermal systems to episodes of magma replenishment. However, recent observations and modeling indicate that hydrothermal heat flux is also controlled by a heterogenous crustal permeability structure. In Chapter IV, I

investigate whether the Endeavour hydrothermal system is underlain by a heterogeneous permeability structure by applying 3-D full-waveform inversion to constrain the fine-scale velocity structure (<1 km resolution) of the upper crust and use it to estimate crustal permeability. The results suggest a highly heterogeneous velocity, and by inference, permeability structure within the upper 3 km of crust that correlates with variations in seismicity, black smoker heat flux, and depth of the magma lens. I conclude that seismogenic cracking induced by magma recharge locally enhances crustal permeability and thus governs black smoker heat flux and patterns of hydrothermal circulation.

CHAPTER IV

SEISMIC EVIDENCE THAT BLACK SMOKER HEAT FLUX IS INFLUENCED BY LOCALIZED MAGMA REPLENISHMENT AND ASSOCIATED INCREASES IN CRUSTAL PERMEABILITY

From Arnoux, G. M., Toomey, D. R., Hooft, E. E. E., Wilcock, W. S., Morgan, J., Warner, M., and VanderBeek, B. P. (2017). Seismic evidence that black smoker heat flux is influenced by localized magma replenishment and associated increases in crustal permeability. *Geophysical Research Letters*, 44, 1687-1695.

1.0 Introduction

Much of what we know regarding heat flux between magmatic and hydrothermal systems at mid-ocean ridges stems from modeling. Models of hydrothermal flow, in combination with field observations, indicate sites of vigorous hydrothermal circulation overlie portions of the axial magma chamber (AMC) that have undergone recent magma replenishment (Singh et al., 1999; Humphris & Cann, 2000; Liu & Lowell, 2009; Wilcock et al., 2009); such replenishment events maintain the heat necessary to sustain the observed long-term heat fluxes of black smoker hydrothermal systems (Liu & Lowell, 2009). However, seismic observations and more recent hydrothermal modeling indicate black smoker heat flux is not only controlled by localized magma supply rates, but also by a heterogeneous crustal permeability structure (Wilcock et al., 2009; Lowell et al., 2013; Singh et al., 2013). Realistic estimates of crustal permeability beneath black smoker vent fields are thus necessary to better understand these systems (Lowell et al., 2013). Three-dimensional full-waveform inversion (FWI) (Warner et al., 2013), an advanced seismic imaging technique commonly applied to industry data sets, has the resolution necessary to

constrain fine-scale velocity structure that can be used to infer relative spatial variations in crustal permeability (Carlson, 2011).

Here we apply three-dimensional FWI to seismic data collected on the Endeavour segment of the Juan de Fuca Ridge to develop high-resolution images of the magmatic-hydrothermal reaction zone—the region near the magmatic heat source in which high-temperature, water-rock reactions occur—beneath several well-studied hydrothermal vent fields. The central rift valley of the Endeavour segment hosts five long-lived black smoker vent fields (from north to south – Sasquatch, Salty Dawg, High Rise, Main Endeavour, and Mothra) driven by heat loss from an AMC located approximately 2.2-3.3 km below the seafloor (Van Ark et al., 2007; Carbotte et al., 2008, 2012) (Figure 1). These vent fields are characterized by large variations in heat flux (Thompson et al., 2005; Kellogg, 2011), steep gradients in temperature and chemistry (Butterfield et al., 1994; Kelley et al., 2002, 2012), and high levels of associated seismicity (Wilcock et al., 2009; Kelley et al., 2012). We resolve fine-scale velocity variations within the magmatic-hydrothermal reaction zone that correlate with concentrations of seismicity, the heat fluxes of the overlying hydrothermal vent fields, and variations in the axial magmatic system. In conjunction with previous microseismicity and hydrothermal studies, we conclude that black smoker heat flux is influenced by localized magma replenishment to the AMC, which induces seismogenic cracking and increases crustal permeability within the overlying reaction zone. The interplay between these linked processes and the clogging of permeability by hydrothermal deposits gives rise to an evolving, strongly heterogeneous permeability structure within the magmatic-hydrothermal reaction zone along the segment.

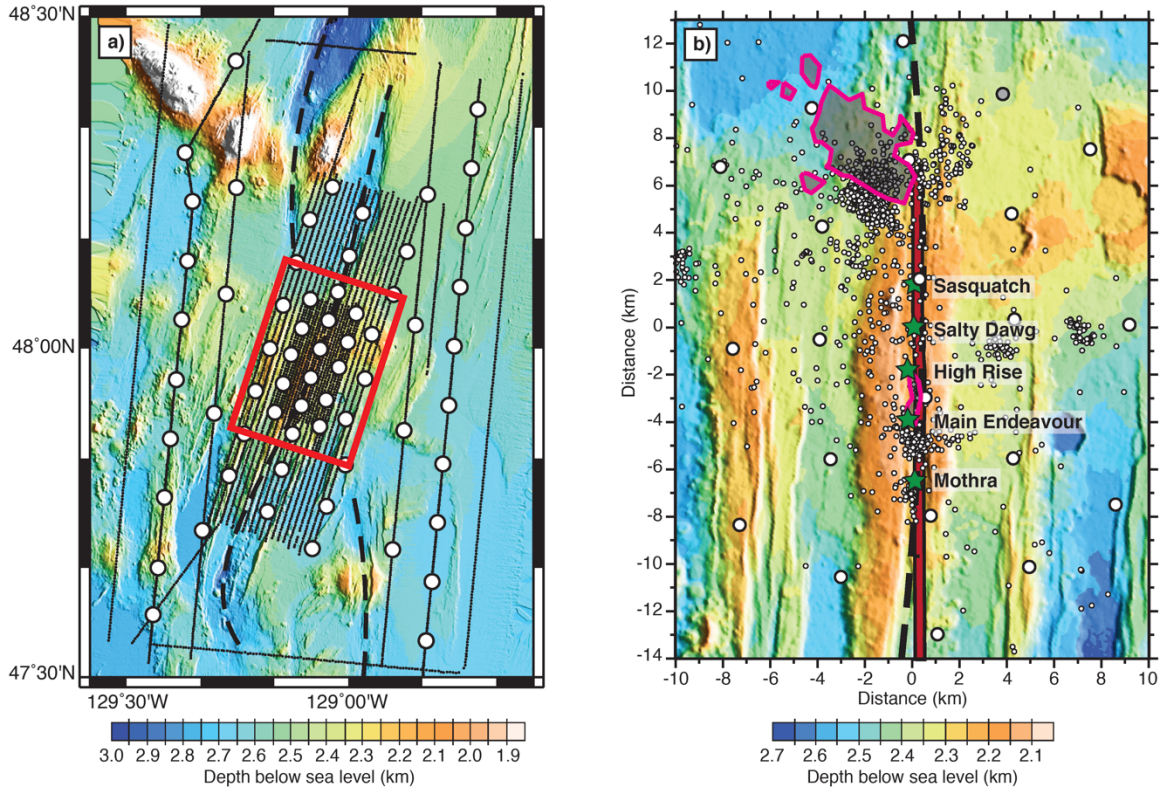

Figure 1. The Endeavour seismic tomography experiment. (a) Configuration of the ETOMO experiment conducted along the Endeavour segment of the Juan de Fuca Ridge. Seismic data were collected using four-component ocean bottom seismometers (OBSs; large white circles) and the 6600 cu. in. airgun array of the *R/V Marcus G. Langseth*. Black dots show shot locations and thick dashed lines indicate the plate boundary. Data from the crustal grid (red box) were used in FWI. (b) Crustal grid of the ETOMO experiment consisting of 22 OBSs (large white circles) that recorded 1673 airgun shots; one OBS did not record data (grey circle). Vent fields (green stars) and AMC reflector (red line) (Van Ark et al., 2007) are overlain. Magenta contours show areas with earthquake densities >20 events per km^2 recorded during the February 2005 swarm (Hooft et al., 2010). Small white circles are epicenters of post-swarm earthquakes that occurred between October 2005 and June 2006 (Weekly et al., 2013).

2.0 Experiment and Methods

2.1 Endeavour Tomography Experiment

The Endeavour tomography (ETOMO) experiment was conducted in 2009 on the Endeavour segment and used a seismic array consisting of 68 four-component (three orthogonal geophones and one hydrophone) ocean bottom seismometers (OBSs) to record ~5500 airgun shots from the 36-element, 6600 cu. in airgun array of the *R/V Marcus G.*

Langseth (Weekly et al., 2014) (Figure 1a). The central portion of the experiment, or the crustal grid, encompassed the five hydrothermal vent fields and recorded seismic data for imaging the detailed structure of the upper crust underlying the hydrothermal vent fields (Figure 1b and red box in Figure 1a). The crustal grid includes 22 OBSs with an average spacing of 5 km that recorded 1673 airgun shots, with spacing of ~450 m along and 450 m to 1 km between each shot line, representing the densest portion of the ETOMO experiment; one OBS within the crustal grid did not record data (grey circle in Figure 1b). We use data from a subset of the crustal grid that consist of a total of ~24,500 seismograms recorded on the hydrophones of 21 OBSs (Figure 1). Examples of the seismic data are provided in Figure S1 in Appendix C.

2.2 Three-Dimensional Full-Waveform Inversion

A previous travel-time tomography study provides a three-dimensional starting model of upper crustal *P*-wave velocity and anisotropy (Weekly et al., 2014) (Appendix C, Figures S2a and S3a-d). For the purpose of this study, the initial velocity model was constructed such that it incorporated only the crustal grid portion of the ETOMO experiment. FWI requires ~4 grid points per wavelength for the maximum frequency and the minimum velocity which is approximately 1500 ms^{-1} within the water column (Morgan et al., 2016). Thus, a grid spacing of 50 m was chosen so that our inversions could reach a maximum frequency of 6.5 Hz. The velocity model is 20 km x 27 km wide and 8.95 km deep, corresponding to a grid of 401 x 541 x 180 nodes. Reciprocity was applied to reduce the computation cost of the inversions.

The starting velocity model was smoothed relative to the travel-time tomography model (Weekly et al., 2014), as it is preferable to start FWI with a smooth model (Morgan et al., 2016). Smoothing was applied horizontally and vertically over a distance of about

half the seismic wavelength at the lowest inversion frequency, 3 Hz, to remove structure below the theoretical resolution of FWI. This effectively smoothed layer 2A, which was included in the travel-time tomography model based on thickness estimates from MCS data (Carbotte et al., 2008). The data were windowed around the first arriving crustal refractions (Pg) using a window length of 750 ms. While S-waves were infrequently present within this window, as seen on the radial channel, their energy did not contribute to that on the hydrophone (Appendix C, Figure S4).

Data at larger offsets from the OBSs within the crustal grid were dominated by noise (Appendix C, Figures S5a and S6). The adverse effects of noise are frequency dependent, such that data up to 10 km and 15 km offsets were useable in the inversions at low (3-4 Hz) and high (4-6 Hz) frequencies, respectively (Appendix C, Figure S6a and b). Furthermore, at offsets closer than approximately 2.9 km, the first arrival is obscured by its interactions with the large amplitude direct arrivals through the water column. Therefore, data between offsets of 2.9–10 km were inverted with 10 iterations at low-pass cutoff frequencies of 3.0, 3.4, and 3.9 Hz. Data at offsets between 2.9–15 km were then input into the inversion and 5 iterations performed at 3.3 and 3.8 Hz, followed by 10 iterations performed at 4.4 and 5.1 Hz. During FWI, velocity is iteratively updated whereas anisotropy is held constant (Morgan et al., 2016); examples of Vp model updates during the inversion are shown in Figure S7 in Appendix C. A more detailed description of the methods is provided in Morgan et al. (2016).

3.0 Results

Figures S2 and S3 in Appendix C show comparisons between the travel-time tomography and FWI results. While generally consistent with results from travel-time tomography (Weekly et al., 2014), our FWI images depict larger amplitude anomalies and

provide improved spatial resolution of the crust above the axial magmatic system and beneath the active vent fields (Figures 2 and 3). Synthetic resolution tests indicate the ability to resolve structure on the order of 0.8-1 km^3 within the upper 3 km of crust, representing a fourfold improvement over the travel-time tomography results (Weekly et al., 2014) (Appendix C, Figures S8 and S9). Resolution decreases with depth, however, such that structures on the order of 1.5 km^3 are better constrained down to 2.5 km bsf, but are unrecoverable below 3 km. We therefore avoid structural interpretations below 3 km bsf (Appendix C). Additional information pertaining to model resolution and fitness is provided in Appendix C (Thurber, 1983; Toomey & Foulger, 1989; Toomey et al., 1994).

3.1 Along-Axis Structure

Significant heterogeneity in the velocity structure is observed along-axis (Figures 2a and Appendix C, S10). A large low-velocity anomaly is detected 2.5 km bsf, the top of which correlates well with the depth of the AMC reflector (Van Ark et al., 2007; Carbotte et al., 2008) (Figure 2a); the magnitude of this anomaly is greatest between the Main Endeavour and High Rise vent fields and decreases to the north and south. Directly overlying the AMC reflector, within the inferred location of the magmatic-hydrothermal reaction zone, low-velocity anomalies are resolved beneath Main Endeavour and High Rise, whereas the other vent fields are underlain by higher velocities (Figure 2a); we note, however, that the reaction zone above the AMC is likely much thinner than is resolved by FWI. There is a correlation between the velocity, density of earthquakes, and intensity of hydrothermal venting. The region of the most concentrated seismicity coincides with the low velocities that are located beneath the High Rise and Main Endeavour vent fields, which in comparison to the other vent fields on the Endeavour segment are characterized

by a larger number of black smoker vents (Kelley et al., 2002), higher maximum venting temperatures (Kelley et al., 2002), and higher heat fluxes (Kellogg, 2011) (Figure 2).

A prominent low-velocity anomaly lies 5 km to the north of the Sasquatch vent field, centered at 2 km bsf in a region of enhanced seismicity (Figures 2 and Appendix C, S11). No reflector corresponding to this low-velocity anomaly was detected in a 2002 MCS study (Van Ark et al., 2007; Carbotte et al., 2008, 2012). Low-velocity anomalies also underlie Mothra at 1-2 km bsf and extend to the south of the vent fields.

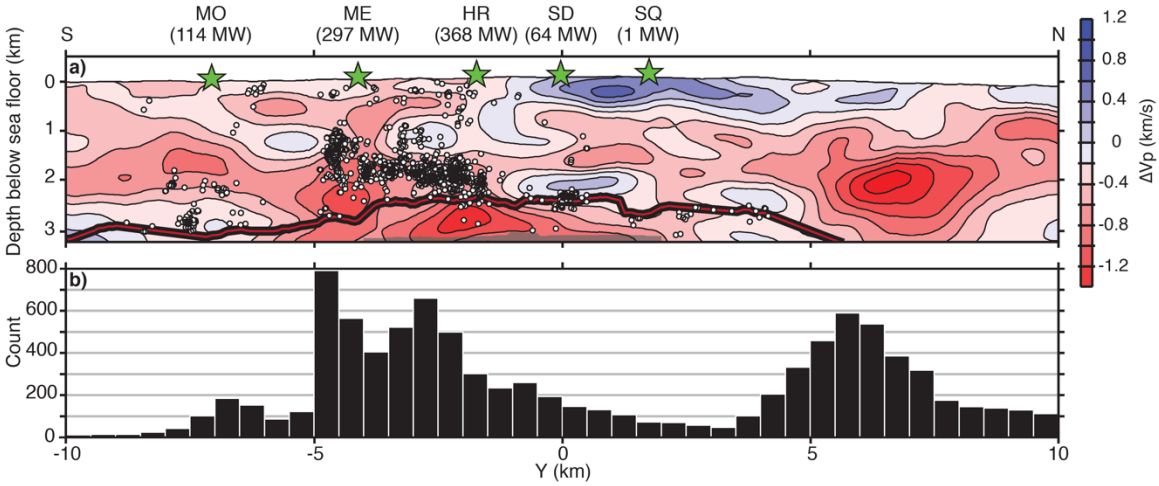

Figure 2. Along-axis section of preferred model and microseismicity. (a) Along-axis section (X = 0.1 km, see Figure 1b) of the preferred FWI model. Three-dimensional velocity anomalies are plotted relative to a horizontal average of the starting model and masked in regions where the derivative weight sum is less than 10 (see Appendix C). Section shows the locations of the vent fields (green stars), hypocenters for earthquakes recorded between 2003 and 2004 (white circles) (Wilcock et al., 2009), and AMC reflector (bold red and black line) (Van Ark et al., 2007). The position of the AMC was obtained by converting two-way travel-times of the AMC (Van Ark et al., 2007) to depth assuming a horizontal average of the velocity model from travel-time tomography. The heat fluxes of the five vent fields are provided above each vent (Kellogg, 2011); MO = Mothra, ME = Main Endeavour, HR = High Rise, SD = Salty Dawg, and SQ = Sasquatch. (b) Histogram of ~6000 earthquakes that occurred within 2 km of the ridge axis, located via an automated method from 2003 to 2006 (Weekly et al., 2013). Earthquakes are binned in 0.5 km intervals along the ridge axis. Hypocenters from this data set are not shown in (a) because of poor depth constraints since many of these earthquakes occurred outside of the seismic network. Modified from Figure 12c in Weekly et al. (2014).

3.2 Across-Axis Structure

FWI results for rise-perpendicular sections located across four of the hydrothermal vent fields—Mothra, Main Endeavour, High Rise, and Salty Dawg—are shown in Figure 3. At 2-3 km bsf, a pronounced low-velocity zone that correlates with the AMC reflector underlies all of the vent fields aside from Mothra, the southernmost field. We note that the width of the mid-crustal low-velocity anomaly, at 3 km bsf in Figures 3b-d, varies between 1-2 km in width and is thus greater than the width of the overlying AMC reflector (0.4–1.2 km) (Van Ark et al., 2007; Carbotte et al., 2008, 2012). Resolution tests indicate that at these depths we can resolve features approximately 1-1.5 km in width (Appendix C), suggesting that a broader low velocity zone likely underlies the AMC reflector.

Significant low-velocity anomalies are imaged that underlie the abyssal hills within ±2 km of the ridge axis (Figures 3 and Appendix C, S11), correlating with the approximately 2-km-wide region in which <10,700 year old dikes are located (Clague et al., 2014). Further off-axis, these low-velocity anomalies give way to high velocities, forming a sequence of alternating low- and high-velocity anomalies that parallel the ridge axis (Figures 3 and Appendix C, S11). The bands have an average width of 2-3 km and span the length of the entire segment within our study area. The widest and largest magnitude high-velocity band is located beneath, and to the east of, the westernmost abyssal hill (Appendix C, Figures S11a and b).

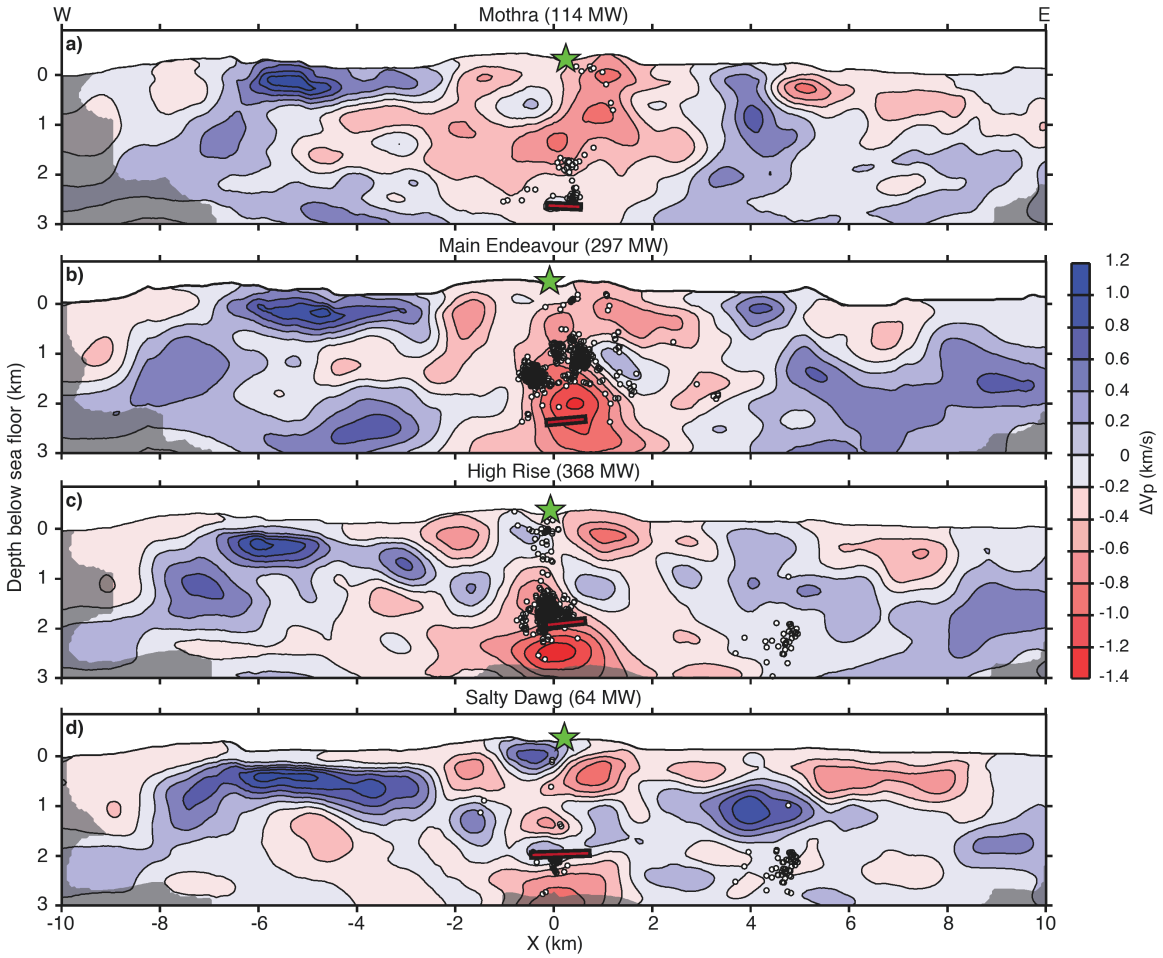

Figure 3. Across-axis sections showing velocity anomalies beneath hydrothermal vent fields. Vertical sections crossing the ridge axis at (a) Mothra (Y = -7 km), (b) Main Endeavour (Y = -4.1 km), (c) High Rise (Y = -1.7 km), and (d) Salty Dawg (Y = 0 km), masked in regions where the derivative weight sum is less than 10 (see Appendix C). Overlain are the hypocenters for earthquakes recorded between 2003 and 2004 (white circles) (Wilcock et al., 2009), vent field locations (green stars), and the AMC reflector (red and black line) (Van Ark et al., 2007). Heat fluxes are provided above each vent (Kellogg, 2011).

4.0 Discussion

Above the AMC reflector, we attribute the observed variations in the velocity structure (Figures 2a and 3) primarily to fluctuations in porosity and by inference, permeability (Appendix C, Figures S12 and S13). In the upper to middle crust, variations in *Vp* provide a reliable estimate of crustal porosity (Swift et al., 2008; Carlson, 2010; Carlson, 2014). We note that sub-solidus variations in temperature also affect seismic

properties. However, since compressional wave speeds show only a slight linear decrease with increasing temperatures below roughly 600˚C (Christensen, 1996; Kern et al., 2001), large lateral variations in *Vp* above the AMC and within the upper 3 km of oceanic crust are most likely due to localized changes in porosity; in Appendix C, we describe a method to convert absolute velocity to porosity and provide images of the converted velocity structure (Appendix C, Equation S1; Table S1; Figures S12 and S13). While porosity is not equivalent to crustal scale hydrologic permeability, it is the primary variable that affects permeability (Bernabé et al., 2003) and may therefore be linked to variations in permeability in the upper to middle oceanic crust (Carlson, 2011). Yet, as there is no simple way to relate porosity and permeability, we relate *Vp* and porosity to permeability qualitatively.

The low-velocities beneath the near-axis abyssal hills are consistent with enhanced porosity along a complex of inward- and outward-facing normal faults (Figures 3 and 4b). In this model, the complex of outward-facing faults are draped by syntectonic lava flows and termed “volcanic-growth faults” (Macdonald et al., 1996). Crustal damage caused by dike propagation from the AMC to the seafloor may also contribute to the low seismic velocities found beneath the abyssal hills and those forming the v-shaped low-velocity pattern at depth (Delaney et al., 1984; Fontaine et al., 2014). This interpretation offers an explanation for the occurrence of anomalously young lavas sampled off-axis (Clague et al., 2014). The alternating sequence of low- and high-velocity anomalies further off-axis appears to be associated with bathymetric highs and lows, with lower velocities centered beneath the outer flanks of the outer abyssal hills. We therefore infer that this banding indicates variations in the thickness of layer 2A, in concert with previous results (Barclay & Wilcock, 2004; Van Ark et al., 2007; Weekly et al., 2014). Furthermore, we attribute the

shallow (1-2 km bsf) low-velocity anomalies beneath and to the south of Mothra and the large low-velocity anomaly north of Sasquatch to fracturing resulting from dike propagation and tectonic fracturing associated with the 6-year non-erupting spreading event that occurred from 1999-2005 along the Endeavour segment (Bohnenstiehl et al., 2004; Hooft et al., 2010; Weekly et al., 2013) (Figures 2a and 4a).

Beneath the AMC reflector (Van Ark et al., 2007; Carbotte et al., 2008, 2012), we attribute variations in the magnitude of the mid-crustal low-velocity zone to lateral variations in melt content of the axial magmatic system (Figure 4a). Owing to the limited mid-crustal data incorporated in the current analysis, the true magnitude of the low-velocity anomaly is underestimated, thus we cannot place absolute bounds on the melt fraction. However, the observed variation in the magnitude of the velocity anomaly along axis is a resolvable feature (Appendix C), which allows us to infer that melt fractions in the magmatic system beneath the AMC reflector must vary. Notably, the region of lowest velocities beneath the AMC reflector—and by inference highest melt fractions—coincides with the concentration of seismicity in 2003-2004 between the Main Endeavour (MEF) and High Rise (HR) vent fields, which are characterized by a larger number of black smoker vents (Kelley et al., 2002), higher maximum venting temperatures (Kelley et al., 2002), and higher heat fluxes (Kellogg, 2011) than the other vent fields on the Endeavour segment (Figure 2a). Focal mechanisms for these earthquakes are also consistent with stress perturbations resulting from injection of magma into a sill (Wilcock et al., 2009). We therefore infer that the observed variation in the low-velocity anomaly beneath the AMC reflector is the result of a more recent magma recharge event between MEF and HR (Figures 2a and 4).

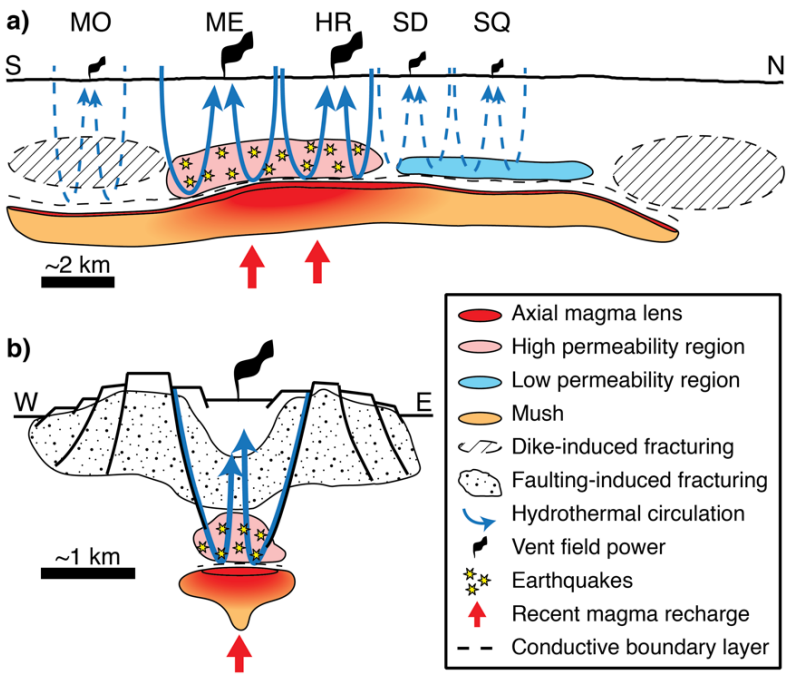

Figure 4. Conceptual illustration for processes that modify crustal permeability. (a) Along-axis section depicting the relations between active processes and vent field power output (stylized black swaths). Recent recharge (red arrows) to the AMC (red lens) induces seismogenic cracking (yellow stars) that enhances crustal permeability (pink region), resulting in a thin conductive boundary layer (dashed line; CBL) and efficient hydrothermal circulation (solid blue arrows). Lack of recent magma replenishment results in a reduction of permeability via hydrothermal clogging within the reaction zone (light blue region) and a thicker CBL, resulting in inefficient hydrothermal circulation (dashed blue arrows) that cannot reach the CBL. Regions of dike-induced fracturing are shown by ellipses with diagonal lines. (b) Rise-perpendicular section showing processes beneath the High Rise vent field. Inward-dipping normal faults near the axial valley serve as pathways for hydrothermal fluids, and along with outward-facing faults on the abyssal hills, fracture the crust, generating zones of enhanced permeability (stippled regions). Efficient hydrothermal circulation is facilitated by enhanced permeability above the AMC, resulting from seismicity associated with recent magma chamber recharge; this also results in a thin CBL above the AMC. Gradient in mush zone indicates higher melt fractions in red regions.

On the basis of the coincident variations in the magmatic system, rates of seismicity, and power output of the overlying vent fields, we infer magma recharge

associated with seismogenic cracking and increased permeability exerts a primary control on black smoker heat flux. Black smokers are driven by heat transferred from an axial magma reservoir via a thin (10-100 m) thermal boundary layer (TBL) at the interface between hydrothermal circulation cells and the roof of the magma chamber (Lowell & Germanovich, 2004; Liu &Lowell, 2009). In the absence of magma replenishment, the TBL thickens owing to hydrothermal clogging (Wilcock & Delaney, 1996) and crystallization of magma to the roof of the reservoir (Singh et al., 1999; Lowell & Germanovich, 2004; Liu & Lowell, 2009). We infer that the former process is apparent in the relatively high velocities and low rates of seismicity that characterize the reaction zone beneath Mothra, Salty Dawg, and Sasquatch, the vent fields with the lowest heat fluxes on the Endeavour segment (Figures 2a, 3a, d, and 4a). Recent magma injection, on the other hand, induces seismogenic cracking that counteracts the thickening of the TBL by increasing crustal permeability within the reaction zone (Wilcock et al., 2009), a scenario evident beneath MEF and HR, the most robust vent fields on the segment (Figures 2a, 3b, c, 4a, and b); magma replenishment may also thin the TBL by limiting crystallization on the roof of the reservoir. The absolute timescales for these interconnected effects are unconstrained, though modeling indicates that magmatic perturbations to the AMC may take from months to years to influence heat flux at the surface (Germanovich et al., 2011); a decrease in magma resupply would take a similar amount of time to result in a decline in seafloor vent temperatures and heat output (Singh et al., 2013; Choi & Lowell, 2015). In conjunction with previous microseismicity and hydrothermal studies, we conclude the large variations in heat flux that characterize the Endeavour hydrothermal system are a manifestation of localized magma injection that produces an evolving and strongly heterogeneous crustal permeability structure via induced seismogenic cracking.

5.0 Conclusions

Previous work has demonstrated the necessity for magma replenishment in maintaining the longevity and high heat fluxes of black smoker hydrothermal systems (Humphris & Cann, 2000; Lowell & Germanovich, 2004; Liu & Lowell, 2009). While it has been proposed that magma recharge events modify crustal permeability (Wilcock et al., 2009; Lowell et al., 2013), geophysical observations to support this hypothesis have been lacking. Our results imply that magma recharge and induced seismogenic cracking contribute to enhanced crustal permeability and that spatial and temporal variations in this process give rise to an evolving, highly heterogeneous crustal permeability that governs, in part, the heat flux of black smoker hydrothermal systems and the pattern of hydrothermal circulation. Cracking induced by dike propagation and tectonic faulting may also modify crustal permeability, providing additional controls on hydrothermal circulation. Thus, our results support inferences made from modeling studies and provide constraints on spatial variations in the permeability structure of the crust that can be incorporated into models of hydrothermal flow to further our understanding of magma-driven hydrothermal systems.

CHAPTER V

CONCLUSION

This dissertation explored mass and energy exchange at mid-ocean ridges. Active-source seismic data collected at the East Pacific Rise (EPR) and Endeavour segment of the Juan de Fuca Ridge (JdFR) allowed me to construct the first images of the segment-scale structure of a mid-ocean ridge magmatic system in its entirety, from the topmost mantle to upper crust, and place novel constraints on the physical properties of a ridge segment. These results provide new insights into the mechanics of magmatic focusing, origin of mid-ocean ridge segmentation, and link between tectonic, magmatic, and hydrothermal processes. At the EPR, subcrustal reflections were found to originate from dunitic interfaces located between 2 and 6 km beneath the crust. The general along-axis depth variations of these dunitic horizons correlate with patterns of mantle upwelling along the northern EPR, suggesting these features may be thermally controlled. Observations of dunitic horizons within the mantle sections of ophiolites are common and thought to be related to focused porous flow, a notion supported by geodynamic modeling. These observations suggest that the dunitic horizons may be related to focused melt flow, thereby supporting previous models of high-porosity channels at the base of the thermal lithosphere as a mechanism for magmatic focusing beneath mid-ocean ridges. Beneath the Endeavour segment of the JdFR, the mantle magmatic system was found to be skewed relative to the ridge-tracking crustal magmatic system. Along-axis variations in mantle and crustal melt volume coincided with the vertical alignment of the magmatic systems, intensity of hydrothermal activity, inferred crustal composition, and abrupt changes in seafloor fabric. These correlations indicate that the relative skew between the mantle and crustal magmatic

systems exerts a primary control on magmatic and ridge-crest processes and thus, mass and energy transfer, at mid-ocean ridges. High resolution seismic velocity images of the upper 3 km of crust beneath the Endeavour segment demonstrate that hydrothermal heat flux is not only controlled by magma replenishment, but also associated changes in crustal permeability. Along-axis velocity variations beneath the Endeavour hydrothermal system indicate highly heterogeneous crustal permeability above the axial magma lens, with high permeability zones coinciding with enhanced seismicity induced by magma injection and high fluxes in the overlying hydrothermal vent fields. In contrast, low seismicity rates and low heat fluxes accompany low permeability zones. Thus, these results demonstrate that magma lens replenishment and induced seismogenic cracking enhance crustal permeability, providing an important mechanism for maintaining permeable pathways for hydrothermal fluids to interact with the axial magma lens.

The results from this dissertation provide novel insights into how mass and energy are transferred between the solid Earth and its hydrosphere. Yet, there exist a plethora of outstanding questions. Does the mush zone of mid-ocean ridge magmatic systems consist of discrete magma bodies or is it a diffuse zone of low partial melt? What controls the characteristics and distribution of crustal magma bodies off-axis? Are off-axis magmatic systems long-lived due to less intense faulting and fissures and thus, less efficient hydrothermal cooling? To address these questions, future work is directed at utilizing higher resolution imaging to constrain the detailed structure of oceanic spreading centers.

APPENDIX A

CHAPTER II SUPPORTING INFORMATION

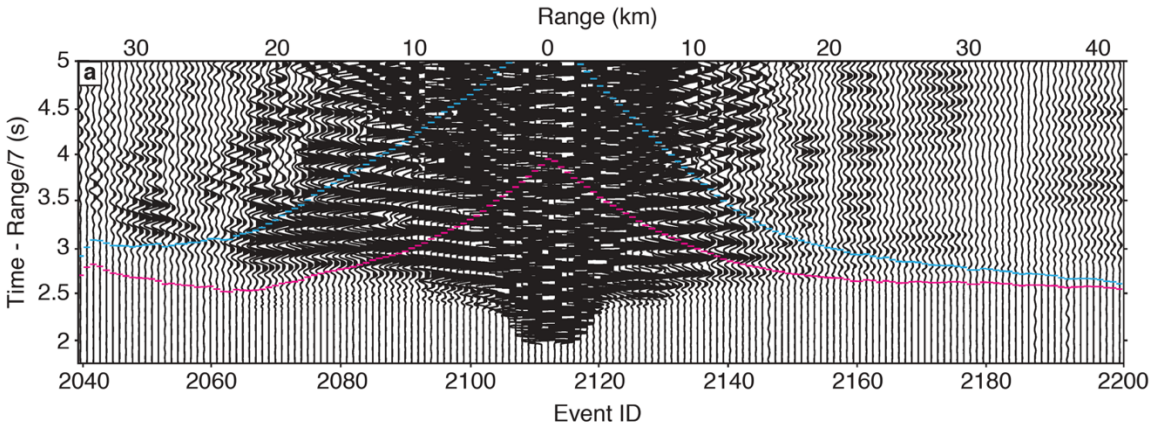

Figure S1. Same as in Figure 2, except record section is for the radial component of OBS 64. Note the absence of *S*-wave energy.

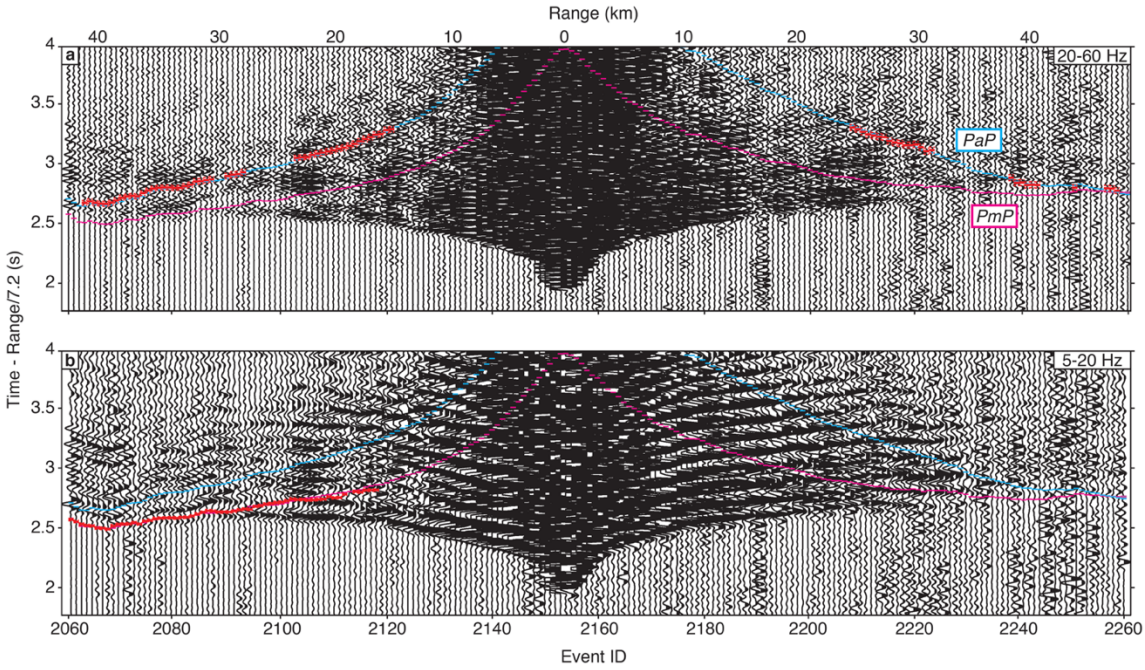

Figure S2. As in Figure 2, showing picked (a) *PaP* and (b) *PmP* arrivals (red ticks) for ocean bottom hydrophone 25.

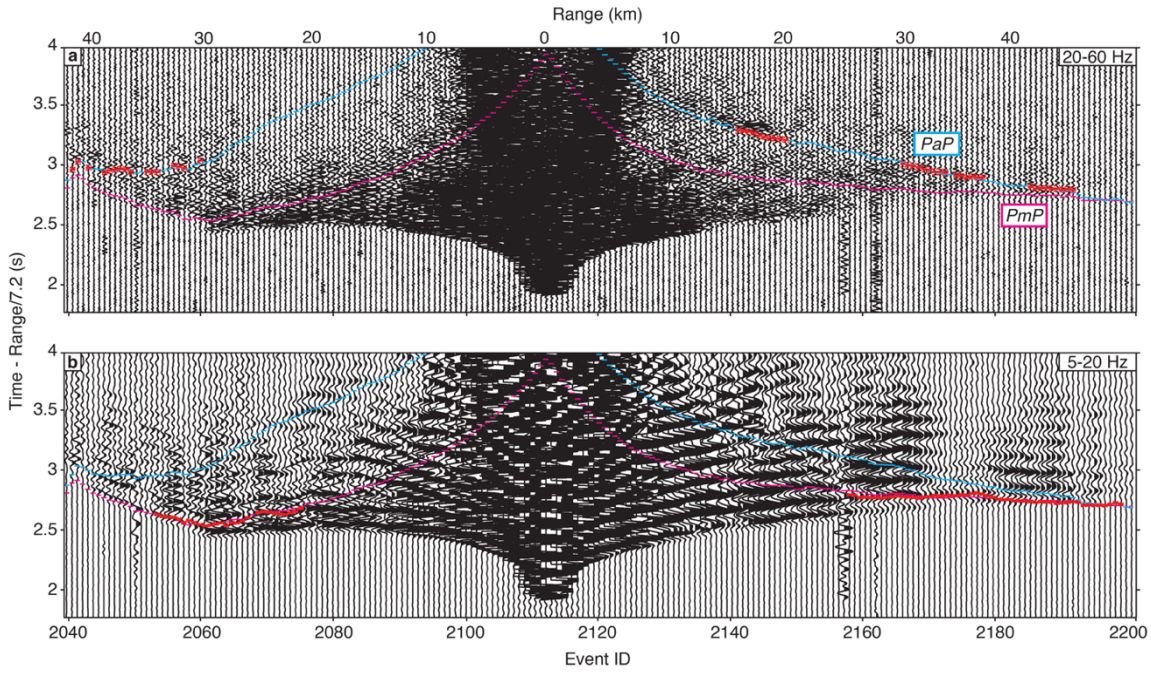

Figure S3. As in Figure 2, showing picked (a) *PaP* and (b) *PmP* arrivals (red ticks) for ocean bottom seismometer 54.

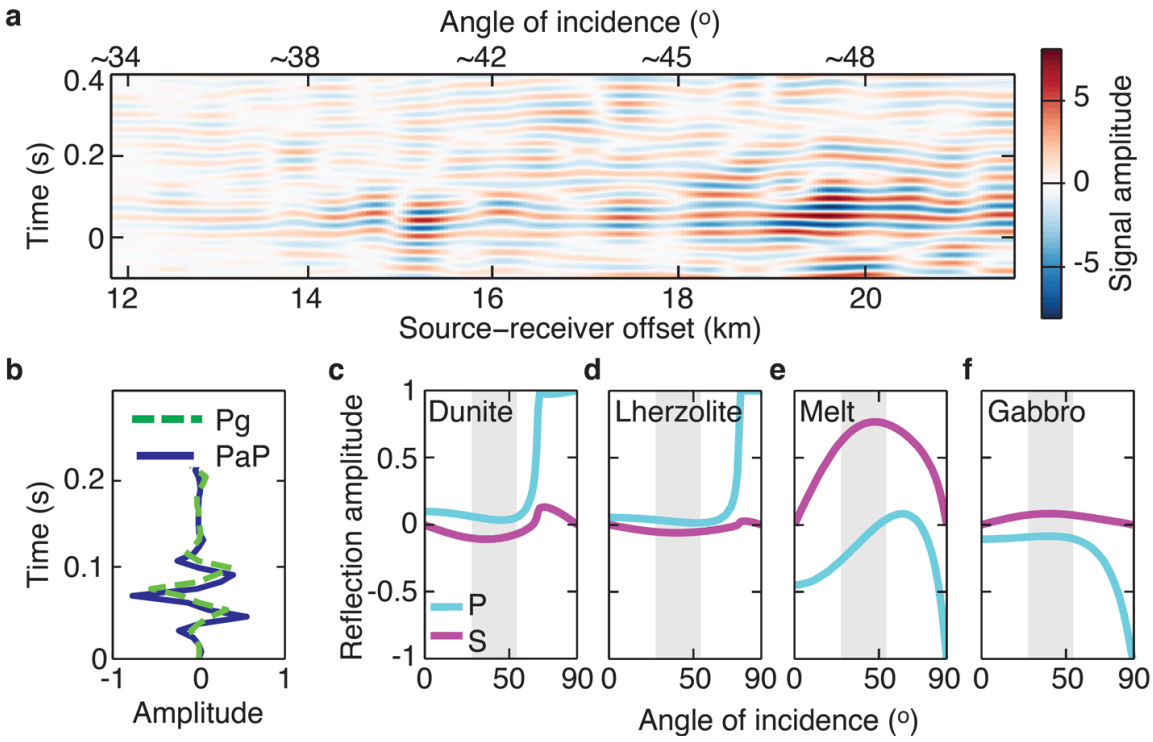

Figure S4. Observed and theoretical amplitude variation with offset (AVO). (a) AVO behavior for a subset of reflection events aligned by the onset time of the *PaP* arrival time for each trace, colored to show signal strength. Events are band-pass filtered between 20-60 Hz and were amplitude corrected for geometrical propagation effects. (b) PWS stack of *PaP* and *Pg* arrivals for the events shown in (a). Traces are aligned by the onset time of the respective arrival. Note the similar waveform structure. (c-f) Reflection coefficients for a *P*-wave incident upon a half space. Reflected *P*-wave amplitude (blue lines) and *S*-wave amplitude (red lines) are plotted as a function of incidence angle. The lithologic contact is formed by juxtaposing harzburgite with various lithologies (see text for details).

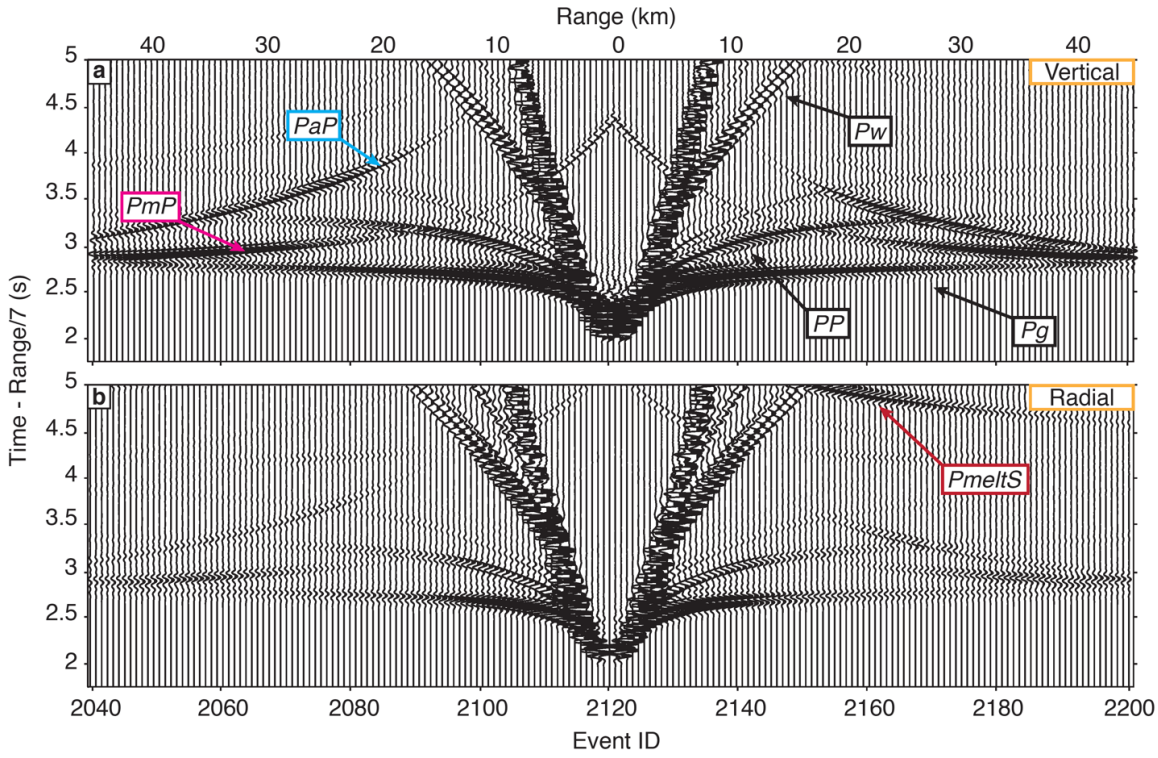

Figure S5. Synthetic record sections for a model with a 100-m-thick dunite that hosts a 7-m-thick gabbro melt lens embedded within the mantle. (a) Synthetic vertical record section showing amplification of the *PaP* arrivals relative to the dunite-only case shown in Figure 3. (d) Synthetic radial record section showing clear *PmeltS* arrivals generated from the mantle melt lens within the dunite layer. Record sections are band-pass filtered between 5 and 20 Hz; amplitudes are fixed scaled.

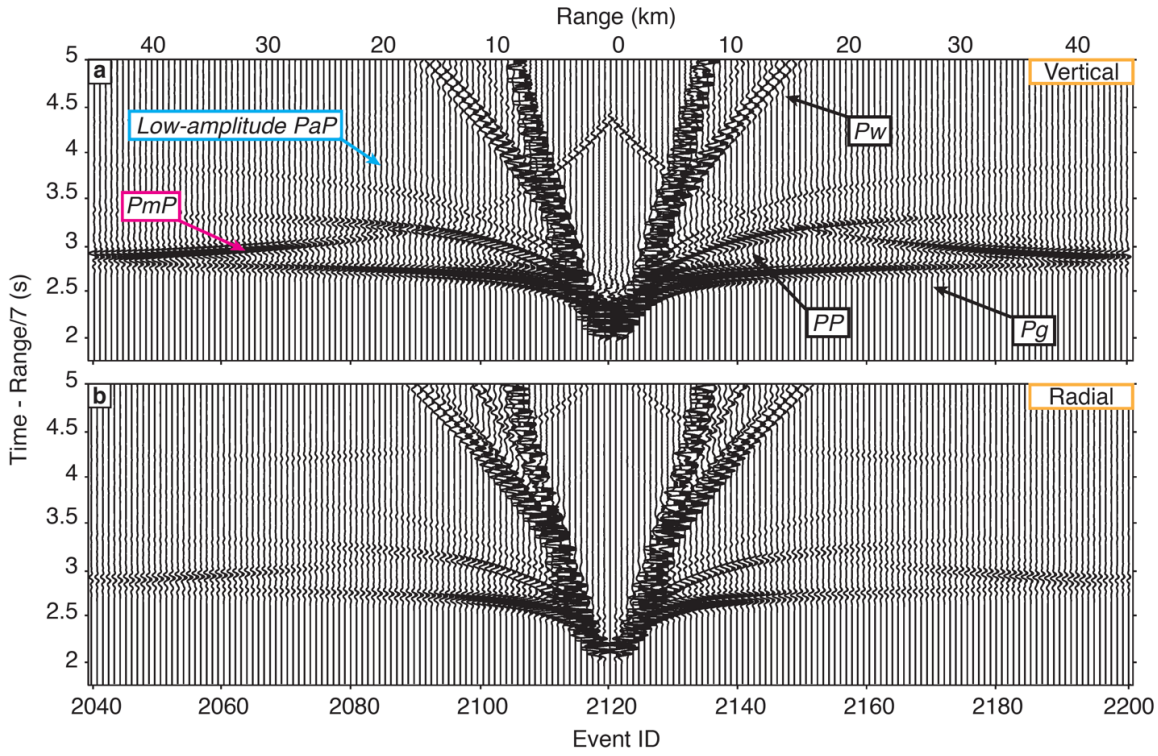

Figure S6. As in Figure S6, except for a 7-m-thick solid gabbro layer embedded within the 100-m-thick dunite layer. (a) Synthetic vertical record section showing significant reduction in the amplitude of the *PaP* arrivals relative to the dunite-only case shown in Figure 3. (d) Synthetic radial record section showing lack of *S*-wave arrivals. Record sections are band-pass filtered between 5 and 20 Hz; amplitudes are fixed scaled.

APPENDIX B

CHAPTER III SUPPORTING INFORMATION

Introduction

Our supporting information details the analytical process we used to arrive at and validate our preferred model. In this supporting document, we provide details of the process utilized for picking *PmP* arrivals, describe the inversion approach used to obtain our preferred model, and describe tests used to assess the resolution of our preferred model.

Text S1.

Picking PmP arrivals

In this study, we added hand-picked *PmP* travel-times to the existing *Pg*, *PmP*, or *Pn* travel-times used in previous studies (Weekly et al., 2014; Soule et al., 2016; VanderBeek et al., 2016). We adopted an iterative approach to compile our catalogue of *PmP* travel-times. To guide in the picking effort, we first generated predicted *PmP* travel-times using the model of Soule et al. (2016). Picks were then added by picking impulsive events within source-receiver offsets of 30-50 km; at these ranges, *PmP* typically have high-amplitudes and are most easily discernable. The range and number of picks was progressively expanded by inverting the data for velocity structure and generating new predicted *PmP* travel-times to aid in subsequent picking. Throughout this process, residuals were inspected to identify and modify or eliminate incorrect picks. Finally, we picked arrivals by plotting the data by azimuth to make use of trends in range-limited *PmP* arrivals (Figure 2c). This strategy was particularly useful for rise-crossing *PmP* arrivals, which tended to have decreased amplitudes relative to the rise-parallel *PmP*.

As secondary *PmP* arrivals can be challenging to pick, we adopted the strategy detailed by Soule et al. (2016) to improve the consistency of picks. This entails two approaches: (i) flattening record sections on the predicted travel-times of *Pg* from the model of *Weekly et al.* (2014) to remove the effect of complex bathymetry on the timing of *PmP* arrivals and (ii) picking the second cycle of the *PmP* waveform and then applying a correction to adjust it to the onset of the first cycle. Because the onset of the *PmP* waveform is often obscured by the coda, it is easier to identify the onset of the larger amplitude second cycle of the *PmP* arrival and subsequently apply a time correction of -0.05 s (Soule et al., 2016). Depending on the signal-to-noise ratio for each instrument channel, data were either picked on the vertical geophone or hydrophone channel, or the two were stacked. A majority of the *PmP* arrivals picked were on stacked channels, which tended to have higher signal-to-noise ratios.

Pick uncertainties were estimated visually, with larger uncertainties assigned to groups of waveforms with significant trace-to-trace variability or where *PmP* appeared to be interacting with the *Pg* arrival or other coda. Uncertainties at the one-sigma level ranged from 10 to 25 ms. We incorporated picks from 20-70 km offset.

Text S2.

Inversion approach

We adopted a three-step inversion approach to obtain a preferred model that includes segment-scale isotropic and anisotropic structure within the crust and topmost mantle, as well as crustal thickness: (i) inversion of *Pg* travel-times following the inversion strategy of Weekly et al. (2014) with a modified anisotropy symmetry axis, described in section 4.2, and penalties applied to anisotropy, (ii) joint inversion of *Pg* and *PmP* to constrain the velocity structure of the lower crust and crustal thickness, and (iii) inversion

of *Pn* using the preferred crustal model to constrain the segment-scale mantle structure. We describe each of these steps below. Only step (i) inverted for the anisotropic structure, though imposed anisotropic structure was included in the forward calculations for steps (ii) and (iii) as described below. For each inversion step, we searched over horizontal and vertical smoothing values and chose those which provided a smooth solution that fit the data well. Travel-time calculations and inversion for model parameters were performed until the RMS travel-time residual converged (typically 10 iterations for just *Pg* and 3–5 iterations for subsequent steps).

First, we inverted the *Pg* data following the inversion strategy of Weekly et al. (2014) to produce a shallow crustal model of isotropic and anisotropic heterogeneity that serves as the basis for subsequent inversions to constrain deeper structure. This was done assuming a slow-symmetry axis characteristic of fluid-filled cracks and utilized a jumping inversion strategy (Shaw & Orcutt, 1985). Penalties were also applied to the anisotropic structure to prevent large perturbations in regions of poor *Pg* ray coverage; if left unchanged, these anomalous anisotropic regions would influence the misfit of *PmP* travel-times. This step resulted in a model with reduced magnitude of anisotropy in the off-axis portions of the model space, but increased magnitudes near the ridge axis relative to the model of Weekly et al. (2014). The resultant isotropic component of the velocity structure is similar to that of Weekly et al. (2014). Our preferred model was obtained using a jumping strategy with λv=300, λxy=200, λp=1 for isotropic slowness, λav=400, λaxy=400, λap=5 for anisotropic structure, and converged to a RMS of 11.2 ms and χ^2-misfit of 1.08. The resulting crustal model was modified for subsequent joint *Pg* and *PmP* inversions by downward continuing velocities at 4 km depth to the base of the model and inserting an initial Moho interface, modeled as a smoothed version of the seafloor, at a depth of 6.8 km

below the seafloor. Anisotropy from the *Pg* inversion was not modified, as anisotropic structure below 4 km depth is low (<2%) everywhere except beneath Middle Valley segment and to the north of North Symmetric segment, which are characterized by comparatively higher anisotropy (2-4%) down to 5 km depth (Figure S2); within the non-overlapping portion of the segment, anisotropy below 4 km depth is predominantly <1%.

In the second step, we jointly inverted *Pg* and *PmP* travel-times for the structure of the mid- to lower crust and Moho depth. We used *PmP* residuals to investigate the presence of segment-scale anisotropy within the lower crust. To estimate the anisotropic signal within the lower crust, we used our preferred crustal model derived from steps (i) and (ii) in section 4.2 to investigate azimuthal variations in *PmP* travel-time residuals. Using the method described by Vanderbeek et al. (2016), the lower crustal anisotropy was estimated to have a magnitude <0.5%. We therefore did not impose or invert for lower crustal anisotropy. The forward calculation included the unaltered anisotropic structure from step (i) and was held fixed during the inversion, such that we only inverted for the isotropic component of the velocity structure. The preferred model was obtained using a creeping inversion strategy with λv=300, λxy=200, λp=1 for isotropic slowness, λiv=600, λixy=600, λip=1 for the Moho reflector, and converged to a RMS of 11 (χ^2 = 1.02) and 16 ms (χ^2 = 0.87) for *Pg* and *PmP*, respectively.

We then used the method described by VanderBeek et al. (2016) to estimate segment-scale anisotropic structure within the mantle relative to an isotropic, homogeneous (7.6 km/s) mantle. Despite the change between our preferred crustal velocity model and crustal thickness relative to that used by VanderBeek et al. (2016), the anisotropic mantle signal was similar. In particular, the new estimate for the fast-axis orientation and magnitude of anisotropy are slightly lower than those from VanderBeek et

al. (2016), decreasing from 122°±1° to 120°±1° and 4.7 ± 0.4% to 3.7 ± 0.5%, respectively. We inserted this new estimate for anisotropic mantle structure into the preferred model; relative to the plate-spreading direction, the fast-axis orientation is skewed clockwise by 10°. Finally, we inverted *Pn* to constrain isotropic slowness perturbations within the mantle, holding the crustal structure and Moho interface fixed. Once again, anisotropy was included in the forward calculation and held fixed during the inversion. Our preferred model was obtained using a jumping inversion strategy (Shaw & Orcutt, 1985) with λv=200, λxy=200, λp=1 for isotropic slowness and converged to a RMS of 11.2 ms and χ^2-misfit of 1.2

Text S3.

Resolution

We identify the regions in which our preferred model is well-resolved through the analysis of the spatial distribution of ray paths. Specifically, we use the derivative weight sum (DWS) to measure the density of predicted ray paths that influence each perturbational node in the inversion volume (Toomey and Foulger, 1989). On the basis of checkerboard resolution tests (discussed below), anomalies located within regions of the model space where the DWS is less than ~10 are poorly reconstructed and we therefore mask those regions of the model space (Figures 3-6).

To further assess the resolution of crustal and mantle isotropic structure, we employ three-dimensional synthetic checkerboard tests. We constructed multiple synthetic models with alternating sinusoidal patterns of positive and negative isotropic anomalies with a mean magnitude of ±5% (maximum magnitude ±7%) applied to the preferred isotropic model. The first synthetic model consisted of 4x4x2 km^3 cubic anomalies that alternated with depth (Figures S1a-1c). The second model consisted of 6x6x2 km^3 anomalies (Figures

S1d and S1e). We imposed the final crustal anisotropic structure in the crustal sections of our preferred anisotropic model for each synthetic test. We calculated travel-times for *Pg* and *PmP* phases for the same data geometry used to constructed our preferred solution. Each *Pg* travel-time was then assigned an uncertainty of 11 ms and random noise with a standard deviation of 11 ms was applied to the synthetic *Pg* data. Likewise, we assigned an uncertainty of 18 ms for *PmP* travel-times and applied random noise with a standard deviation of 18 ms to the *PmP* data. The synthetic data were then jointly inverted for isotropic perturbations following the same inversion procedure used in our preferred solution.

The recovered checkerboards for the 4x4x2 km^3 and 6x6x2 km^3 models indicate that we underestimate amplitudes, but constrain along-axis crustal variations (Figures S1a-e). The dimensions of checkerboards are well-recovered throughout the crust, though the amplitudes are largely underestimated by approximately 40-50%. However, the amplitude recovery of anomalies within 5 km of the ridge is consistent along-axis, indicating that we are able to constrain along-axis variability despite the inability to recover absolute amplitudes. Both crustal checkerboards models indicate that crustal structure is well-constrained within 30 km of the plate boundary down to ~4 km (Figures S1a and S1d). Crustal resolution, however, decreases within the lower crust such that 4x4x2 km^3 and 6x6x2 km^3 anomalies are recovered within 15 and 25 km of the plate boundary, respectively (Figures S1b and S1e).

We also constructed synthetic tests to assess model resolution of mantle structure and crustal thickness. The mantle synthetic test was conducted in a similar fashion to the crustal tests, but with 10x10x2 km^3 cubic anomalies oriented in a N-S direction to mimic the mantle structure of our preferred solution (Figure S1f). We imposed 3.7% mantle

anisotropy with a fast axis rotated 10° clockwise from the plate-spreading direction. Calculated travel-times through this synthetic model were assigned an uncertainty of 11 ms and random noise with a standard deviation of 11 ms was applied to the *Pn* data. The results of this test indicate that the amplitudes of mantle anomalies, similar to those within the crust, are underestimated by 40-50%. The dimensions of anomalies are more poorly resolved that the crustal checkerboards, though they are relatively well-recovered within ~10-20 km of the plate boundary along most of the segment (Figure S1f); to the west of the southern end of the Endeavour segment, resolution is diminished. We assessed the resolution of the asymmetric crustal thickness anomalies by generating a synthetic Moho interface with a constant of depth of 6.8 km and two sinusoidal, asymmetric 20x20 km^2 anomalies with a maximum thickness variation of 1 km (Figure S1g). Synthetic travel-times generated using this model were assigned an uncertainty of 18 ms and random noise with a standard deviation of 18 ms was applied to the *PmP* data. The results indicate we are able to accurately resolve such variations in Moho structure (Figure S1g).

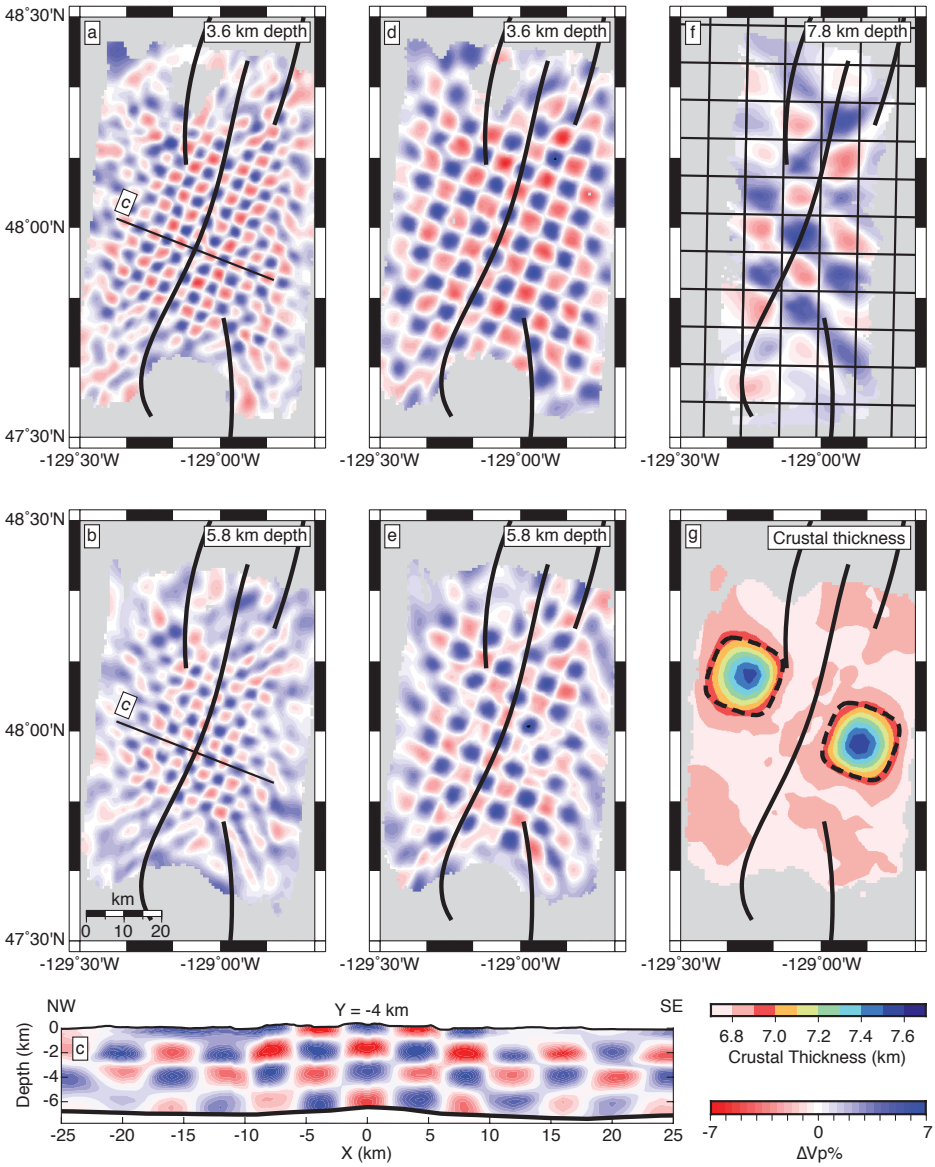

Figure S1. Checkerboard synthetic tests and resolution. (a and b) Map view depth slices of recovered 4x4x2 km^3 sinusoidal checkerboard anomalies at (a) 3.6 km and (b) 5.8 km depth. Thin black line indicates the cross-section shown in (c). (c) Cross-section through recovered 4x4x2 km^3 checkerboard model. Bold black line indicates the Moho. (d and e) Map view depth slices of recovered 6x6x2 km^3 sinusoidal checkerboard anomalies at (d) 3.6 km and (e) 5.8 km depth. (f) Recovered sinusoidal checkerboard anomalies embedded within the mantle. The wavelength of the anomalies is 10 km in both x- and y-directions. Black gridlines mark the boundary between the true alternating positive and negative velocity perturbations. The true sinusoidal anomalies in Figures 8a-e have a mean amplitude of ±5%, with a maximum amplitude of ±7%. (g) Recovered crustal thickness anomalies characterized by sinusoidal features of 1-km thickened crust, or maximum thickness of 7.7 km. Dashed black line indicates the boundary of the thickness anomalies. Bold black lines in map-view sections indicates the plate boundaries.

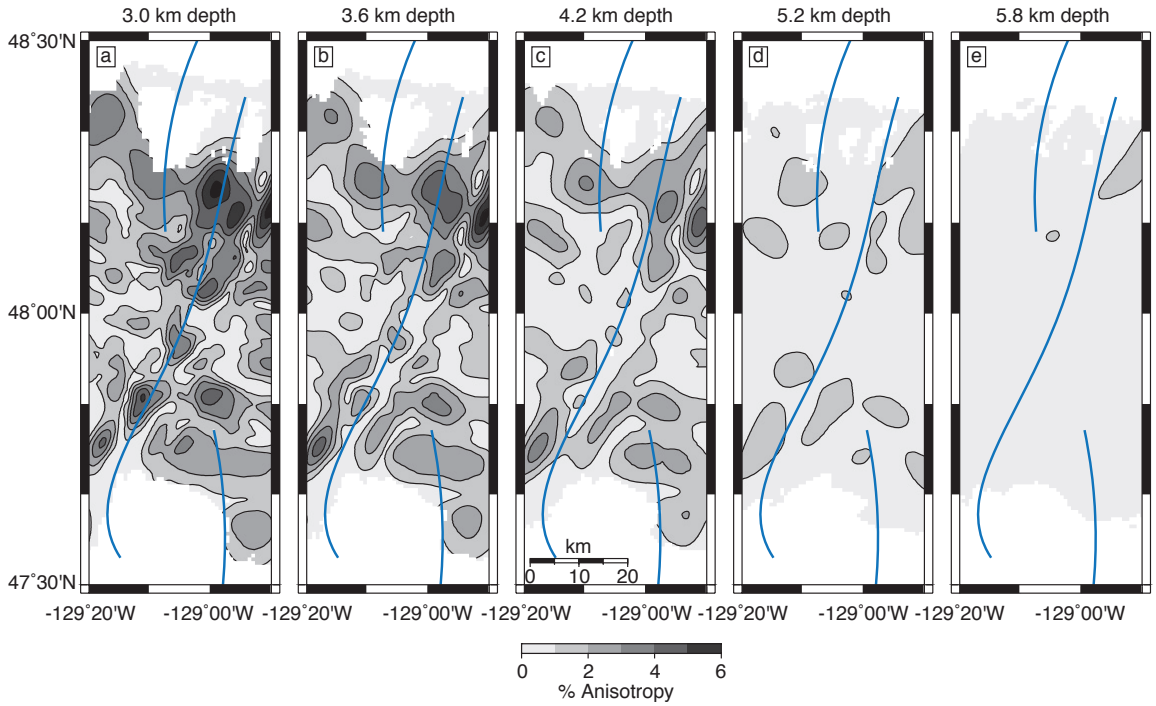

Figure S2. Map-view sections showing the magnitude of anisotropy at (a) 3.0 km depth, (b) 3.6 km depth, (c) 4.2 km depth, (d) 5.2 km depth, and (e) 5.8 km depth. Images are contoured at 1% intervals and masked where there is poor ray coverage (white regions). The traces of the plate boundaries are shown (blue lines).

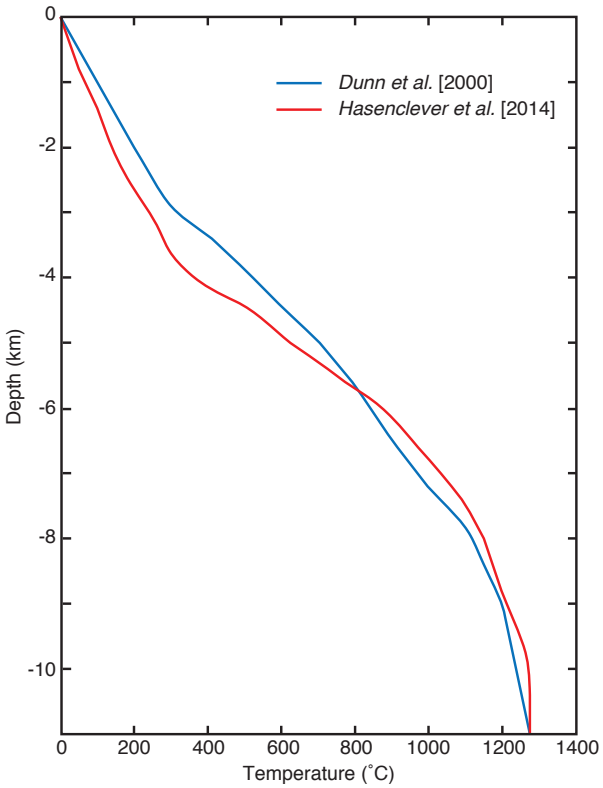

Figure S3. Comparison of temperature profiles used to estimate temperature from seismic velocity anomalies. The blue line is a profile located 10 km off-axis in the thermal model of Dunn et al. (2000) and used to generate the thermal models shown in Figures 7 and 8, as well as Figure S4. The red line is 10 km off-axis profile from the thermal model of Hasenclever et al. (2014), which was used to generate the thermal models in Figure S5.

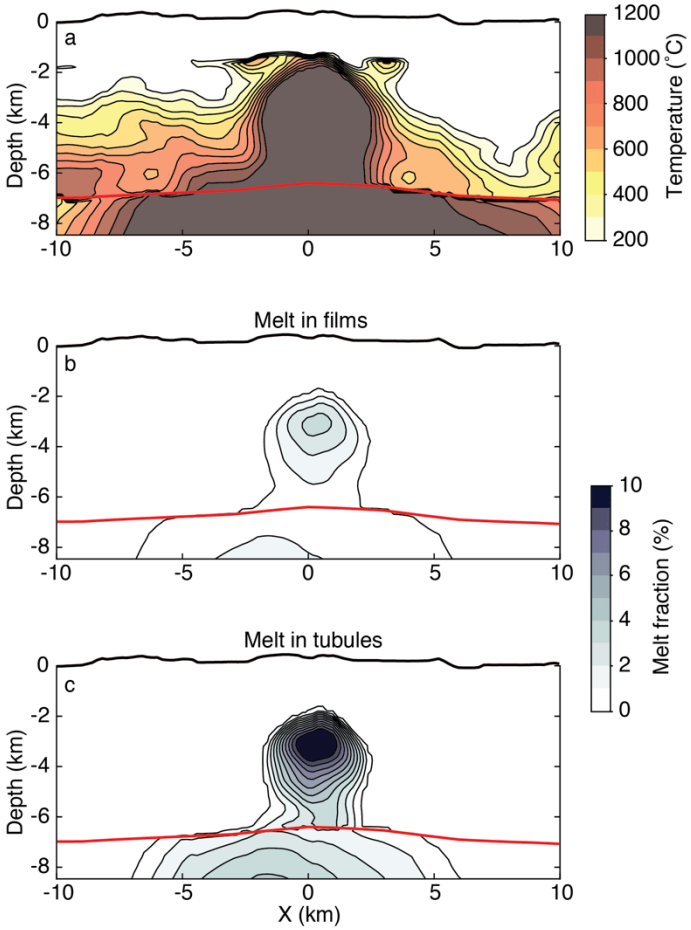

Figure S4. Anharmonic temperature and melt fraction models computed from the cross-axis section in Figure 5c. Temperature and melt fraction are contoured at 100°C and 1%, respectively. (a) Temperature model assuming only anharmonic effect, using the T(z) profile of Dunn et al. (2000) (Supplementary Figure 3). (b) Melt fractions calculated assuming anharmonic effects for which melt resides in thin films. (c) As for (b), except for melt residing in tubules. Large velocity reductions above 2 km depth (e.g., Figure 5) are attributed to porosity variations and are therefore removed from the temperature and melt fraction calculations.

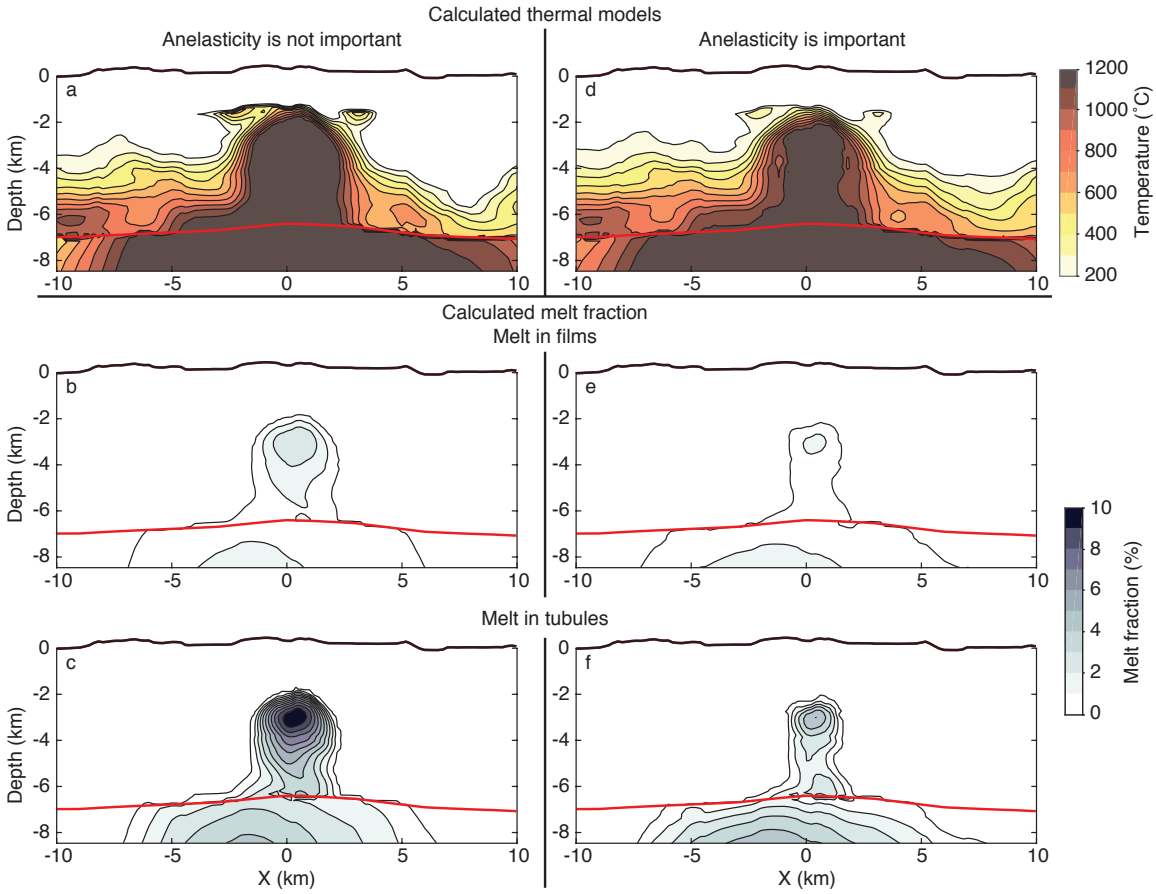

Figure S5. Temperature and melt fraction models computed from the cross-axis section in Figure 5c, using the cooler temperature profile of Hasenclever et al. (2014) (red line, Figure S3). Temperature and melt fraction are contoured at 100°C and 1%, respectively. (a) Temperature model assuming only anharmonic effects. (b) Melt fractions calculated assuming anharmonic effects for which melt resides in thin films. (c) As for (b), except for melt residing in tubules. Large velocity reductions above 2 km depth (e.g., Figure 5) are attributed to porosity variations and are therefore removed from the temperature and melt fraction calculations.

APPENDIX C

CHAPTER IV SUPPORTING INFORMATION

Introduction

Our supporting information describes the equation we use to convert absolute velocity to porosity and details the analytical process we used to assess and validate our preferred model. We also provide plots that show the following: hydrophone data from the ETOMO experiment; a comparison between the travel-time tomography and preferred FWI models; *P*-to-*S* conversions observed on the radial channel; the match between synthetic and field data; results of different stages of the inversion; a porosity model derived from the preferred velocity model; the results of synthetic checkerboard tests; a cross-section through the preferred velocity model; and map-view sections of the anomalous velocity.

Text S1.

Conversion from absolute velocity to porosity

To convert absolute crustal velocity to porosity, we applied equation 5 from Carlson (2014) (Equation S1), which relates porosity (Φ) to seismic velocity in crustal rocks (υ_r) via a quadratic function for suites of rocks that have narrow ranges of grain densities and elastic moduli, such as basalts and gabbros:

$$\Phi(v_r) = \frac{-b \pm \sqrt{b^2 - 4a\left(c - \frac{1}{v_r^2}\right)}}{2a} \tag{S1}$$

The quadratic coefficients—*a*, *b*, and *c*—are functions of asperity contact across the cracks, a measure of crack morphology, and were estimated by making a nonlinear fit to Equation S1 to log velocity and porosity data (Carlson, 2014). The values, standard errors, and relative errors for these coefficients are shown in Table S1. This equation is empirically

derived from borehole data of 6-15 Ma oceanic crust and is therefore not entirely suitable for young oceanic crust. In particular, the best fitting model for the conversion from velocity to porosity does not accurately predict porosities typical of layer 2A in very young crust, likely owing to a decrease in porosity with crustal age (Carlson, 2014). For this reason, we have only applied the equation to crustal velocities from 1-3 km below seafloor and therefore avoid estimating the porosity within layer 2A (Figures S12 and S13).

Table S1. Modified from Table 1 in Carlson (2014). Quadratic coefficients and their associated values, standard errors, and relative errors for lavas and dikes.

	Lavas			Dikes		
Quadratic coefficients	Value	s.e.	r.e.	Value	s.e.	r.e.
a	-0.129	0.011	0.089	-0.212	0.013	0.061
b	0.181	0.017	0.098	0.311	0.020	0.064
c	0.0258			0.0217		

Text S2.

Model Resolution

We identify the regions in which our preferred velocity model is well resolved by analyzing the spatial distribution of ray paths using travel-time tomography (Toomey and Foulger, 1989). A spatial measure of the distribution of *Pg* ray paths within the model volume is given by the derivative weight sum (DWS) (Thurber, 1983; Toomey et al., 1994), which is a measure of the density of predicted ray paths influencing each node in the perturbational grid. On the basis of checkerboard resolution tests (discussed below), anomalies located within regions of the model space with a DWS less than 10 are poorly

reconstructed. We therefore mask regions of the model with a DWS below 10; below this threshold, interpretations drawn from the results were not made. Owing to the limited extent of the crustal grid, ray path distribution in the outer edge of the model space was sparse at more than 1.2 km below the seafloor (bsf; Figures S11d-g). The central portion of the crustal grid, however, was densely sampled to 2.4-3 km bsf (Figures S11f-g).

We assess the resolution of crustal structure using checkerboard tests. We constructed synthetic models with an alternating pattern of positive and negative isotropic velocity anomalies with a magnitude of 3% applied to the starting FWI model. Synthetic seismograms were calculated using the same data geometry used to construct our preferred solution and processed the same way as the field data. These processed seismograms were then inverted for velocity perturbations following the same inversion procedure used in our preferred solution. Here we show two checkerboard tests: (1) a vertical synthetic checkerboard model with 1-km-by-1-km-by-1-km tiles centered along the ridge axis at X = 0 km, extending from the seafloor to the base of the model (Figure S8) and (2) a horizontal synthetic checkerboard model with 1.5-km-by-1.5-km-by-1.5-km tiles placed between 2 and 3.5 km bsf and extending from X = -10 to X = 10 and Y = -14 to Y = 13 (Figure S9). In the vertical checkerboard test, anomalies near the seafloor are approximately 800 m in the z dimension owing to the way in which the checkerboard anomalies were applied to the model (i.e., not parallel to the seafloor). In general, the distribution of recovered crustal perturbations accurately reflects the true checkerboard models. The locations of low-velocity anomalies near the ridge axis are well recovered while the magnitudes are typically underestimated below 2.5 km bsf. Our checkerboard tests indicate crustal structure on the order of 0.8-1 km^3 is well constrained in the upper 3

km, although features on the order of 1.5 km^3 are better constrained at depth—a remarkable improvement over the resolution of the travel-time tomography results (Weekly et al., 2014). Additional synthetic tests are presented in Morgan et al. (2016).

Text S3.

Model fitness

In order to judge the fit of the preferred model, we examine the phase match between the field data and synthetics generated using the preferred model (Figures S5 and S6). This can be accomplished in two ways: (1) subtracting the phase of the observed data from that of the synthetic data (Figures S5a and S6) and (2) comparing the traces of the observed and synthetic data (Figure S5b). Using the former method, phase residuals near zero (green in Figure S5a) indicate a good match between the observed and synthetic data. Figure S5a shows the phase residuals for all traces within 2.9 to 15 km from OBS 54 (figure is masked in regions where traces were not used in FWI). Aside from a few traces, the phase residual is at or near zero, indicating the model is capable of predicting the observed data. The improvement from the starting to final model is also evident in the phase residuals for the traces recorded on all of the instruments, as the final model has a smaller standard deviation than the starting model within offsets of 15 km (Figure S6). Traces with higher residuals may indicate the presence of noise that FWI is incapable of matching. Figure S5b compares the observed and synthetic traces for a subset of events from shot line 15 recorded on OBS 54. For the most part, the observed and synthetic traces are quite close, further indicating a good model fit. More information pertaining to the model fitness and how the inversion is monitored are provided in Morgan et al. (2016).

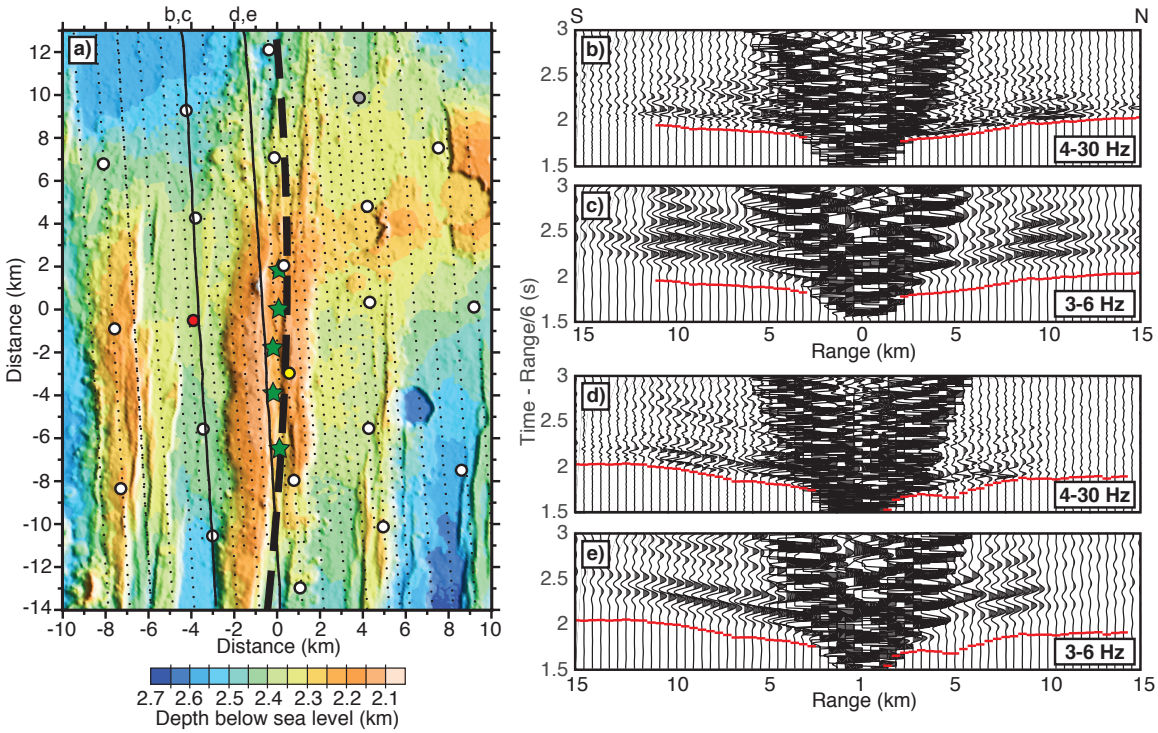

Figure S1. Experiment geometry and example record sections with *Pg* travel-time picks (red lines) overlain. (a) Bathymetric map of the crustal grid of the ETOMO experiment showing OBSs (large white circles), air gun shots (black dots), hydrothermal vents (green stars), and the plate boundary (dashed black line). Grey circle indicates an OBS that did not record data useable for FWI, whereas red and yellow circles indicate OBSs for which data is shown in (b, c) and (d, e), respectively. Two bold black lines show shot lines for the record sections shown in (b-e). (b-e) Example record sections of data prior to preprocessing for FWI. Redlines indicate Pg picks used for travel-time inversion (Weekly et al., 2014). Waveform data are band-pass filtered between (b, d) 4-30 Hz and (c, e) 3-6 Hz and plotted with a reduction velocity of 6 km/s.

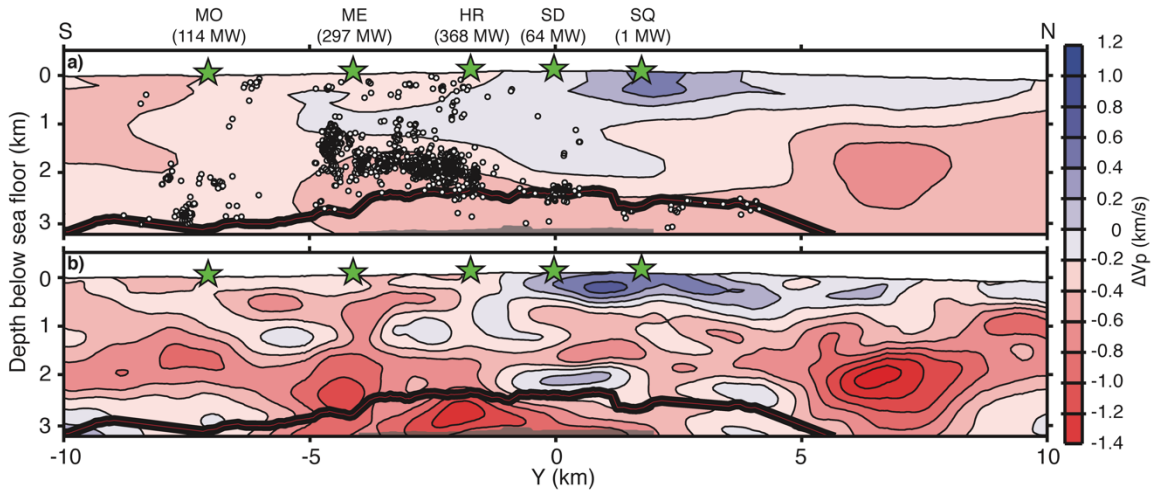

Figure S2. Along-axis comparison of travel-time tomography and FWI results. (a) Along-axis section (X = 0.1 km, see Figure 1b) of the final travel-time tomography model. Three-dimensional velocity anomalies are plotted relative to a horizontal average of the travel-time tomography model (Weekly et al., 2014). (b) Same as (a), except for the final FWI model. Three-dimensional velocity anomalies are plotted relative to a horizontal average of the starting model for FWI and masked in regions where the derivative weight sum is less than 10 (see text S1). Plotted features are the same as those in Figure 2a.

Figure S3 (next page). Across-axis comparison of travel-time tomography and FWI results. Across-axis sections of the final (a-d) travel-time tomography and (e-h) FWI models. Vertical sections crossing the ridge axis at (a, e) Mothra (Y = -7 km), (b, f) Main Endeavour (Y = -4.1 km), (c, g) High Rise (Y = -1.7 km), and (d, h) Salty Dawg (Y = 0 km), masked in regions where the derivative weight sum is less than 10 (see text S1). Overlain are the hypocenters for earthquakes recorded between 2003 and 2004 (white circles) (Wilcock et al., 2009), vent field locations (green stars), and the AMC reflector (red and black line) (Van Ark et al., 2007). Heat fluxes of are provided above each vent (Kellogg, 2011).

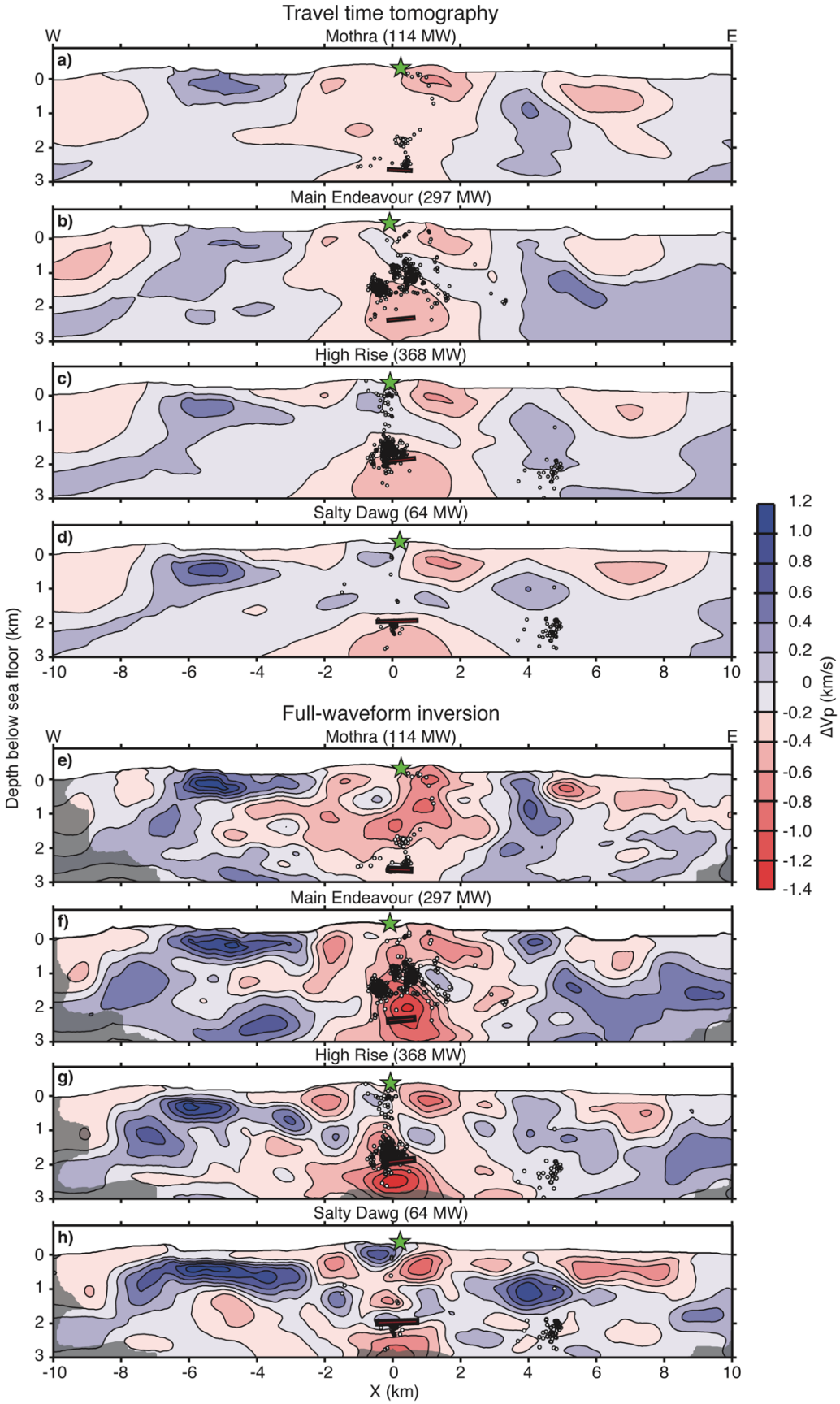
Travel time tomography
W
Mothra (114 MW)
E
a)
Main Endeavour (297 MW)
b)
High Rise (368 MW)
c)
Salty Dawg (64 MW)
d)
Full-waveform inversion
e)
f)
g)
h)
Depth below sea floor (km)
X (km)
ΔVp (km/s)
1.2
1.0
0.8
0.6
0.4
0.2
0
-0.2
-0.4
-0.6
-0.8
-1.0
-1.2
-1.4

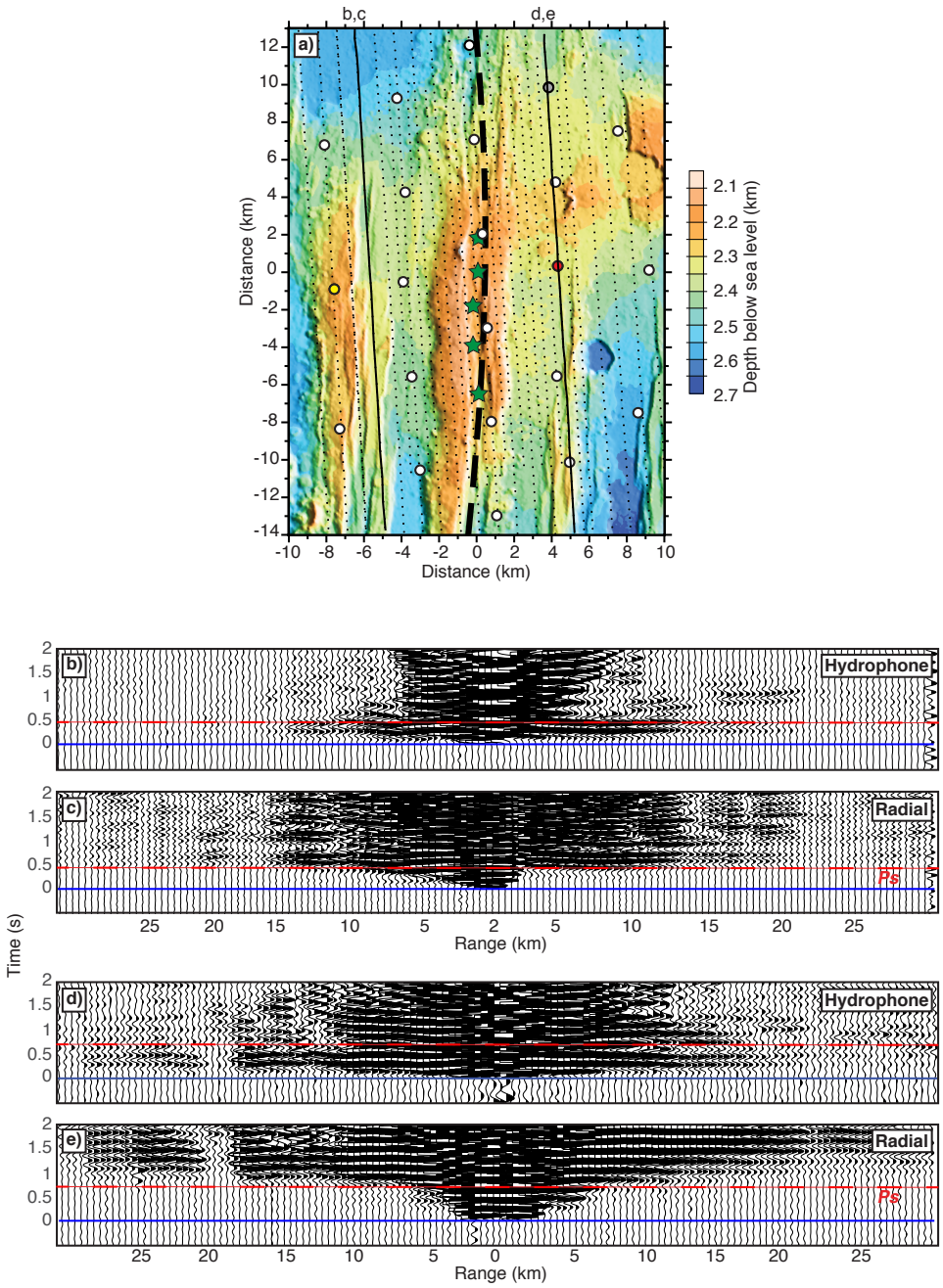

Figure S4. *P*-to-*S* conversions at the base of layer 2A, *Ps*, recorded on the radial channel and examples of hydrophone data. (a) Bathymetric map of the crustal grid of the ETOMO experiment showing OBSs 60 (yellow circle) and 39 (red circle) for which data is shown in (b, c) and (d, e), respectively. Other features are the same as those shown in Figure S1a. Two bold black lines show shot lines for the record sections shown in (b-e). (b, c) Hydrophone and radial components of OBS 60. Radial shows *Ps* at 500 ms (dashed red line). Energy from this arrival is not observed on the hydrophone. (c, d) Hydrophone and radial components of OBS 39. Radial shows *Ps* at ~750 ms (dashed red line), outside the window used for this study. The energy from this arrival is not observed on the hydrophone.

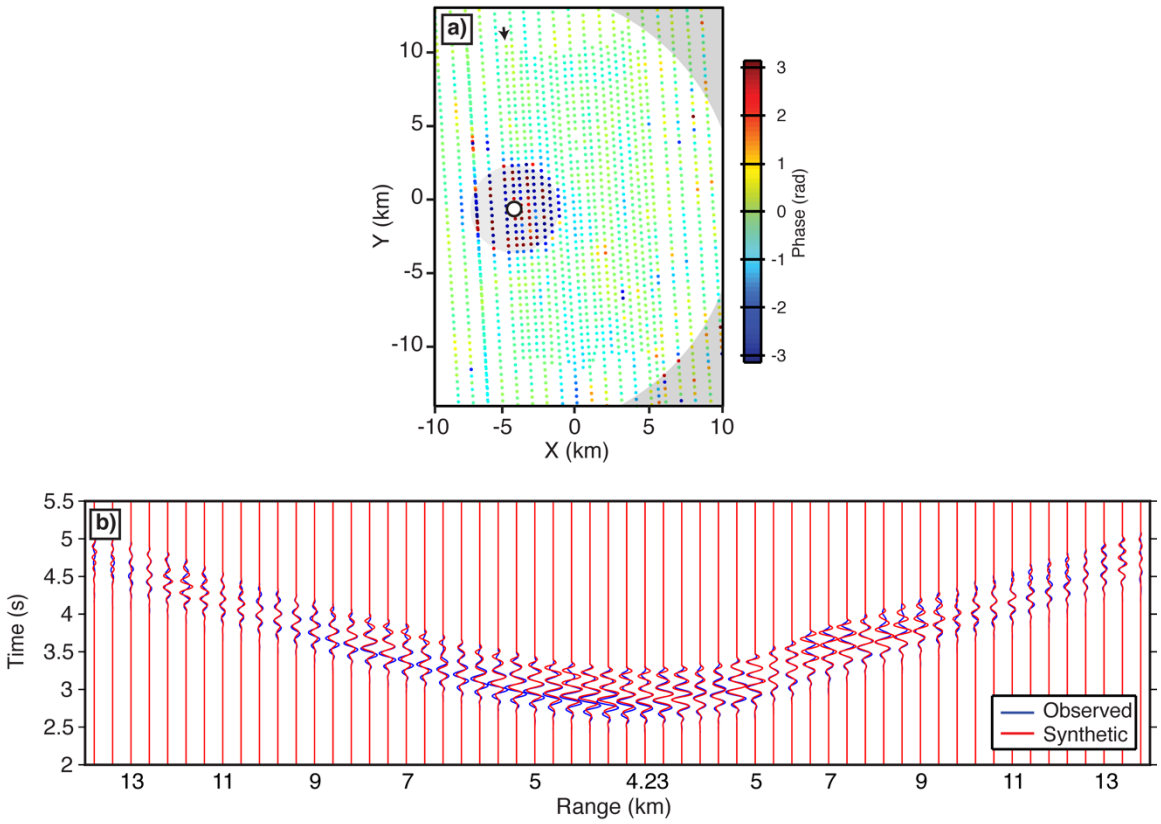

Figure S5. Phase residuals for an ETOMO OBS and trace comparisons. (a) Phase residuals (synthetic minus observed), in radians, for shots recorded on OBS 54 (white circle) within 2.9 to 15 km offset from the receiver at 5.1 Hz. Masked regions encompass traces that were not used for FWI. Events from shot line 15 (marked by arrow) are shown in (b). (b) Comparison of observed (blue) and synthetic (red) traces for a subset of events along shot line 15; the traces have been processed the same way described in section 2.2 of the main text and only include the first 750 ms of data after the onset of the first arriving crustal refractions (black lines). Observed and synthetic traces are each normalized by their respective aggregate mean RMS (i.e., a single scalar value).

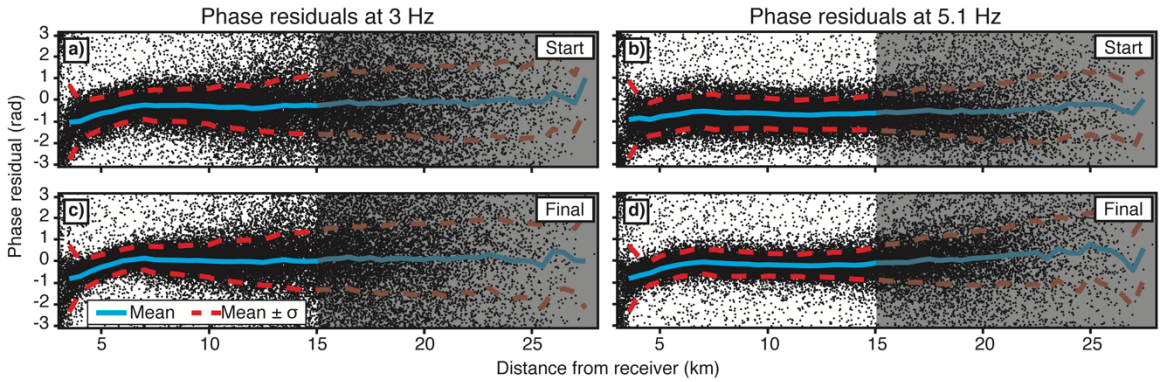

Figure S6. Phase residuals with offset prior to and after application of FWI. Phase residuals for the starting model at low-pass cutoff frequencies of (a) 3.0 and (b) 5.1 Hz for all shots within the crustal grid. Phase residuals for the final model at low-pass cutoff frequencies of (c) 3.0 and (b) 5.1 Hz for all shots within the crustal grid. Solid blue lines show the mean phase residual and the dashed red lines show the mean ± the standard deviation. Masked regions encompass traces that were not used for FWI.

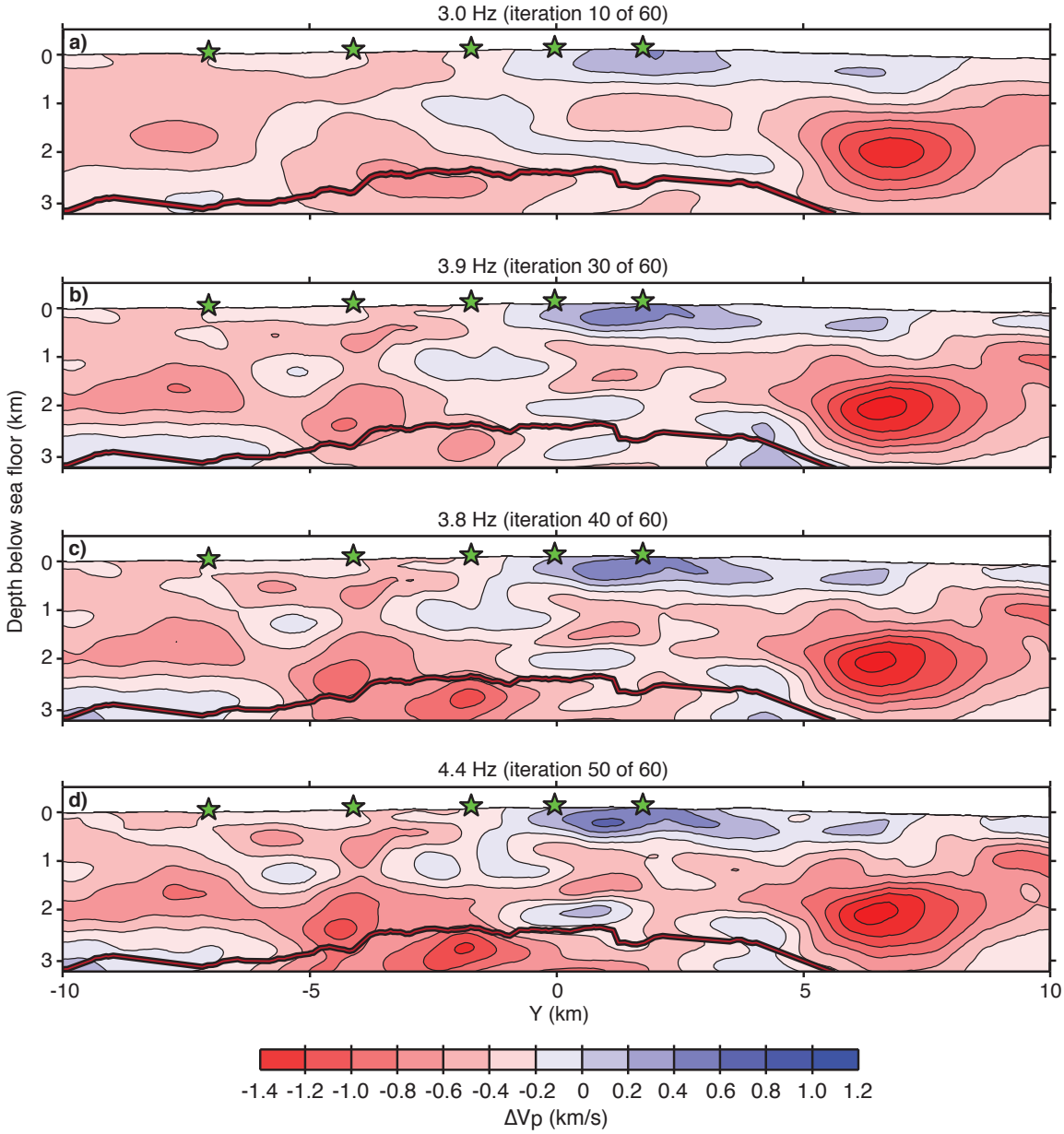

Figure S7. Along-axis sections showing the results of the inversion leading to the preferred model. The inversion consisted of sixty iterations at a total of seven different low-pass cutoff frequencies (section 2.2 in main text). Hydrothermal vents (green stars) and the axial magma chamber reflection (red and black line) are overlain.

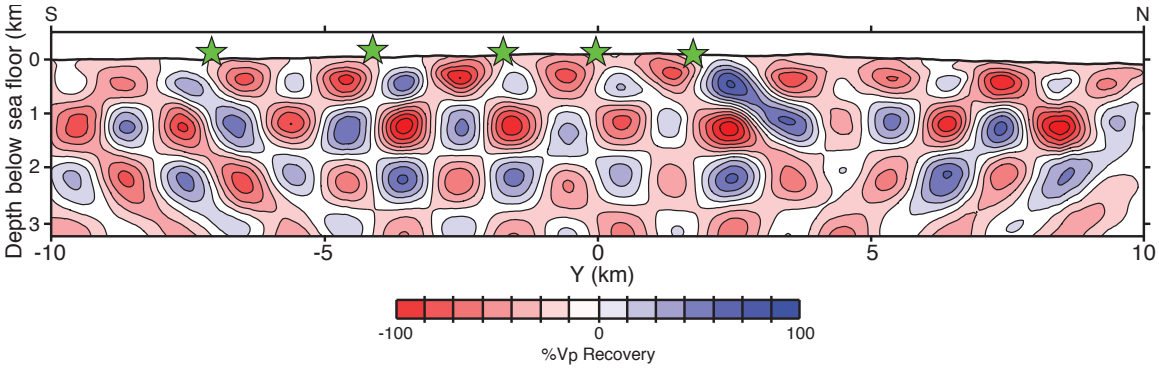

Figure S8. Recovered vertical checkerboard. The recovery of synthetic crustal checkerboard-patterned anomalies is shown at $X = 0.1$ km. The true model contains 1 km^3 columnar velocity perturbations of ±3% *Vp* applied to the starting velocity model. Velocity anomalies alternate with depth and are only located within ±0.5 km of $X = 0$ km. The color contours show the percent recovery of *P* wave perturbations with a contour interval of ~14% *Vp*. The green stars show the location of the hydrothermal vents.

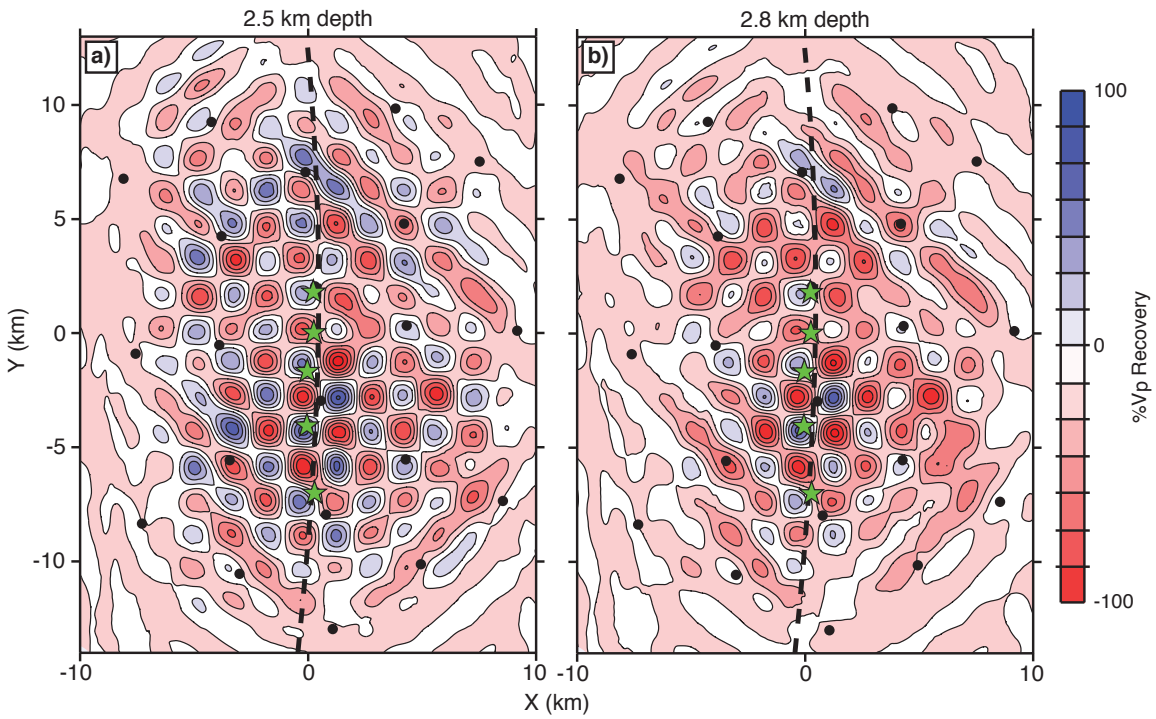

Figure S9. Recovered horizontal checkerboard. The recovery of synthetic crustal checkerboard-patterned anomalies is shown at (a) 2.5 and (b) 2.8 km beneath the seafloor (bsf). The true model contains 1.5-km^3 columnar velocity perturbations of ±3% *Vp* applied to the starting velocity model. Velocity anomalies do not vary with depth and are only located between 2 and 3.5 km bsf. The color contours show the percent recovery of *P* wave perturbations with a contour interval of ~14% *Vp*. The dashed black lines and green stars show the location of the plate boundary and hydrothermal vents, respectively.

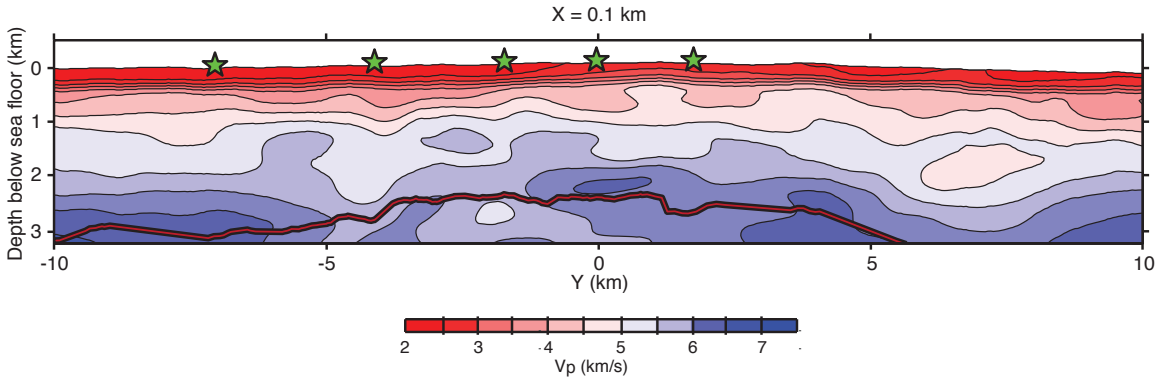

Figure S10. Along-axis section of the preferred *P* wave velocity model. Plotted features are the same as those in Figure S6. Contour interval is 0.5 km/s.

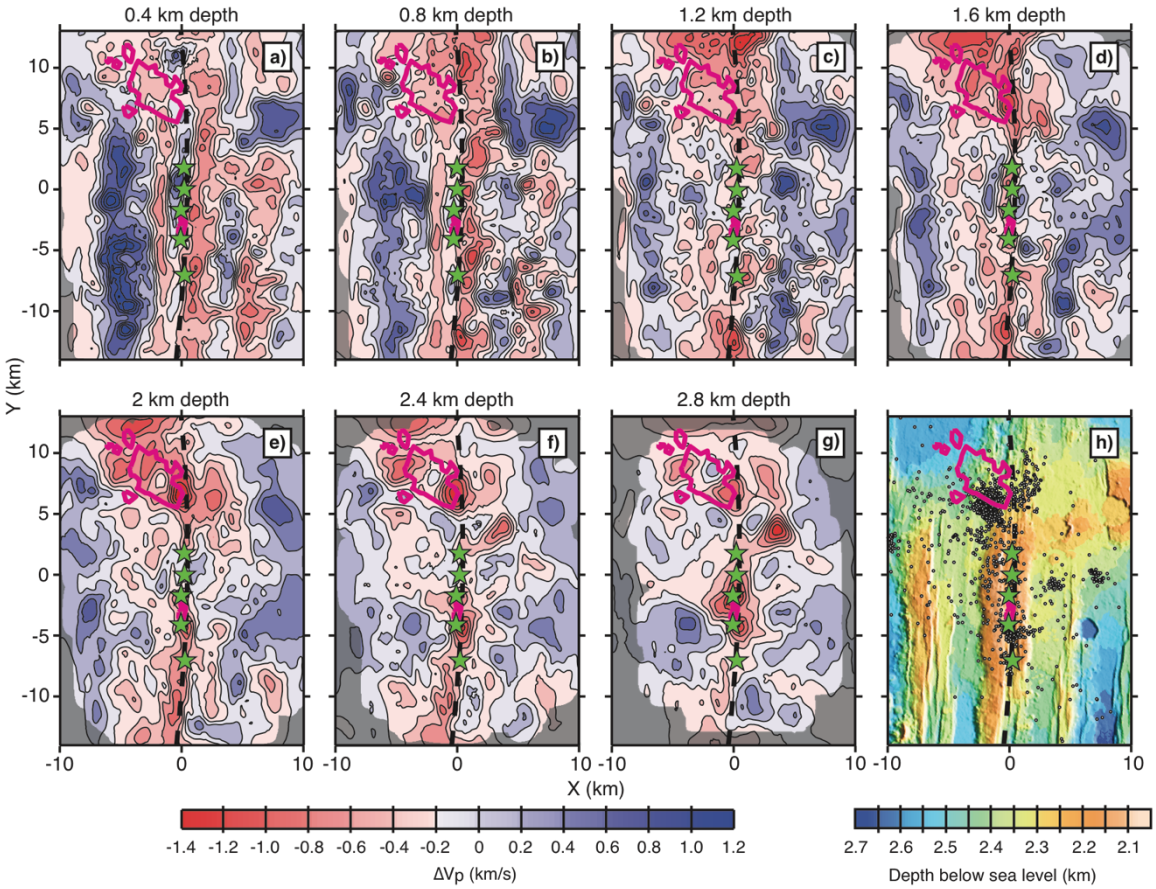

Figure S11. Map view sections of three-dimensional velocity anomalies. (a-g) Horizontal slices through the FWI model are presented at 0.4 km depth intervals with a contour interval of 0.2 km/s and masked where the derivative weight sum is less than 10 (see text S1). Thick dashed line and green stars indicate the plate boundary and vent fields, respectively. Magenta contours show areas with earthquake densities >20 events per km^2 recorded during the February 2005 swarm (Hooft et al., 2010). (h) Bathymetric map of the area shown in (a-g). White circles are epicenters of post-swarm earthquakes that occurred between October 2005 and June 2006 (Weekly et al., 2013).

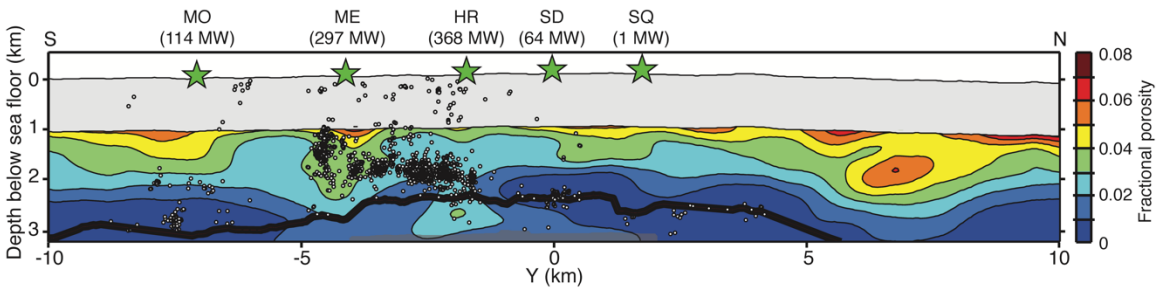

Figure S12. Along-axis cross-section through the preferred velocity model converted to porosity. Fractional porosity of the crust from 1-3 km bsf. The contour interval is 0.01. Grey region extending from 0-1 km bsf is the region where porosity was not calculated. Plot is masked in regions where the derivative weight sum is less than 10 (see text S1). Section shows vent field locations (green stars), hypocenters for earthquakes recorded between 2003 and 2004 (white circles) (Wilcock et al., 2009), and AMC reflector (red and black line) (Van Ark et al., 2007). The heat fluxes of the five vent fields are provided above each vent (Kellogg, 2011).

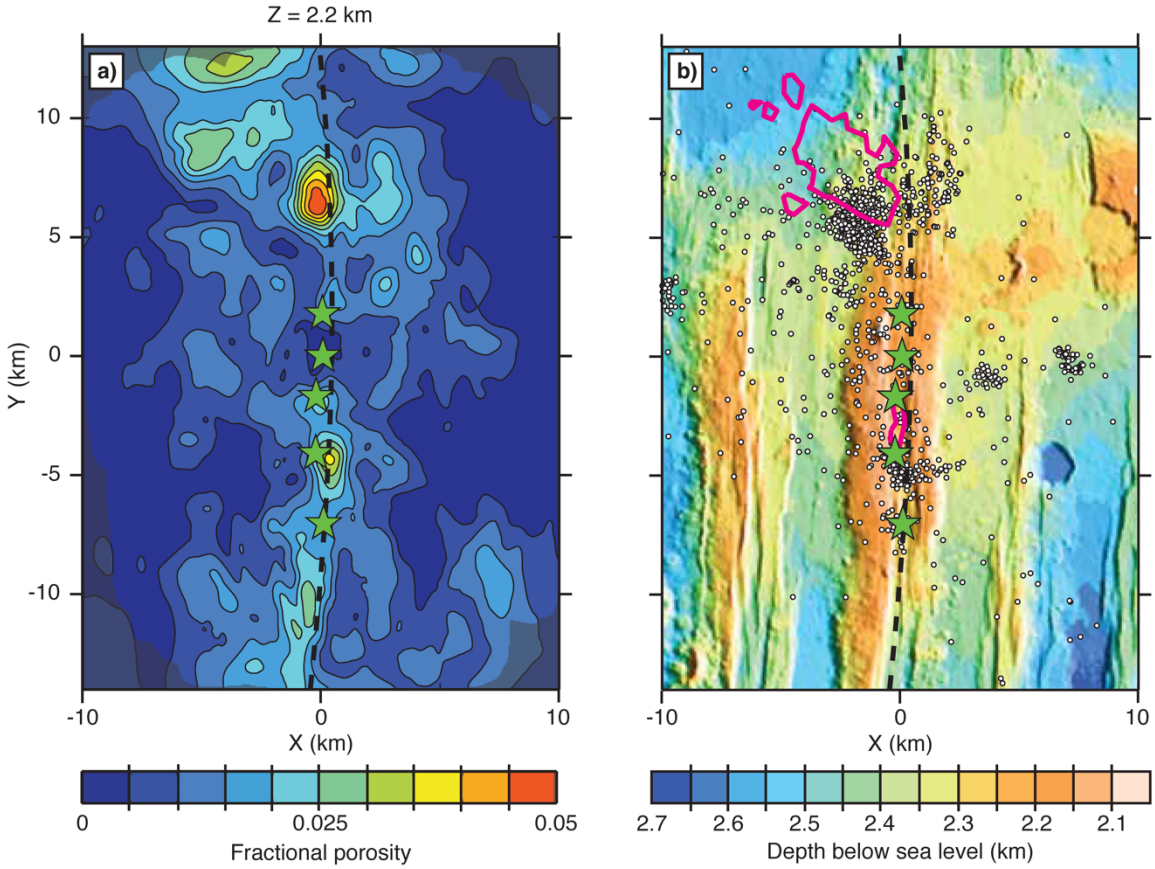

Figure S13. Map view section of lateral porosity variations in relation to seismicity. (a) Depth slice through the preferred velocity model converted to porosity at 2.2 km bsf. The contour interval is 0.005. Plot is masked in regions where the derivative weight sum is less than 10. (b) Bathymetry of the area showing epicenters of post-swarm earthquakes that occurred between October 2005 and June 2006 (white circles) (Weekly et al., 2013). Magenta contours show areas with earthquake densities >20 events per km^2 recorded during the February 2005 swarm (Hooft et al., 2010). Locations of the vent fields (green stars) and plate boundary (dashed black line) are overlain on each plot.

REFERENCES CITED

Chapter II

Canales, J. P., Detrick, R. S., Toomey, D. R., & Wilcock, W. S. D. (2003). Segment-scale variations in the crustal structure of 150-300 kyr old fast spreading oceanic crust (East Pacific rise, 8°15'N-10°5'N) from wide-angle seismic refraction profiles. *Geophysical Journal International*, *152*(3), 766–794.

Canales, J. P., Nedimovi, M. R., Kent, G. M., Carbotte, S. M., & Detrick, R. S. (2009). Seismic reflection images of a near-axis melt sill within the lower crust at the juan de fuca ridge. *Nature*, *460*(7251), 89–93.

Canales, J. P., Carton, H., Carbotte, S. M., Mutter, J. C., Nedimović, M. R., Xu, M., et al. (2012). Network of off-axis melt bodies at the East Pacific Rise. *Nature Geoscience*, *5*(4), 279–283.

Ceuleneer, G., Monnereau, M., & Amri, I. (1996). Thermal structure of a fossil mantle diapir inferred from the distribution of mafic cumulates. *Nature, 379*(6561), 149.

Detrick, R. S., Buhl, P., Vera, E. E., Mutter, J., Orcutt, J. A., Madsen, J., & Brocher, T. (1987). Multi-channel seismic imaging of a crustal magma chamber along the East Pacific Rise. *Nature*, *326*(5), 35–41.

Dunn, R. A., Lekić, V., Detrick, R. S., & Toomey, D. R. (2005). Three-dimensional seismic structure of the Mid-Atlantic Ridge (35°N): Evidence for focused melt supply and lower crustal dike injection. *Journal of Geophysical Research: Solid Earth*, *110*(B9).

Durant, T. D., & Toomey, D. R. (2009). Evidence and implications of crustal magmatism on the flanks of the East Pacific Rise. *Earth and Planetary Science Letters*, *287*(1–2), 130–136.

Garmany, J. (1989). Accumulations of melt at the base of young oceanic crust. *Nature*, *340*, 628–632.

Godard, M., Jousselin, D., & Bodinier, J. L. (2000). Relationships between geochemistry and structure beneath a palaeo-spreading centre: A study of the mantle section in the Oman ophiolite. *Earth and Planetary Science Letters*, *180*(1–2), 133–148.

Hebert, L. B., & Montési, L. G. J. (2010). Generation of permeability barriers during melt extraction at mid-ocean ridges. *Geochemistry, Geophysics, Geosystems*, *11*(12).

Kelemen, P. B., & Aharonov, E. (1998). Periodic formation of magma fractures and generation of layered gabbros in the lower crust beneath oceanic spreading ridges. *Geophysical Monograph*, *106*, 267–289.

Kelemen, P. B., Shimizu, N., & Salters, V. J. M. (1995). Extraction of mid-ocean-ridge basalt from the upwelling mantle by focused flow of melt in dunite channels. *Nature*, *375*(6534), 747–753.

Kelemen, P. B., Hirth, G., Shimizu, N., Spiegelman, M., & Dick, H. J. B. (1997). A review of melt migration processes in the adiabatically upwelling mantle beneath oceanic spreading ridges. *Philosophical Transactions of the Royal Society A: Mathematical, Physical and Engineering Sciences*.

Korenaga, J., & Kelemen, P. B. (1997). Origin of gabbro sills in the Moho transition zone of the Oman ophiolite : Implications for magma transport in. *Journal of Geophysical Research: Solid Earth*, *102*(B12), 27729–27749.

Larsen, S., & Harris, D. (1993). Seismic Wave Propagation Through a Low-Velocity Nuclear Rubble Zone, Lawrence Livermore Natl. Lab., Livermore, Calif.

Nedimović, M. R., Carbotte, S. M., Harding, A. J., Detrick, R. S., Canales, J. P., Diebold, J. B., et al. (2005). Frozen magma lenses below the oceanic crust. *Nature*, *436*(7054), 1149–52.

Rabinowicz, M., & Ceuleneer, G. (2005). The effect of sloped isotherms on melt migration in the shallow mantle: A physical and numerical model based on observations in the Oman ophiolite. *Earth and Planetary Science Letters*, *229*, 231–246.

Sauter, D., Unternehr, P., Manatschal, G., Tugend, J., Cannat, M., Le Quellec, P., et al. (2016). Evidence for magma entrapment below oceanic crust from deep seismic reflections in the Western Somali Basin. *Geology*, *44*(6), 407–410.

Schimmel, M., & Paulssen, H. (1997). Noise reduction and detection of weak, coherent signals through phase weighted stacks. *Geophysical Journal International*, *130*, 497–505.

Sparks, D. W., & Parmentier, E. M. (1991). Melt extraction from the mantle beneath spreading centers. *Earth and Planetary Science Letters*, *105*, 368–377.

Spiegelman, M. (1993a). Flow in deformable porous media. Part 2 numerical analysis—the relationship between shock waves and solitary waves. Journal of Fluid Mechanics, *247*, 39-63.

Spiegelman, M. (1993b). Physics of melt extraction: Theory, implications and applications. *Phil. Trans. R. Soc. Lond. A, 342*(1663), 23–41.

Takazawa, E., Okayasu, T., & Satoh, K. (2003). Geochemistry and origin of the basal lherzolites from the northern Oman ophiolite (northern Fizh block). *Geochemistry, Geophysics, Geosystems*, *4*(2).

The MELT Seismic Team. (1998). Imaging the Deep Seismic Structure Beneath a Mid-Ocean Ridge: The MELT Experiment. *Science*, *280*(5367), 1215–1218.

Toomey, D. R., Solomon, S. C., & Purdy, G. M. (1994). Tomographic imaging of the shallow crustal structure of the East Pacific Rise at 9°30′N. *Journal of Geophysical Research: Solid Earth, 99*(B12), 24135-24157.

Toomey, D. R., Jousselin, D., Dunn, R. a, Wilcock, W. S. D., & Detrick, R. S. (2007). Skew of mantle upwelling beneath the East Pacific Rise governs segmentation. *Nature*, *446*, 409–414.

Vera, E. E., Mutter, J. C., Buhl, P., Orcutt, J. A., Harding, A. J., Kappus, M. E., et al. (1990). The structure of 0- to 0.2-m.y.-old oceanic crust at 9°N on the East Pacific Rise from expanded spread profiles. *Journal of Geophysical Research: Solid Earth*, *95*, 15529–15556.

Chapter III

Van Ark, E. M., Detrick, R. S., Canales, J. P., Carbotte, S. M., Harding, A. J., Kent, G. M., et al. (2007). Seismic structure of the Endeavour Segment, Juan de Fuca Ridge: Correlations with seismicity and hydrothermal activity. *Journal of Geophysical Research: Solid Earth*, *112*(B2).

Arnoux, G. M., Toomey, D. R., Hooft, E. E. E., Wilcock, W. S. D., Morgan, J., Warner, M., & VanderBeek, B. P. (2017). Seismic evidence that black smoker heat flux is influenced by localized magma replenishment and associated increases in crustal permeability. *Geophysical Research Letters*, *44*(4), 1687–1695.

Barth, G. A., & Mutter, J. C. (1996). Variability in oceanic crustal thickness and structure: Multichannel seismic reflection results from the northern East Pacific Rise. *Journal of Geophysical Research: Solid Earth*, *101*(B8), 17951–17975.

Bazin, S., Harding, A. J., Kent, G. M., Orcutt, J. A., Singh, S. C., Tong, C. H., et al. (2003). A three-dimensional study of a crustal low velocity region beneath the 9°03′N overlapping spreading center. *Geophysical Research Letters*, *30*(2).

Bell, R. E., & Buck, W. R. (1992). Crustal control of ridge segmentation inferred from observations of the Reykjanes Ridge. *Nature*, *357*, 583–586.

Bohnenstiehl, D. R., Dziak, R. P., Tolstoy, M., Fox, C. G., & Fowler, M. (2004). Temporal and spatial history of the 1999-2000 Endeavour Segment seismic series, Juan de Fuca Ridge. *Geochemistry, Geophysics, Geosystems*, *5*(9).

Butterfield, D. A., McDuff, R. E., Mottl, M. J., Lilley, M. D., Lupton, J. E., & Massoth, G. J. (1994). Gradients in the composition of hydrothermal fluids from the Endeavour segment vent field: Phase separation and brine loss. *Journal of Geophysical Research: Solid Earth, 99*(B5), 9561-9583.

Byrnes, J. S., Toomey, D. R., Hooft, E. E. E., Nábělek, J., & Braunmiller, J. (2017). Mantle dynamics beneath the discrete and diffuse plate boundaries of the Juan de Fuca plate: Results from Cascadia Initiative body wave tomography. *Geochemistry, Geophysics, Geosystems*, *18*(8), 2906–2929.

Canales, J. P., Detrick, R. S., Toomey, D. R., & Wilcock, W. S. D. (2003). Segment-scale variations in the crustal structure of 150-300 kyr old fast spreading oceanic crust (East Pacific rise, 8°15'N-10°5'N) from wide-angle seismic refraction profiles. *Geophysical Journal International*, *152*(3), 766–794.

Canales, J. P., Dunn, R. A., Ito, G., Detrick, R. S., & Sallarès, V. (2014). Effect of Variations in Magma Supply on the Crustal Structure of Mid-Ocean Ridges: Insights from the Western Galápagos Spreading Center. In *The Galapagos: A Natural Laboratory for the Earth Sciences* (pp. 363–391).

Carbotte, S. M., Canales, J. P., Nedimović, M., Carton, H., & Mutter, J. (2012). Recent Seismic Studies at the East Pacific Rise 8°20'–10°10'N and Endeavour Segment: Insights into Mid-Ocean Ridge Hydrothermal and Magmatic Processes. *Oceanography, 25*(1), 100-112.

Carbotte, S. M., Detrick, R. S., Harding, A., Canales, J. P., Babcock, J., Kent, G., et al. (2006). Rift topography linked to magmatism at the intermediate spreading Juan de Fuca Ridge. *Geology*, *34*(3), 209–212.

Carbotte, S. M., Nedimović, M. R., Canales, J. P., Kent, G. M., Harding, A. J., & Marjanović, M. (2008). Variable crustal structure along the Juan de Fuca Ridge: Influence of on-axis hot spots and absolute plate motions. *Geochemistry, Geophysics, Geosystems*, *9*(8).

Carbotte, S. M., Marjanović, M., Carton, H., Mutter, J. C., Canales, J. P., Nedimović, M. R., et al. (2013). Fine-scale segmentation of the crustal magma reservoir beneath the East Pacific Rise. *Nature Geoscience*, *6*(10), 866–870.

Caristan, Y. (1982). The transition from high temperature creep to fracture in Maryland diabase. *Journal of Geophysical Research: Solid Earth*, *87*(B8), 6781–6790.

Chen, J., & Morgan, J. P. (1996). The effects of spreading rate, the magma budget, and the geometry of magma emplacement on the axial heat flux at mid-ocean ridges. *Journal of Geophysical Research: Solid Earth*, *101*(B5), 11475–11482.

Christensen, N. I., & Salisbury, M. H. (1979). Seismic anisotropy in the oceanic upper mantle: Evidence from the Bay of Islands Ophiolite Complex. *Journal of Geophysical Research: Solid Earth*, *84*(B9), 4601–4610.

Clague, D. A., Dreyer, B. M., Paduan, J. B., Martin, J. F., Caress, D. W., Guilderson, T. P., & Mcgann, M. L. (2014). Eruptive and tectonic history of the Endeavour Segment, Juan de Fuca Ridge, based on AUV mapping data and lava flow ages. *Geochemistry, Geophysics, Geosystems*, *15*(8), 3364–3391.

Collier, J. S., & Sinha, M. C. (1992). Seismic mapping of a magma chamber beneath the Valu Fa Ridge, Lau Basin. *Journal of Geophysical Research: Solid Earth*, *97*(B10), 14031–14053.

Crisp, J. A. (1984). Rates of magma emplacement and volcanic output. *Journal of Volcanology and Geothermal Research*, *20*(3–4), 177–211.

Davis, E. E., & Lister, C. R. B. (1977). Heat flow measured over the Juan de Fuca Ridge: Evidence for widespread hydrothermal circulation in a highly heat transportive crust. *Journal of Geophysical Research*, *82*(30), 4845–4860.

Davis, E. E., & Villinger, H. (1992). Tectonic and thermal structure of the Middle Valley sedimented rift, northern Juan de Fuca Ridge. In *Proc. ODP, Init. Repts.* (Vol. 139, pp. 9-41). Ocean Drilling Program.

DeMets, C., Gordon, R. G., & Argus, D. F. (2010). Geologically current plate motions. *Geophysical Journal International*, *181*(1), 1–80.

Detrick, R. S., Buhl, P., Vera, E. E., Mutter, J., Orcutt, J. A., Madsen, J., & Brocher, T. (1987). Multi-channel seismic imaging of a crustal magma chamber along the East Pacific Rise. *Nature*, *326*(5), 35–41.

Dunn, R. A., Toomey, D. R., & Solomon, S. C. (2000). Three-dimensional seismic structure and physical properties of the crust and shallow mantle beneath the East Pacific Rise at 9°30′N. *Journal of Geophysical Research: Solid Earth*, *105*(B10), 23537–23555.

Dunn, R. A., Lekić, V., Detrick, R. S., & Toomey, D. R. (2005). Three-dimensional seismic structure of the Mid-Atlantic Ridge (35°N): Evidence for focused melt supply and lower crustal dike injection. *Journal of Geophysical Research: Solid Earth*, *110*(B9).

Dunn, R. A., Martinez, F., & Conder, J. A. (2013). Crustal construction and magma chamber properties along the Eastern Lau Spreading Center. *Earth and Planetary Science Letters*, *371–372*, 112–124.

Dziak, R. P. (2006). Explorer deformation zone: Evidence of a large shear zone and reorganization of the Pacific-Juan de Fuca-North American triple junction. *Geology*, *34*(3), 213–216.

Francheteau, J., & Ballard, R. D. (1983). The East Pacific Rise near 21°N, 13°N and 20°S: inferences for along-strike variability of axial processes of the Mid-Ocean Ridge. *Earth and Planetary Science Letters*, *64*(1), 93–116.

Goss, A. R., Perfit, M. R., Ridley, W. I., Rubin, K. H., Kamenov, G. D., Soule, S. A., et al. (2010). Geochemistry of lavas from the 2005-2006 eruption at the East Pacific Rise, 9°46'N-9°56'N: Implications for ridge crest plumbing and decadal changes in magma chamber compositions. *Geochemistry, Geophysics, Geosystems*, *11*(5), 1–35.

Gregory, R. T., & Taylor, H. P. (1981). An oxygen isotope profile in a section of Cretaceous oceanic crust, Samail Ophiolite, Oman: Evidence for δ18O buffering of the oceans by deep (>5 km) seawater-hydrothermal circulation at mid-ocean ridges. *Journal of Geophysical Research: Solid Earth*, *86*(B4), 2737–2755.

Gripp, A. E., & Gordon, R. G. (2002). Young tracks of hotspots and current plate velocities. *Geophysical Journal International*, *150*(2), 321–361.

Hasenclever, J., Theissen-Krah, S., Rüpke, L. H., Morgan, J. P., Iyer, K., Petersen, S., & Devey, C. W. (2014). Hybrid shallow on-axis and deep off-axis hydrothermal circulation at fast-spreading ridges. *Nature*, *508*, 508–12.

Henstock, T. J., Woods, A. W., & White, R. S. (1993). The accretion of oceanic crust by episodic sill intrusion. *Journal of Geophysical Research: Solid Earth*, *98*(B3), 4143–4161.

Hooft, E. E. E., Detrick, R. S., & Kent, G. M. (1997). Seismic structure and indicators of magma budget along the Southern East Pacific Rise. *Journal of Geophysical Research: Solid Earth.*, *102*(B12), 27319–27340.

Hooft, E. E. E., Patel, H., Wilcock, W., Becker, K., Butterfield, D., Davis, E., et al. (2010). A seismic swarm and regional hydrothermal and hydrologic perturbations: The northern Endeavour segment, February 2005. *Geochemistry, Geophysics, Geosystems*, *11*(12).

Isaak, D. G. (1992). High-temperature elasticity of iron-bearing olivines. *Journal of Geophysical Research: Solid Earth*, *97*(B2), 1871–1885.

Jackson, I., Paterson, M. S., & Fitz Gerald, J. D. (1992). Seismic wave dispersion and attenuation in Aheim dunite: and experimental study. *Geophysical Journal International*, *108*(2), 517–534.

Karato, S. (1993). Importance of anelasticity in the interpretation of seismic tomography. *Geophysical Research Letters*, *20*(15), 1623–1626.

Karsten, J. L., Hammond, S. R., Davis, E. E., & Currie, R. G. (1986). Detailed geomorphology and neotectonics of the Endeavour Segment, Juan de Fuca Ridge: New results from Seabeam swath mapping. *Geological Society of America Bulletin*, *97*(2), 213–221.

Karsten, J. L., Delaney, J. R., Rhodes, J. M., & Liias, R. A. (1990). Spatial and temporal evolution of magmatic systems beneath the Endeavour Segment, Juan de Fuca Ridge: Tectonic and petrologic constraints. *Journal of Geophysical Research: Solid Earth*, *95*(B12), 19235–19256.

Kelley, D. S., Carbotte, S., Caress, D., Clague, D., Delaney, J., Gill, J., et al. (2012). Endeavour Segment of the Juan de Fuca Ridge: One of the most remarkable places on Earth. *Oceanography, 25*(1), 44-61.

Kelley, D. S., Baross, J. A., & Delaney, J. R. (2002). Volcanoes, fluids, and life at mid-ocean ridge spreading centers. *Annual Review of Earth and Planetary Sciences*, *30*, 385–491.

Kellogg, J. (2011). Temporal and spatial variability of hydrothermal fluxes within a mid-ocean ridge segment, PhD Thesis, Univ. of Washington, Seattle, WA.

Kent, G. M., Harding, A. J., & Orcutt, J. A. (1993). Distribution of magma beneath the East Pacific Rise between the Clipperton Transform and the 9°17′N Deval from forward modeling of common depth point data. *Journal of Geophysical Research: Solid Earth*, *98*(B8), 13945–13969.

Kent, G. M., Singh, S. C., Harding, A. J., Sinha, M. C., Orcutt, J. A., Barton, P. J., et al. (2000). Evidence from three-dimensional seismic reflectivity images for enhanced melt supply beneath mid-ocean-ridge discontinuities. *Nature*, *406*, 614–618.

Kleinrock, M. C., Tucholke, B. E., Lin, J., & Tivey, M. A. (1997). Fast rift propagation at a slow-spreading ridge. *Geology*, *25*(7), 639–642.

Langmuir, C. H., Bender, J. F., & Batiza, R. (1986). Petrological and tectonic segmentation of the East Pacific rise, 5°30′-14°30′ N. *Nature*, *322*, 422–429.

Macdonald, K. C., Fox, P. J., Perram, L. J., Eisen, M. F., Haymon, R. M., Miller, S. P., et al. (1988). A new view of the mid-ocean ridge from the behaviour of ridge-axis discontinuities. *Nature*, *335*, 217–225.

Macdonald, K. C., Scheirer, D. S., & Carbotte, S. M. (1991). Mid-ocean ridges: Discontinuities, segments and giant cracks. *Science*, *253*(5023), 986–994.

Marjanović, M., Carbotte, S. M., Carton, H., Nedimović, M. R., Mutter, J. C., & Canales, J. P. (2014). A multi-sill magma plumbing system beneath the axis of the East Pacific Rise. *Nature Geoscience*, *7*, 825–829.

Mavko, G. M. (1980). Velocity and attenuation in partially molten rocks. *Journal of Geophysical Research: Solid Earth*, *85*(B10), 5173–5189.

Morgan, J., Warner, M., Arnoux, G., Hooft, E., Toomey, D., VanderBeek, B., & Wilcock, W. (2016). Next-generation seismic experiments – II: wide-angle, multi-azimuth, 3-D, full-waveform inversion of sparse field data. *Geophysical Journal International*, *204*(2), 1342–1363.

Nicolas, A., Boudier, F., & Ildefonse, B. (1996). Variable crustal thickness in the Oman ophiolite: Implication for oceanic crust. *Journal of Geophysical Research: Solid Earth*, *101*(B8), 17941–17950.

Schmeling, H. (1985). Numerical models on the influence of partial melt on elastic, anelastic and electric properties of rocks. Part I: elasticity and anelasticity. *Physics of the Earth and Planetary Interiors*, *41*(1), 34–57.

Schouten, H., Klitgord, K. D., & Whitehead, J. A. (1985). Segmentation of mid-ocean ridges. *Nature*, *317*, 225–229.

Seher, T., Crawford, W. C., Singh, S. C., Cannat, M., Combier, V., & Dusunur, D. (2010). Crustal velocity structure of the Lucky Strike segment of the Mid-Atlantic Ridge at 37°N from seismic refraction measurements. *Journal of Geophysical Research: Solid Earth*, *115*(B3).

Shaw, P. R., & Orcutt, J. A. (1985). Waveform inversion of seismic refraction data and applications to young Pacific crust. *Geophysical Journal International*, *82*(3), 375–414.

Shoberg, T., Stein, S., & Karsten, J. (1991). Constraints on rift propagation history at the Cobb Offset, Juan de Fuca Ridge, from numerical modeling of tectonic fabric. *Tectonophysics*, *197*(2–4), 295–308.

Sinton, J. M., & Detrick, R. S. (1992). Mid-ocean ridge magma chambers. *Journal of Geophysical Research: Solid Earth*, *97*(B1), 197–216.

Soule, D., Wilcock, W. S. D., Toomey, D. R., Hooft, E. E. E., & Weekly, R. T. (2016). Near-axis crustal structure and thickness of the Endeavour Segment, Juan de Fuca Ridge. *Geophysical Research Letters*, *43*(11), 5688-5695.

Sparks, D. W., & Parmentier, E. M. (1991). Melt extraction from the mantle beneath spreading centers. *Earth and Planetary Science Letters*, *105*, 368–377.

Toomey, D. R., & Foulger, G. R. (1989). Tomographic inversion of local earthquake data from the Hengill-Grensdalur Central Volcano Complex, Iceland. *Journal of Geophysical Research: Solid Earth*, *94*(B12), 17497–17510.

Toomey, D. R., & Hooft, E. E. E. (2008). Mantle upwelling, magmatic differentiation, and the meaning of axial depth at fast-spreading ridges. *Geology*, *36*(9), 679–682.

Toomey, D. R., Purdy, G. M., Solomon, S. C., & Wilcock, W. S. D. (1990). The three-dimensional seismic velocity structure of the East Pacific Rise near latitude 9°30′N. *Nature*, *347*, 639–645.

Toomey, D. R., Solomon, S. C., & Purdy, G. M. (1994). Tomographic imaging of the shallow crustal structure of the East Pacific Rise at 9°30′N. *Journal of Geophysical Research: Solid Earth, 99*(B12), 24135-24157.

Toomey, D. R., Jousselin, D., Dunn, R. a, Wilcock, W. S. D., & Detrick, R. S. (2007). Skew of mantle upwelling beneath the East Pacific Rise governs segmentation. *Nature*, *446*, 409–414.

Turner, I. M., Peirce, C., & Sinha, M. C. (1999). Seismic imaging of the axial region of the Valu Fa Ridge, Lau Basin - the accretionary processes of an intermediate back-arc spreading ridge. *Geophysical Journal International*, *138*(2), 495–519.

VanderBeek, B. P., Toomey, D. R., Hooft, E. E. E., & Wilcock, W. S. D. (2016). Segmentation of mid-ocean ridges attributed to oblique mantle divergence. *Nature Geoscience*, *9*, 636–642.

Weekly, R. T., Wilcock, W. S. D., Hooft, E. E. E., Toomey, D. R., McGill, P. R., & Stakes, D. S. (2013). Termination of a 6 year ridge-spreading event observed using a seafloor seismic network on the Endeavour Segment, Juan de Fuca Ridge. *Geochemistry, Geophysics, Geosystems*, *14*(5).

Weekly, R. T., Wilcock, W. S. D., Toomey, D. R., Hooft, E. E. E., & Kim, E. (2014). Upper crustal seismic structure of the Endeavour segment, Juan de Fuca Ridge from traveltime tomography: Implications for oceanic crustal accretion. *Geochemistry, Geophysics, Geosystems*, *15*(4), 1296–1315.

West, M., Menke, W., Tolstoy, M., Webb, S., & Sohn, R. (2001). Magma storage beneath Axial volcano on the Juan de Fuca mid-ocean ridge. *Nature*, *413*, 833–836.

White, S. M., Macdonald, K. C., & Haymon, R. M. (2000). Basaltic lava domes, lava lakes, and volcanic segmentation on the southern East Pacific Rise. *Journal of Geophysical Research: Solid Earth*, *105*(B10), 23519–23536.

White, S. M., Haymon, R. M., Fornari, D. J., Perfit, M. R., & Macdonald, K. C. (2002). Correlation between volcanic and tectonic segmentation of fast-spreading ridges: Evidence from volcanic structures and lava flow morphology on the East Pacific Rise at 9°–10°N. *Journal of Geophysical Research: Solid Earth*, *107*(B8), EPM-7.

Whitehead, J. A., Dick, H. J. B., & Schouten, H. (1984). A mechanism for magmatic accretion under spreading centres. *Nature*, *312*, 146–148.

Wilcock, W. S. D., & Delaney, J. R. (1996). Mid-ocean ridge sulfide deposits: Evidence for heat extraction from magma chambers or cracking fronts? *Earth and Planetary Science Letters*, *145*(1–4), 49–64.

Wilcock, W. S. D., Dougherty, M. E., Solomon, S. C., Purdy, G. M., & Toomey, D. R. (1993). Seismic propagation across the East Pacific Rise: Finite difference experiments and implications for seismic tomography. *Journal of Geophysical Research: Solid Earth*, *98*(B11), 19913–19932.

Wilcock, W. S. D., Solomon, S. C., Purdy, G. M., & Toomey, D. R. (1995). Seismic attenuation structure of the East Pacific Rise near 9°30′N. *Journal of Geophysical Research: Solid Earth*, *100*(B12), 24147–24165.

Wilcock, W. S. D., Hooft, E. E. E., Toomey, D. R., McGill, P. R., Barclay, A. H., Stakes, D. S., & Ramirez, T. M. (2009). The role of magma injection in localizing black-smoker activity. *Nature Geoscience, 2*, 509-513.

Wilson, D. S. (1988). Tectonic history of the Juan de Fuca Ridge over the last 40 million years. *Journal of Geophysical Research: Solid Earth*, *93*(B10), 11863–11876.

Wilson, D. S. (1993). Confidence intervals for motion and deformation of the Juan de Fuca Plate. *Journal of Geophysical Research: Solid Earth*, *98*(B9), 16053–16071.

Chapter IV

Van Ark, E. M., Detrick, R. S., Canales, J. P., Carbotte, S. M., Harding, A. J., Kent, G. M., et al. (2007). Seismic structure of the Endeavour Segment, Juan de Fuca Ridge: Correlations with seismicity and hydrothermal activity. *Journal of Geophysical Research: Solid Earth*, *112*.

Barclay, A. H., & Wilcock, W. S. D. (2004). Upper crustal seismic velocity structure and microearthquake depths at the Endeavour Segment, Juan de Fuca Ridge. *Geochemistry, Geophysics, Geosystems*, *5*(1).

Bernabé, Y., Mok, U., & Evans, B. (2003). Permeability-porosity Relationships in Rocks Subjected to Various Evolution Processes. *Pure and Applied Geophysics*, *160*(5), 937–960.

Bohnenstiehl, D. R., Dziak, R. P., Tolstoy, M., Fox, C. G., & Fowler, M. (2004). Temporal and spatial history of the 1999-2000 Endeavour Segment seismic series, Juan de Fuca Ridge. *Geochemistry, Geophysics, Geosystems*, *5*(9).

Butterfield, D. A., McDuff, R. E., Mottl, M. J., Lilley, M. D., Lupton, J. E., & Massoth, G. J. (1994). Gradients in the composition of hydrothermal fluids from the Endeavour segment vent field: Phase separation and brine loss. *Journal of Geophysical Research: Solid Earth, 99*(B5), 9561-9583.

Carbotte, S. M., Nedimović, M. R., Canales, J. P., Kent, G. M., Harding, A. J., & Marjanović, M. (2008). Variable crustal structure along the Juan de Fuca Ridge: Influence of on-axis hot spots and absolute plate motions. *Geochemistry, Geophysics, Geosystems*, *9*(8).

Carbotte, S. M., Canales, J. P., Nedimović, M., Carton, H., & Mutter, J. (2012). Recent Seismic Studies at the East Pacific Rise 8°20'–10°10'N and Endeavour Segment: Insights into Mid-Ocean Ridge Hydrothermal and Magmatic Processes. *Oceanography, 25*(1), 100-112.

Carlson, R. L. (2010). How crack porosity and shape control seismic velocities in the upper oceanic crust: Modeling downhole logs from Holes 504B and 1256D. *Geochemistry, Geophysics, Geosystems*, *11*(4), 1–15.

Carlson, R. L. (2011). The effect of hydrothermal alteration on the seismic structure of the upper oceanic crust: Evidence from Holes 504B and 1256D. *Geochemistry, Geophysics, Geosystems*, *12*(9), 1–11.

Carlson, R. L. (2014). The influence of porosity and crack morphology on seismic velocity and permeability in the upper oceanic crust. *Geochemistry, Geophysics, Geosystems*, *15*(1), 10–27.

Choi, J., & Lowell, R. P. (2015). The response of two-phase hydrothermal systems to changing magmatic heat input at mid-ocean ridges. *Deep-Sea Research Part II: Topical Studies in Oceanography*, *121*, 17–30.

Christensen, N. I. (1996). Poisson's ratio and crustal seismology. *Journal of Geophysical Research: Solid Earth*, *101*(B2), 3139-3156.

Clague, D. A., Dreyer, B. M., Paduan, J. B., Martin, J. F., Caress, D. W., Guilderson, T. P., & Mcgann, M. L. (2014). Eruptive and tectonic history of the Endeavour Segment, Juan de Fuca Ridge, based on AUV mapping data and lava flow ages. *Geochemistry, Geophysics, Geosystems*, *15*(8), 3364–3391.

Delaney, J. R., McDuff, R. E., & Lupton, J. E. (1984). Hydrothermal fluid temperatures of 400 °C on the Endeavour Segment, northern Juan de Fuca Ridge. *Eos*, *65*(973), 45.

Fontaine, F. J., Cannat, M., Escartin, J., & Crawford, W. C. (2014). Along-axis hydrothermal flow at the axis of slow spreading Mid-Ocean Ridges: Insights from numerical models of the Lucky Srike vent field (MAR). *Geochemistry, Geophysics, Geosystems*, *15*, 2918–2931.

Germanovich, L. N., Lowell, R. P., & Ramondenc, P. (2011). Magmatic origin of hydrothermal response to earthquake swarms: Constraints from heat flow and geochemical data. *Journal of Geophysical Research: Solid Earth*, *116*(5), 1–25.

Hooft, E. E. E., Patel, H., Wilcock, W., Becker, K., Butterfield, D., Davis, E., et al. (2010). A seismic swarm and regional hydrothermal and hydrologic perturbations: The northern Endeavour segment, February 2005. *Geochemistry, Geophysics, Geosystems*, *11*(12).

Humphris, S. E., & Cann, J. R. (2000). Constraints on the energy and chemical balances of the modern TAG and ancient Cyprus seafloor sulfide deposits. *Journal of Geophysical Research: Solid Earth*, *105*(B12), 28477.

Kelley, D. S., Baross, J. A., & Delaney, J. R. (2002). Volcanoes, fluids, and life at mid-ocean ridge spreading centers. *Annual Review of Earth and Planetary Sciences*, *30*, 385–491.

Kelley, D. S., Carbotte, S., Caress, D., Clague, D., Delaney, J., Gill, J., et al. (2012). Endeavour Segment of the Juan de Fuca Ridge: One of the most remarkable places on Earth. *Oceanography, 25*(1), 44-61.

Kellogg, J. (2011). Temporal and spatial variability of hydrothermal fluxes within a mid-ocean ridge segment, PhD Thesis, Univ. of Washington, Seattle, WA.

Kern, H., Popp, T., Gorbatsevich, F., Zharikov, A., Lobanov, K. V., & Smirnov, Y. P. (2001). Pressure and temperature dependence of Vp and Vs in rocks from the superdeep well and from surface analogues at Kola and the nature of velocity anisotrophy. *Tectonophysics*, *338*(2), 113–134.

Liu, L., & Lowell, R. P. (2009). Models of hydrothermal heat output from a convecting, crystallizing, replenished magma chamber beneath an oceanic spreading center. *Journal of Geophysical Research: Solid Earth*, *114*(2), 1–14.

Lowell, R. P., & Germanovich, L. N. (2004). Hydrothermal Processes at Mid-Ocean Ridges: Results from Scale Analysis and Single-Pass Models. *Mid-Ocean Ridges*, 219–244.

Lowell, R. P., Farough, A., Hoover, J., & Cummings, K. (2013). Characteristics of magma-driven hydrothermal systems at oceanic spreading centers. *Geochemistry, Geophysics, Geosystems*, *14*(6), 1756–1770.

Macdonald, K. C., Fox, P. J., Alexander, R. T., Pockalny, R., & Gente, P. (1996). Volcanic growth faults and the origin of Pacific abyssal hills. *Nature*, 125–129.

Morgan, J., Warner, M., Arnoux, G., Hooft, E., Toomey, D., VanderBeek, B., & Wilcock, W. (2016). Next-generation seismic experiments – II: wide-angle, multi-azimuth, 3-D, full-waveform inversion of sparse field data. *Geophysical Journal International*, *204*(2), 1342–1363.

Singh, S., Lowell, R. P., & Lewis, K. C. (2013). Numerical modeling of phase separation at Main Endeavour Field, Juan de Fuca Ridge. *Geochemistry, Geophysics, Geosystems*, *14*(10), 4021–4034.

Singh, S. C., Collier, J. S., Harding, A. J., Kent, G. M., & Orcutt, J. A. (1999). Seismic evidence for a hydrothermal layer above the solid roof of the axial magma chamber at the southern East Pacific Rise. *Geology*, *27*(3), 219–222.

Swift, S., Reichow, M., Tikku, A., Tominaga, M., & Gilbert, L. (2008). Velocity structure of upper ocean crust at ocean drilling program site 1256. *Geochemistry, Geophysics, Geosystems*, *9*(10).

Thompson, W. J., McDuff, R. E., Stahr, F. R., Yoerger, D. R., & Jakuba, M. (2005). Heat flux from the Endeavour segment of the Juan de Fuca Ridge. *Eos*, *86*(Fall Meet. Suppl. abstr. T31A-0489).

Thurber, C. H. (1983). Earthquake locations and three-dimensional crustal structure in the Coyote Lake Area, central California. *Journal of Geophysical Research: Solid Earth, 88*(B10), 8226-8236.

Toomey, D. R., & Foulger, G. R. (1989). Tomographic inversion of local earthquake data from the Hengill-Grensdalur Central Volcano Complex, Iceland. *Journal of Geophysical Research: Solid Earth*, *94*(B12), 17497–17510.

Warner, M., Ratcliffe, A., Nangoo, T., Morgan, J., Umpleby, A., Shah, N., et al. (2013). Anisotropic 3D full-waveform inversion. *Geophysics*, *78*(2), R59–R80.

Weekly, R. T., Wilcock, W. S. D., Hooft, E. E. E., Toomey, D. R., McGill, P. R., & Stakes, D. S. (2013). Termination of a 6 year ridge-spreading event observed using a seafloor seismic network on the Endeavour Segment, Juan de Fuca Ridge. *Geochemistry, Geophysics, Geosystems*, *14*(5).

Weekly, R. T., Wilcock, W. S. D., Toomey, D. R., Hooft, E. E. E., & Kim, E. (2014). Upper crustal seismic structure of the Endeavour segment, Juan de Fuca Ridge from traveltime tomography: Implications for oceanic crustal accretion. *Geochemistry, Geophysics, Geosystems*, *15*(4), 1296–1315.

Wilcock, W. S. D., & Delaney, J. R. (1996). Mid-ocean ridge sulfide deposits: Evidence for heat extraction from magma chambers or cracking fronts? *Earth and Planetary Science Letters*, *145*(1–4), 49–64.

Wilcock, W. S. D., Hooft, E. E. E., Toomey, D. R., McGill, P. R., Barclay, A. H., Stakes, D. S., & Ramirez, T. M. (2009). The role of magma injection in localizing black-smoker activity. *Nature Geoscience, 2*, 509-513.